

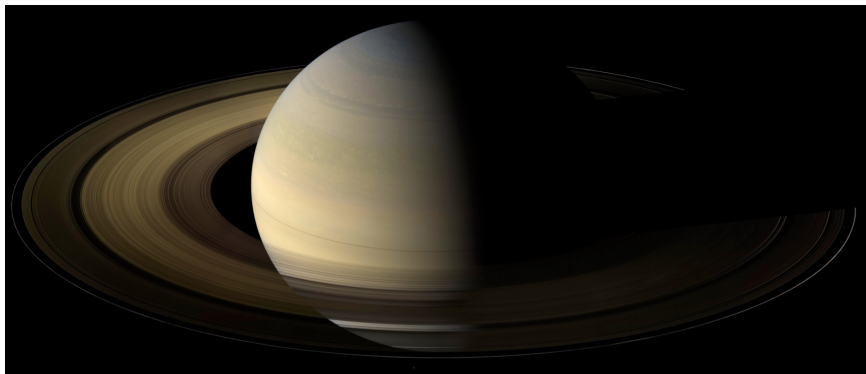
UNIVERSITY OF TWENTE

MASTER THESIS

MercuryDPM: From a Chip to Saturn

Author:
Edgar Ortega Roano

Supervisors:
Prof. Dr. Devaraj
van der Meer,
Prof. Dr. Stefan
Luding



*A thesis submitted in fulfilment
of the requirements
for the degree of
Master in Science*

at the

Physics of Fluids Department
Science & Technology Faculty, Enschede, The Netherlands

August 21, 2019

"For small creatures such as we, the vastness is bearable only through love."

Carl Sagan

UNIVERSITY OF TWENTE

Summary

Science & Technology Faculty, Enschede, The Netherlands

Master Thesis

MercuryDPM: From a Chip to Saturn

by Edgar Ortega Roano

This thesis consists of two parts, the first one called the *propeller project*, where we focus on studying the creation of two-dimensional propeller structures in the vicinity of a moonlet orbiting Saturn using the MercuryDPM software. The second part is called the *clogging project*, where, using the same Discrete Element Method software, we investigate the statistics of clogging in a constricted suspension flow in a lab-on-a-chip micro-channel with a bottleneck. Therefore the name *MercuryDPM: From a Chip to Saturn* chosen.

For the *propeller project*, varying the restitution coefficient ϵ of the ring particles, it is found that the transition between propeller and no-propeller state is smooth. Following the idea of Michikoshi & Kokubo [12], we propose an arbitrary criterion to discern between these two states: if the ratio between the maximum and minimum coarse grained density is greater than two, we consider that there exists a propeller. This happens at $\epsilon \approx 0.70$, where the inelasticity $1 - \epsilon^2 \approx 1/2$. Meaning that simulations where $\epsilon < 0.70$ or, equivalently, $1 - \epsilon^2 > 1/2$ tend to show a propeller structure for a packing fraction $\phi = 0.01$. A different criterion is proposed by comparing the Hill velocity v_H with the velocity fluctuation in y direction δv_y , following the work done by Salo [43], one can consider that a propeller is present when $v_H > \delta v_y$, which gives $\epsilon \approx 0.62$ as an approximate upper limit for the existence of these structures for the same packing fraction.

Focusing now on a completely different length scale, for the *clogging project*, we replicate qualitatively the clogging behaviour found by Marin et al. [44] in a constricted suspension flow, using a simple approach where only the contact forces between particles and the drag force caused by the fluid inside the channel are needed. By counting the number of particles s that escape the constriction before a clog occurs, it is found that the probability of clogging is well fitted by an exponential distribution, being the agreement better after the region of small avalanches, i.e., s bigger than the mode. This implies that clogging is a Poisson process, similar to what is found in dry granular media [48, 49, 50], meaning that two clogging events are independent of each other and each particle that passes through the constriction has the same probability of being the last escapee. It is found that the mean number of escapees increases exponentially with the ratio between the constriction size D and the particle diameter d , when we are far from the intermittent regime $D/d < 5$.

Acknowledgements

We listen about the success of great scientists, past geniuses and known professors; people that were a watershed and turning point in their epoch, and one starts to wonder how their lives were. Was it always so straightforward? Did the theories and equations come naturally into their minds?

Throughout the pass of these years, since I got involved in science, I have met many great people. Amazing professors that captivate you with classes full of enthusiasm, classmates that became friends after sharing many days together at the university; but I noticed the same constant for all of them, life was definitely not straightforward.

Some deal with hours in traffic and waking up at 5 am just to be on time for the first class in the morning; some others deal with illnesses, accidents, depression and obstacles that hold up their plans. We deal with problems everyday, problems in school, in our families, within ourselves and problems literally on the textbooks that we need to solve for the assignments. But we are scientists, that is what we do, we solve problems.

The only reason why I mention this is because one will always encounter trouble, but also people who help you. They are out there, but you have to pay attention and be humble enough to ask for help, they are not angels nor saints, just normal people with problems. I took this small section to thank the normal people, great to my eyes, for lending me the necessary help to accomplish my goals, because without them finishing a master would not have been possible to me.

Firstly, I would like to thank the Dutch organisation for internationalisation in education, Nuffic Neso, for the economical support given to me through the program *Orange Tulip Scholarship Mexico 2017-2018*. In particular to the team of Nuffic Neso Mexico, for the help given throughout the process and welcome to the Dutch culture. I thank the University of Twente, for giving me the opportunity to study in an incredible university with amazing professors and first world facilities. I'd like to sincerely express my appreciation to Banamex for the support given through the program *Programa de Jóvenes de Excelencia Banamex de Fomento Social Banamex, ANUIES y SENER* during the process of application and preparation before the start of the master.

I'm grateful for my professors, supervisors and tutors, specially professor Devaraj van der Meer and professor Stefan Luding, who were amazing thesis supervisors always willing to help and give advise. I thank professor Alvaro Marin, with whom I have worked and discussed part of this manuscript. Many thanks to my internship supervisors, professor Matthias Sperl and Juan Petit, for the advises and friendship; I feel thankful for Hao Shi, professor Thomas Weinhart and professor Simon Portegies, for the patience with all my questions and their time. I thank professor Geert Brocks for accepting to be part of the evaluation committee for this thesis.

Many thanks to my friends in Mexico and my friends in the Netherlands, who have helped me many times and taught me that I don't know everything and that we all need of help no matter who you are. I thank my *brother* Ricardo for unconditional support. I thank my family, in particular my grandma, my aunt and Paco. And finally and naturally, I thank my mom and dad, whom I love and always want to make proud ... and they keep reminding me that they are my biggest fans, even though that everything I have accomplished has been because of them.

Contents

Summary	iii
Acknowledgements	v
1 Introduction to the Saturn System	1
1.1 Saturn and its Rings	1
1.2 Propellers	5
1.3 MercuryDPM: Discrete Element Method	6
1.4 AMUSE: Computational Astrophysics	8
1.5 Scope and Outline	8
2 Granular Matter	11
2.1 What is Granular Matter?	11
2.2 Contact Between Particles	12
2.3 Equations of Motion and Linear Contact Model	14
2.3.1 Normal Contact Forces	15
2.3.2 Tangential Contact Forces	17
2.4 Packing Fraction	18
2.5 Summary	18
3 From Discrete Particles to Continuum Fields	21
3.1 Coarse Graining	21
3.1.1 Mass Balance	22
3.1.2 Momentum Balance	24
3.2 Coarse Graining Near Boundaries	27
3.3 Coarse Graining of Body Forces	27
3.4 Coarse Graining of an Isotropic Compression	28
3.5 Summary	31
4 Gravitational Dynamics	33
4.1 The Two Body Problem	33
4.1.1 Conservative Central Force Problem	33
4.1.2 Motion in the Center of Mass Reference Frame	36
4.2 Kepler Frequency	40
4.3 N-body Problem	41
4.3.1 Very Close Titan System	42
4.3.2 A Comment on Symplecticity	43
4.4 Summary	46
5 Motion in a Rotating Reference Frame	47
5.1 General Non-inertial Reference Frames	47
5.2 Rotating Reference Frame of a Moon	51
5.2.1 Forces in the Rotating Reference Frame of a Moon	51

5.2.2	Velocity Shear in the Reference Frame of a Moon	54
5.3	Summary	55
6	Ring Section and Propellers Simulations	57
6.1	Simulations of Ring Sections	57
6.1.1	Lees-Edwards Boundary Conditions	58
6.1.2	Ring Sections and Coarse Graining	59
6.2	Simulations of Propellers	61
6.2.1	Simulations Setup	61
6.2.2	Propellers	62
6.2.3	Coarse Graining of Propeller Simulations	64
7	Clogging in a Constricted Suspension Flow	71
7.1	Constricted Suspension Flow	72
7.1.1	Poiseuille Flow Far from the Neck	73
7.1.2	Poiseuille Flow Near and Inside the Neck	78
7.2	Drag Force	80
7.2.1	Stokes Drag	81
7.3	Summary	85
8	Simulations of Clogging in a Constricted Suspension Flow	87
8.1	Simulations Setup	87
8.2	Results and Statistics of Clogging in a Constricted Suspension Flow	88
9	Conclusions and Outlook	95
9.1	Propeller Project	95
9.1.1	Conclusions	95
9.1.2	Outlook	96
9.2	Clogging Project	98
9.2.1	Conclusions	98
9.2.2	Outlook	98
	Bibliography	101
A	Granular Temperature of a Sheared Gas	105
A.1	Energy Balance Equation	105
A.2	Constitutive Relations and Transport Coefficients	106
A.3	Sheared Granular Gas	107
A.4	Free Cooling Granular Gas	111
B	Coarse Graining Images of Propellers	113
C	Supplemental Material for Clogging in a Constricted Suspension Flow	119
C.1	Drag Equation	119
C.2	Clogging Complementary Plots	121

Chapter 1

Introduction to the Saturn System

1.1 Saturn and its Rings

The rings of Saturn are a system that evolves continuously and whose origin and dynamics are not yet completely understood. There are a myriad of structures inside them, created by different processes and evolving in very distinct time scales, from some days to millions of years. But before deepening into the study of the structures of the rings, let us revise some general physical characteristics of Saturn and give a motivation of why studying its rings is an interesting and mesmerizing choice.

Saturn has been observed with naked eye since ancient times, but it was Galileo Galilei with his home-made telescope that discovered two objects orbiting Saturn in 1610. Decades later, in 1655, Christiaan Huygens found out that these objects were in fact the biggest moon of Saturn, Titan, and a disk of material, the rings. After him, in the 1670's, Giovanni Cassini discovered four more moons and a gap in the disk of material, now known as the Cassini Division. In the modern era there have been a few spacecrafts that conducted flybys near the planet, but it took until 2004 when the Cassini orbiter and the Huygens probe entered Saturn's orbit that a ton of images and data revolutionized our way to see the gas giant.

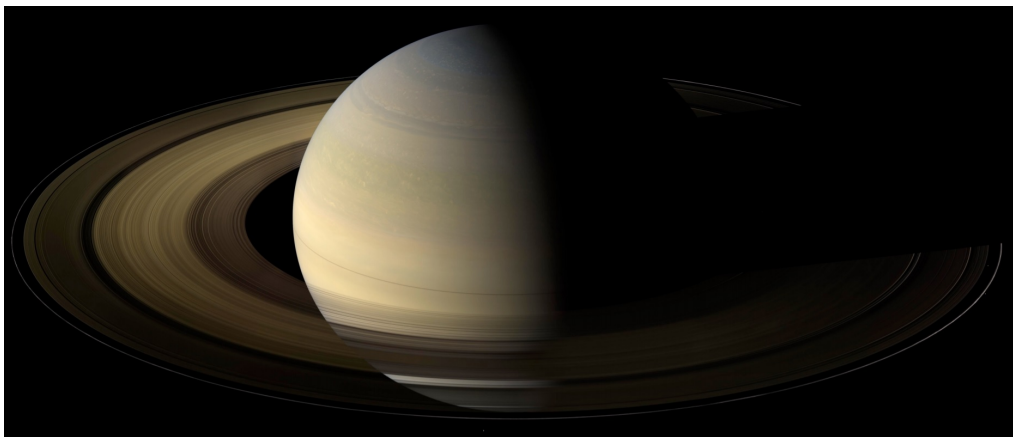


FIGURE 1.1: Saturn a day and a half after its equinox on August 12, 2009. Pictures like this can only be seen a few months before and after Saturn's equinox, which occurs every 15 years. Image taken from [1].

There exist many sources of information out there where you can find anything from fun facts to deep physical manuscripts about Saturn and the Cassini-Huygens mission. Personally, when I first started reading about Saturn and its rings, I found *The Saturn System Through the Eyes of Cassini* [1] very enjoyable. It is an introductory book full of images taken by Cassini, it shows the planet, its rings and its moons as never seen before. Many of the images I show here, Figure 1.1 for example, are taken from this book, and they are also available at the official NASA website for the public <https://www.nasa.gov>.

When it comes to scientific research, my principal sources of information are probably the books *Saturn from Cassini-Huygens* [2] and *Titan from Cassini-Huygens* [3]; these two volumes aim to capture the main scientific results of the Cassini-Huygens mission from orbiting around the Saturn system for 13 years, and were my first scientific approach to the subject.

We can now start to talk about some fundamental facts of Saturn. It is the sixth planet from the Sun and second largest in the Solar System; its mean radius is 58,232 km, with a volume of $8.27 \times 10^{14} \text{ km}^3$ and a mass of $5.68 \times 10^{26} \text{ kg}$. Its origin is still subject of research, but there are two main models: the gas instability model and the core nucleated accretion model [2, 4].

The gas instability model predicts the giant planet origin from the formation of dense clumps in the solar nebular gas disk due gravitational instabilities. In highly massive and turbulent regions of the gas disk, spiral arms form with clumps inside, that collapse under their own gravity into a gaseous planet, similar to how stars form.

As for the core nucleated accretion model, it postulates that the origin of Saturn is due to collisions of planetesimals in a planetary accretion disk. As a result of their inelasticity, the planetesimals clump together until they form a core massive enough to have its own gaseous accretion disk.

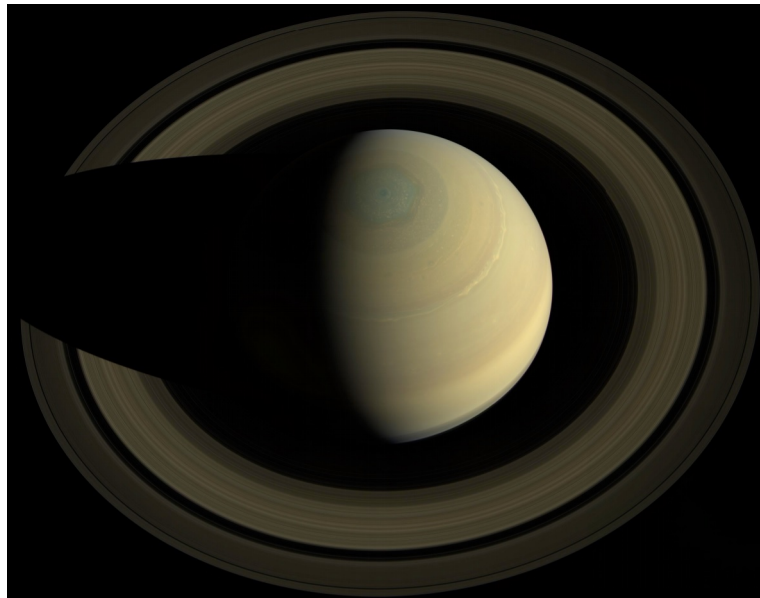


FIGURE 1.2: Cassini flew high above Saturn on October 10, 2013, to give us this beautiful picture of the natural color of the planet. Mesmerizing is the symmetry of the image just to be broken by the shadow that Saturn casts onto its rings. Image taken from [1].

The origin of the rings is also uncertain but some models describe them as leftovers of a circumplanetary disk that were never able to accrete and form a moon due to tidal forces (Roche limit). There is another theory that the circumplanetary ring was able to form a satellite even inside the Roche limit, but a later collision destroyed it and the debris disk did not re-accrete into a new satellite [2]. Cassini gave us a beautiful image of the rings in all their magnificence shown in Figure 1.2.

Saturn has 62 known moons and far more rings than letters of the alphabet, but the rings can be broadly grouped into dense rings (A, B, C) and tenuous rings (D, E, G); the Cassini Division separates rings A and B.

Saturn's dense rings consist mainly of icy particles, which can be as small as marbles (≈ 0.1 m) or hundreds of meters big, which might as well be called moonlets; while Saturn's tenuous rings are composed by dusty particles ($\approx 100 \mu\text{m}$). One of the peculiar characteristics of the rings is that they can be thousands of kilometres wide ($\approx 20,000$ km), but they are very slender, just tens of meters thin, as seen in Figure 1.3. We can exploit this almost-two-dimensionality if we want to study them using astrophysical and particle simulations, since a 3D simulation is naturally more computationally expensive.

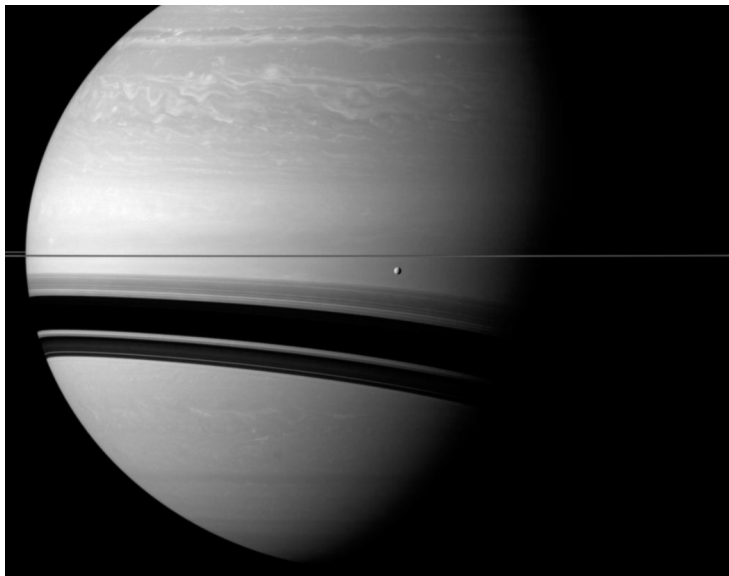


FIGURE 1.3: Side view of Saturn on December 7, 2011, where we are able to appreciate the slenderness of its rings. One of the moons, Tethys, orbits in front of the rings and the shadows cast by them on Saturn. Image taken from [1].

The moons, moonlets and particles in the ring orbit Saturn in almost circular orbits with an angular velocity given by the Kepler Frequency

$$\Omega = \sqrt{\frac{GM_S}{r^3}}, \quad (1.1)$$

expression that will be derived later in Chapter IV, with $G = 6.674 \times 10^{-11} \text{m}^3 / (\text{kg s}^2)$ the gravitational constant, $M_S = 5.68 \times 10^{26} \text{kg}$ the mass of Saturn and r the radial distance from the center of Saturn to the body in question [2]. Equation (1.1) already tells us an important feature about the rings: the particles in the inner-most

rings orbit considerably faster than the particles in the outer-most rings due to the dependence of the angular velocity on the radial distance, $\Omega \propto r^{-3/2}$.

This difference in the particles velocity induces a constant shear in the mean ring plane. If we describe Saturn's rings as a granular gas [5], we can say that this shear *heats up* (in a granular sense, i.e., by the creation of kinetic energy fluctuations) the ring, by inducing collisions between the particles; nevertheless, because of their inelastic nature, the particles are kept inside in a quasi-two-dimensional plane. If a particle is displaced out of the mean plane, it would travel in an inclined orbit and would have to cross the ring, losing energy each time due to the inelastic collisions until it gets back into the plane.

It is the balance between the shear and the inelastic collisions what has kept Saturn's rings stable for millions of years. It is also the reason of their slenderness; if the particles were completely elastic, the thickness of the rings would increase indefinitely and the rings would be destroyed [5].

But collisions are not the only kind of interaction that the particles undergo. Naturally they feel the gravity of Saturn, but also, in smaller magnitude, the gravity of the Sun or the gravity of Titan (biggest moon of Saturn) for example; the particles of the rings even feel a tiny gravitational interaction due to other particles in the ring, interaction that we call *self-gravity of the ring*. Gravity corresponds to a so-called *long-range interaction* or *long-range force* [6]. Its range is infinite and even though Saturn's gravity exceeds in magnitude any other gravitational interaction due to other planets or the sun, there are objects big and close enough inside the rings that can perturb them in such a way to create complex structures.

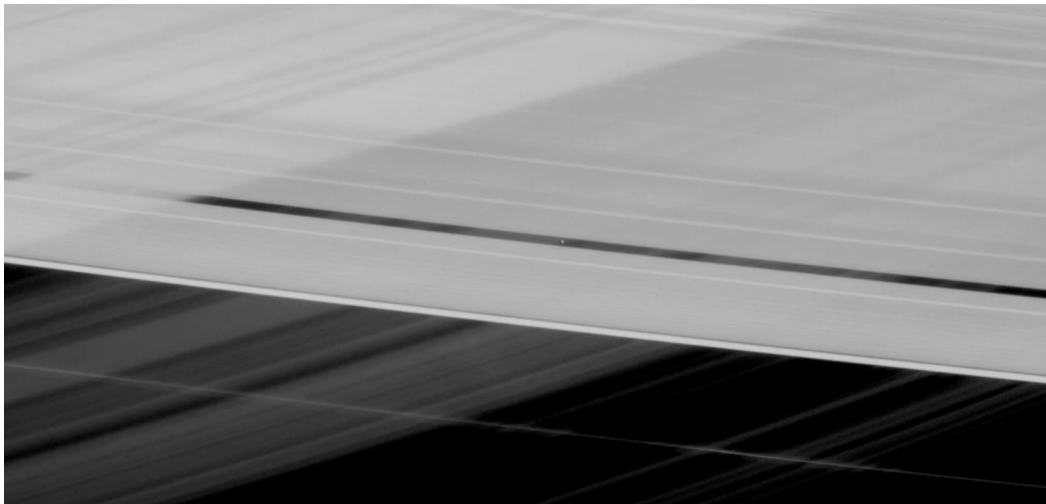


FIGURE 1.4: Saturn's A ring showing a game of lights and shadows. At the center, a shepherd moon, Pan, keeps the Encke gap open. Image taken from [1].

One example are the *shepherd moons*, whose sizes usually are in the order of kilometres. It is better to explain why they are called *shepherd* if we look at particular cases. Look for example at Figure 1.4, where we see Saturn's A ring divided by a gap, the so-called Encke gap, in the middle of the image and within the gap we see a tiny dot, which is Pan, a shepherd moon; Pan has a mean radius of 14.1 km and keeps the Encke gap open through gravitational scattering and direct collision with

the particles of the ring. Another case is the moon called Daphnis, that has a mean radius of 3.8 km and keeps the Keeler gap open. One of the biggest shepherd moons is the one called Prometheus, which has a mean radius of 43.1 km and constrains the extent of the inner edge of Saturn's F Ring. In Figure 1.5 we see Prometheus orbiting near the F ring leaving behind perturbations on the density of the rings. These three moons *shepherd* the particles in the rings, keeping divisions open and controlling their extent [1].

However, there exist small moons (moonlets) that are not big enough to keep a gap open, but big enough to perturb the particles around it visibly, usually creating what it is called a propeller; the main goal of the *propeller project* is to study these structures.

1.2 Propellers

Propellers are S-shaped density structures in the rings caused by embedded moonlets due to gravitational scattering and direct collision. They have been predicted theoretically by Spahn and Sremčević (2000) [7], and Sremčević et al. (2002) [8]. Since their prediction, and discovery by the spacecraft Cassini, there has been continuous research about propellers; names like Spahn, Sremčević, Salo and Seiß are common to see when one is looking for articles about the subject. One of the latest articles where they all collaborated was *Hydrodynamic Simulations of Moonlet-induced Propellers in Saturn's Rings: Application to Blériot* [9], from where I found my main motivation to start working on propeller simulations.

In Figure 1.6 we can see an image taken by Cassini of a propeller in Saturn's A ring; it has been nicknamed "Santos-Dumont," after the pioneering Brazilian-French aviator. The distance between the wave crests tells us the width of the gap, that is about 2 kilometres, which in turn reveals the mass of the central moonlet, comparable to that of a snowball about 1 kilometre in diameter [10].

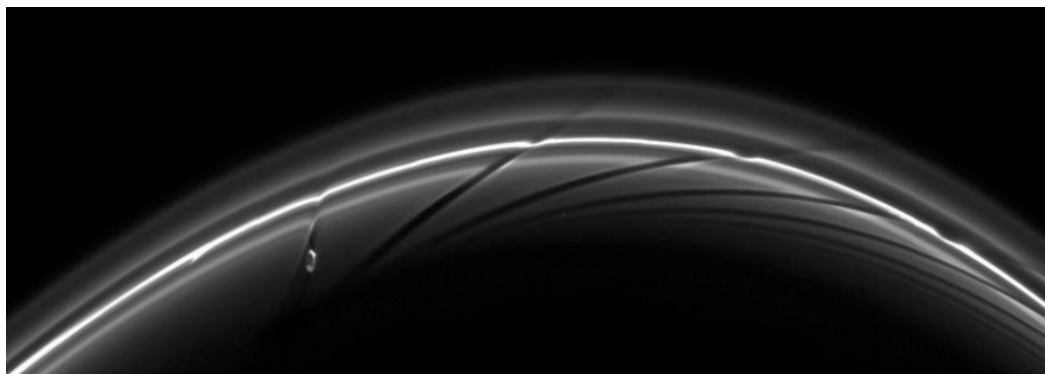


FIGURE 1.5: Saturn's moon Prometheus orbiting near the F ring, leaving behind perturbations, streamer-channels, on the ring. Image taken from [1].

The biggest propeller found until known has been called informally "Blériot", named after Louis Blériot, a French engineer and aviator who was the first person to fly across the English Channel [11]. In Figure 1.7 we see an image of Blériot taken by

Cassini, to give an idea of how big it is, every pixel is around 500 meters. The moonlet is not resolved with the resolution of the picture, but thanks to the propeller structure we are able to tell its approximate size, which is ≈ 900 m in diameter [9].

There exist many ways to study propellers: theoretically, Spahn & Sremčević [7]; with hydrodynamic simulations, Seiß et al. [9]; with N-body simulations, Michikoshi & Kokubo [12]; or with a more stochastic approach, Rein & Papaloizou [13]. They all have their personal codes developed after years of work and research. This manuscript aims to study Saturn's rings and specifically the propeller formation with the tools that I have available and learnt during my studies at the University of Twente. We will follow the work, take the motivation and inspiration from the scientists above mentioned, with a slightly different approach, using Discrete Element Method (DEM) simulations to investigate Saturn's rings and its structures. There are pros and cons for each method and we will review the advantages of using DEM and possible further applications and extensions to this work.

1.3 MercuryDPM: Discrete Element Method

The first powerful tool that will help us simulate Saturn's rings (and micro-particles inside a channel for the second part of this thesis) is the open source code MercuryDPM. It was created to perform discrete particle simulations, a method often referred to as the Discrete Element Method (DEM), but the developers prefer the name Discrete Particle Method (DPM).

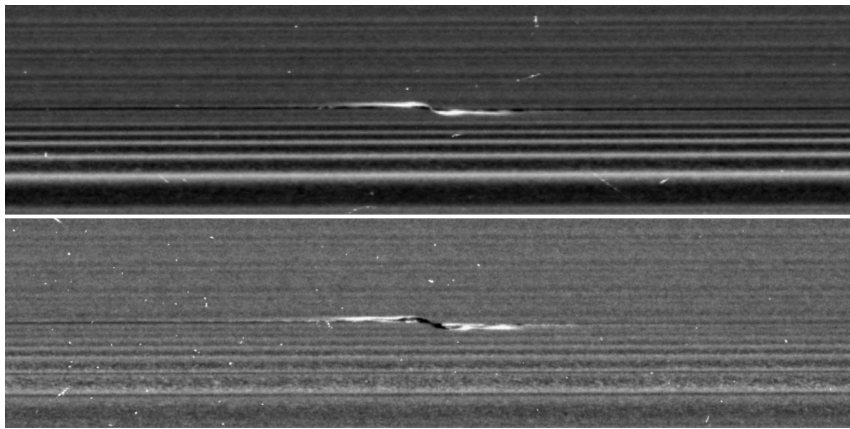


FIGURE 1.6: On February 21, 2017, Cassini captured these images of a propeller in the A ring, showing it on opposite sides of the rings. The top image looks toward the rings' sunlit side, while the bottom image shows the unilluminated side. Image taken from [10].

It simulates the motion of particles, or atoms, by applying forces and torques that stem either from external body forces or from particle interaction laws. For granular particles, these are typically contact forces, while for molecular simulations, forces typically stem from interaction potentials. The code has been developed extensively for granular applications, but could be adapted to include long-range interactions as well. It was started by Anthony Thornton and Thomas Weinhart, and has been developed by many people since it began [14].

The great advantage about MercuryDPM is that it is C++ based and easy to learn, it uses a hierarchical grid algorithm to effectively compute interaction contact forces, even for highly poly-dispersed particles; meaning that it is fast even when a high number of particles of different sizes come into contact. It has a built-in advanced coarse-graining statistical package to extract continuum fields such as density, velocity, structure and stress tensors, either during the computation or as a post-processing step.

The particles in the rings are highly poly-dispersed and collide quite often, and by implementing the force due to Saturn and the moonlet into MercuryDPM, we would have a fast code that simulates particles in the vicinity of the moonlet. A disadvantage is that, if we were to implement self-gravity of the ring, the computation time would scale as $\mathcal{O}(N^2)$, where N is the number of particles in the simulation, making the code very slow.

Further explanation about particle contact models and coarse graining will be given in the following chapters. For more information about the capability of the code and further examples, we will refer to the article by Thornton, Weinhart, Luding & Bokhove [15] and the official MercuryDPM website: <http://mercurydpm.org/>.

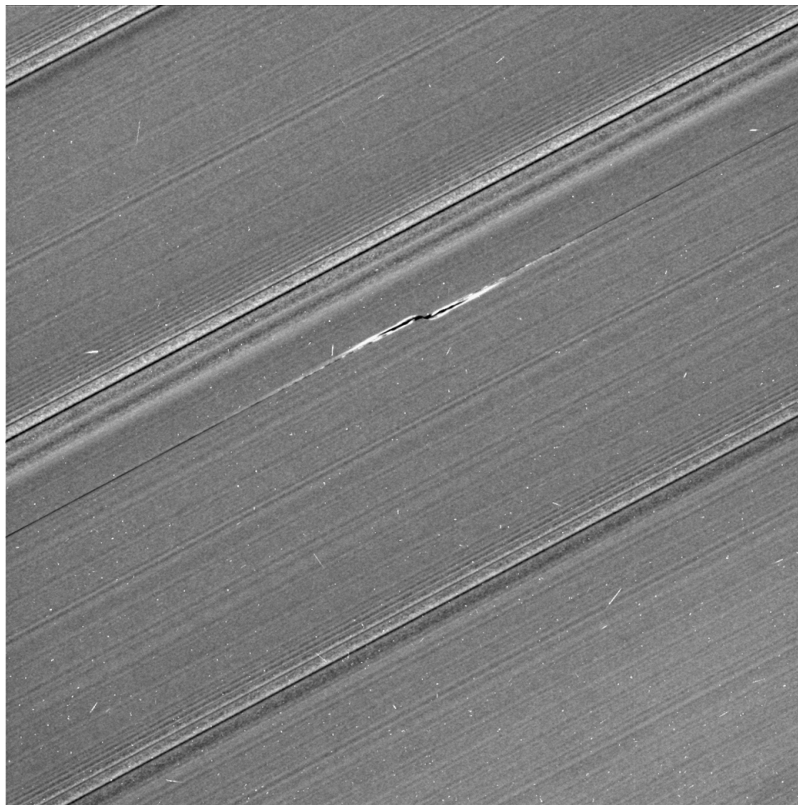


FIGURE 1.7: Cassini's best image of a propeller, informally called Ble-riot, which is the biggest propeller found until now in the A ring. Image taken from [11].

1.4 AMUSE: Computational Astrophysics

The second powerful tool that we will use to study Saturn's rings is called AMUSE, which stands for Astrophysical Multipurpose Software Environment. It is a software framework for astrophysical simulations, in which existing codes from different domains, such as stellar dynamics or stellar evolution, can be easily coupled. It uses Python to interface with different existing numerical codes.

The great advantage of AMUSE is that it incorporates multiple community codes from four fundamental domains: stellar evolution, gravitational dynamics, hydrodynamics, and radiative transfer. Naturally, we are interested in the gravitational dynamics functionality, but it is possible to combine more of the community codes for a more complex simulation. A disadvantage is that collision handling between particles is rather rudimentary, without contact force models or interaction laws other than the four fundamental domains above mentioned.

However, the N-body integrators from the gravitational dynamics domain are splendid, they can scale as $\mathcal{O}(N \log N)$, $\mathcal{O}(N)$ or $\mathcal{O}(N^4)$ depending on the method and required accuracy. One can choose between pure N-body codes, direct N-body codes or approximate methods, suitable for different number of particles with different numerical schemes. For more information about AMUSE we will refer to the book written by Portegies & McMillan [16] or the official website for the open source code: <http://amusecode.org/>.

1.5 Scope and Outline

When I started doing my research, I found myself looking for specific information referenced from an article, that was referenced from another article and so on. In that sense, finding the origin of an equation can be tedious if you have never seen it before; that is why one of the goals of this thesis is to be as theoretically self-contained as possible, meaning that all the important equations are derived, making a concise but self-contained summary of each article and book referenced.

That comes with a cost. Some of the chapters may contain a lot of equations, that can be thought as *basic knowledge*, but from my experience, scientists from a specific field will not necessarily know or remember the *basic knowledge* from another field. As an example, this thesis uses knowledge from the fields of celestial mechanics, hydrodynamics and granular matter. That is why the theoretical chapters come with a summary at the end, to make a quick recapitulation of the important concepts and equations derived.

When working in such a multi-disciplinary field of research, as it is the case for Saturn's rings, another minor problem arises, namely the use of notation. Some of the different areas use similar notation for slightly distinct parameters. Symbols like r , v and ω are broadly used and known to represent the position, velocity and angular velocity respectively; but other examples like γ , η or μ might be used for dissipation or viscosity indistinctly and vary from author to author. I tried to make the notation in this thesis as consistent as possible, making clear what each symbol represents in every chapter. The theoretical chapters are also self-contained, meaning that they can be used as a quick help or reference without the necessity of reading the other ones.

This first chapter starts with an introduction to the Saturn system and the structures that can be found in it, with many beautiful images taken by Cassini. We also gave a quick description of the computational tools used to study the rings and micro-particles, MercuryDPM and AMUSE.

The second chapter has been named *Granular Matter*, it gives a brief introduction of the concept of granular materials and some examples in real life. We present the concept of the overlap between the particles and its dynamics through the easiest contact model, the Linear Spring Dashpot Model. We pose the equations of motion for the translational and rotational degrees of freedom that MercuryDPM solves at each time step in the simulations.

In the chapter *From Discrete Particles to Continuum Fields*, we develop the basic theory of Coarse Graining and apply it to the density, momentum, velocity and stress fields. The equations of continuity and momentum balance are derived with extensions to coarse graining near boundaries and body forces.

Starting with the theory of *Gravitational Dynamics*, the fourth chapter gives us an introduction to the two body problem and the N-body problem. We derive the most important parameter of the *propeller project*, the Kepler Frequency and give a didactic example using the framework of AMUSE.

We continue with the gravitational dynamics but now applying the Newtonian formalism to the *Motion in a Rotating Reference Frame*. General equations of motion for non-inertial reference frames are derived and then applied for the case of motion in the vicinity of a moon orbiting Saturn, or any planet for that matter.

After the last two preliminary chapters, in Chapter VI we apply the astrophysical concepts to simulate ring sections and reproduce the formation of propellers varying the coefficient of restitution. The coarse graining built-in tool of MercuryDPM is used to a better analysis of the data obtained.

In Chapter VII we start working on a completely different scale: Microfluidics. We develop the basic tools needed to simulate micro-particles flowing through a rectangular channel with a bottle neck. Two main elements are needed for this, the expression for the flow velocity and the drag force affecting the particles. A long discussion is made about the drag force and the most appropriate expression for it.

We use MercuryDPM to simulate a constricted suspension flow in Chapter VIII. Since MercuryDPM works with forces, we make use of the drag force on particles, derived in the preceding chapter, to explore the statistics of clogging in a micro-channel neck.

Finally we conclude both projects and give an outlook of can be done for future research.

Chapter 2

Granular Matter

2.1 What is Granular Matter?

Thinking about *Granular Matter*, Saturn's rings would not be the first example that comes to our mind. The truth is that probably we first think of sand and grains, but granular materials are pretty much everywhere in our daily life. From the sugar that we put in our coffee or the salt that we add to our food to huge avalanches and landslides.

Even though the components of granular materials can be tiny solid particles, together as a system they can behave as a solid, liquid or gas; it is not complicated to find examples of these three states of granular matter. The sand that is static in a pile acts like a solid, but it can also run down on the surface of the dunes of the desert like a liquid or be in a gaseous state in the form of a sandstorm.

The macroscopic constituents of granular matter need not be small particles, it is all relative to how you look at it. The boulders falling within a landslide can be as huge as a truck and the icy particles of Saturn's rings range in sizes from a few centimetres to hundreds of meters [2], but when you look at them from far enough they are small compared to the whole structure they form.

Then, with all this variety of examples, see Figure 2.1, it is important to define what we mean with *granular media*. Following the definition of Andreotti et al. [5], we consider granular media as the collection of rigid or semi rigid macroscopic particles whose sizes are greater than $100\ \mu\text{m}$, with the important characteristic that they dissipate energy with every collision between each other, meaning that they are inelastic; their inelasticity is based on the fact that these particles are themselves macroscopic bodies with many internal degrees of freedom [17].

One certain and inevitable situation that happens in the three states of granular matter is the contact between its components, i.e., contacts between grains. In order to characterize a system with many particles, we specify (as Herrmann et al. did [18]) only the interaction between two of the components, assuming many-body interactions to result from the sum of the two-particle forces. We can assume either that the particles are hard so that no overlap is admissible between them, or that they are *soft particles*, such that there exist an overlap when they come into contact. The next two sections are a summary of the chapter *Collisions & Contacts Between Two Particles* by Stefan Luding [18], where we are going to define the overlap and the contact model for the grains.



FIGURE 2.1: Examples of granular matter. Dunes, grains, sandstorms, planetary rings, pills and even avalanches are part of what we consider granular matter.

2.2 Contact Between Particles

In order to characterize the contact between two spherical particles, we define the overlap δ as a measure of deformation

$$\delta = (a_i + a_j) - (\mathbf{r}_i - \mathbf{r}_j) \cdot \hat{\mathbf{n}}, \quad (2.1)$$

being a_i and a_j the radii of the particle i and j respectively, \mathbf{r}_i and \mathbf{r}_j their positions with respect to an origin of coordinates and

$$\hat{\mathbf{n}} = \hat{\mathbf{n}}_{ij} = \frac{(\mathbf{r}_i - \mathbf{r}_j)}{|\mathbf{r}_i - \mathbf{r}_j|}, \quad (2.2)$$

a normal unit vector that points from the center of particle j to the center of particle i , see Figure 2.2.

To get the magnitude of the normal relative velocity, we need to project the relative velocity of the contact point of particles i and j ,

$$\mathbf{v}_{ij} = \mathbf{v}_i - \mathbf{v}_j - (a_i \boldsymbol{\omega}_i + a_j \boldsymbol{\omega}_j) \times \hat{\mathbf{n}}, \quad (2.3)$$

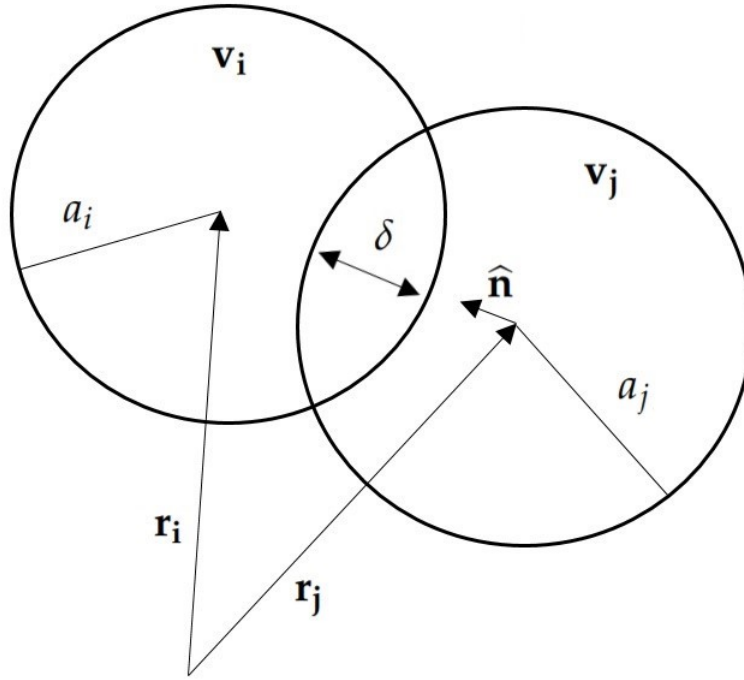


FIGURE 2.2: An illustration of two interacting particles i and j , where the interaction is quantified by the overlap δ . The position of the centres of mass is given by \mathbf{r}_i and \mathbf{r}_j for the particles with radii a_i and a_j colliding with velocities \mathbf{v}_i and \mathbf{v}_j respectively. The unit vector $\hat{\mathbf{n}}$ points from the center of the particle i to the center of the particle j .

in the direction of $\hat{\mathbf{n}}$

$$v^n = -\mathbf{v}_{ij} \cdot \hat{\mathbf{n}} = -(\mathbf{v}_i - \mathbf{v}_j) \cdot \hat{\mathbf{n}}.$$

Naturally \mathbf{v}_i is the linear velocity and $\boldsymbol{\omega}_i$ the angular velocity of particle i , and equivalently for j . According to this definition, when the particles are approaching the magnitude of the normal velocity is positive, $v^n > 0$; and negative, $v^n < 0$, when the particles are separating.

By looking at equation (2.1), we realize that v_n is just the derivative of the overlap with respect to time, $\dot{\delta}$

$$v^n = -\mathbf{v}_{ij} \cdot \hat{\mathbf{n}} = -(\mathbf{v}_i - \mathbf{v}_j) \cdot \hat{\mathbf{n}} = \dot{\delta}, \quad (2.4)$$

since

$$\frac{d\delta}{dt} = \frac{d}{dt} [(a_i + a_j) - (\mathbf{r}_i - \mathbf{r}_j) \cdot \hat{\mathbf{n}}] \quad (2.5)$$

and therefore

$$\begin{aligned}\dot{\delta} &= -(\dot{\mathbf{r}}_i - \dot{\mathbf{r}}_j) \cdot \hat{\mathbf{n}}, \\ &= -(\mathbf{v}_i - \mathbf{v}_j) \cdot \hat{\mathbf{n}}.\end{aligned}\quad (2.6)$$

Naturally, we assumed that a_i and a_j do not change, as it can happen in the case of plastic deformation, swelling or changes due to temperature. This is not the only assumption made, we also assume that the overlap is small compared to the radii of the particles, $\delta \ll a_i, a_j$.

2.3 Equations of Motion and Linear Contact Model

If we know the total force \mathbf{f}_i acting on a particle i due to other particles, walls or external forces, the granular matter problem is reduced to solve Newton's equation for the translational

$$m_i \frac{d^2}{dt^2} \mathbf{r}_i = \mathbf{f}_i, \quad (2.7)$$

and the rotational degrees of freedom

$$I_i \frac{d}{dt} \boldsymbol{\omega}_i = \mathbf{t}_i. \quad (2.8)$$

Here m_i is the mass of the particle and \mathbf{r}_i its position vector. The moment of inertia is denoted by I_i and its angular velocity is $\boldsymbol{\omega}_i$. For the translational motion, the change in linear momentum is caused by the total force \mathbf{f}_i , which we can write as the sum of the total contact forces \mathbf{f}_i^c and the external body forces \mathbf{f}_i^{ext} , such as gravity

$$\mathbf{f}_i = \sum_c \mathbf{f}_i^c + \mathbf{f}_i^{ext}, \quad (2.9)$$

for the rotational motion, the change in angular momentum is due to the total torque applied to the particle \mathbf{t}_i

$$\mathbf{t}_i = \sum_c (\mathbf{l}_i^c \times \mathbf{f}_i^c + \mathbf{q}_i^c), \quad (2.10)$$

where \mathbf{l}_i^c is the vector that connects the center of mass of particle i with the contact point, and \mathbf{q}_i^c any other torques different than the one caused by the tangential force, for example by rolling and torsion.

The force that the particle i feels due to any other particle j can be decomposed into a normal f^n and tangential part f^t

$$\mathbf{f}_i^c = \mathbf{f}_{ij}^c = f^n \hat{\mathbf{n}} + f^t \hat{\mathbf{t}}. \quad (2.11)$$

We already introduced the normal vector $\hat{\mathbf{n}}$, but the tangential vector is given by

$$\hat{\mathbf{t}} = \frac{\mathbf{v}^t}{|\mathbf{v}^t|}, \quad (2.12)$$

with the tangential relative velocity

$$\mathbf{v}^t = \mathbf{v}_{ij} - \mathbf{v}^n \quad (2.13)$$

and the normal relative velocity $\mathbf{v}^n = -\hat{\mathbf{n}}(v^n)$.

We will now discuss the contact models used in this thesis to describe the normal and tangential forces.

2.3.1 Normal Contact Forces

The first and easiest contact model explained by Stefan Luding [18] is the so called Linear Spring Dashpot Model (LSD), which tells us that the normal force on a particle due to the contact with a second one has a repulsive elastic force part

$$f_{el}^n = k\delta, \quad (2.14)$$

where k is the spring constant, and a dissipative one

$$f_{diss}^n = \gamma v_n, \quad (2.15)$$

with γ being a viscous damping constant.

Now we are in search of an equation that describes the evolution of the overlap during the contact time ($0 \leq t \leq t_c$) and an expression for the contact time itself, since we will use it to determine the time step of the numerical computation. We begin by writing the normal component of Newton's second law for two frictionless particles i and j in contact:

$$\frac{d}{dt} \mathbf{v}_i \cdot \hat{\mathbf{n}} = \frac{f_i^n}{m_i}, \quad (2.16)$$

$$\frac{d}{dt} \mathbf{v}_j \cdot \hat{\mathbf{n}} = \frac{f_j^n}{m_j}, \quad (2.17)$$

where f_i^n is the normal force felt by that particle. In the case of a monodisperse system (i.e. the same size for all particles in the packing, $a_i = a_j$) the masses are $m_i = m_j = m$. Now by subtracting equation (2.16) from equation (2.17) we obtain

$$\frac{d}{dt} (-\mathbf{v}_i + \mathbf{v}_j) \cdot \hat{\mathbf{n}} = -\frac{f_i^n}{m_i} + \frac{f_j^n}{m_j}, \quad (2.18)$$

if we notice that

$$\frac{d}{dt}(-\mathbf{v}_i + \mathbf{v}_j) \cdot \hat{\mathbf{n}} = \frac{d}{dt}v_n = \ddot{\delta},$$

then

$$\ddot{\delta} = -\frac{f_i^n}{m_i} + \frac{f_j^n}{m_j}, \quad (2.19)$$

and by Newton's third law $f_j^n = -f_i^n$, equation (2.19) becomes

$$\ddot{\delta} = -\frac{f_i^n}{m_i} + \frac{f_j^n}{m_j} = -f_i^n \left(\frac{1}{m_i} + \frac{1}{m_j} \right), \quad (2.20)$$

or rearranging and defining the reduced mass $m_{ij} = \frac{m_i m_j}{m_i + m_j}$

$$\ddot{\delta} = -f_i^n \left(\frac{m_i + m_j}{m_i m_j} \right) = -\frac{f_i^n}{m_{ij}}. \quad (2.21)$$

Now we can insert the force model (LSD)

$$f_i^n = k\delta + \gamma\dot{\delta}, \quad (2.22)$$

into equation (2.21) to obtain:

$$\begin{aligned} \ddot{\delta} + \frac{\gamma}{m_{ij}}\dot{\delta} + \frac{k}{m_{ij}}\delta &= 0, \\ \ddot{\delta} + 2\eta\dot{\delta} + \omega_0^2\delta &= 0. \end{aligned} \quad (2.23)$$

We have defined the effective viscosity as

$$\eta = \frac{\gamma}{2m_{ij}}, \quad (2.24)$$

and the oscillation frequency of an elastic oscillator

$$\omega_0^2 = \frac{k}{m_{ij}}. \quad (2.25)$$

Equation (2.23) is a linear second order differential equation corresponding to a damped oscillator, more specifically the underdamped case when $2\eta < \omega_0^2$, and has the solution

$$\delta(t) = \left(\frac{v_0}{\omega} \right) e^{-\eta t} \sin \omega t, \quad (2.26)$$

with v_0 the initial relative velocity $v_0 = \dot{\delta}(0)$ and ω the oscillation frequency of the damped oscillator

$$\omega = \sqrt{\omega_0^2 - \eta^2}. \quad (2.27)$$

Now we can finally write the contact time as:

$$t_c = \frac{\pi}{\omega}, \quad (2.28)$$

which is valid as long as $\eta < \omega_0$. In DEM the time step of the simulations is usually set to $t_c/50$ or even $t_c/100$ in order to resolve the collisions between particles accurately.

Taking the derivative with respect to time of equation (2.26)

$$\dot{\delta}(t) = \left(\frac{v_0}{\omega}\right) e^{-\eta t} [\omega \cos \omega t - \eta \sin \omega t], \quad (2.29)$$

we can obtain the final relative velocity v_f by evaluating at the contact time, since $v_f = \dot{\delta}(t_c)$, then

$$v_f = \dot{\delta}(t_c) = -v_0 e^{-\pi\eta/\omega}. \quad (2.30)$$

We define the coefficient of restitution ϵ as

$$\epsilon = -\frac{v_f}{v_0} = e^{-\pi\eta/\omega} = e^{-\eta t_c}, \quad (2.31)$$

where an $\epsilon = 1$ corresponds to a completely elastic collision between particles and $\epsilon = 0$ is completely inelastic.

2.3.2 Tangential Contact Forces

The tangential force is coupled to the normal force via the Coulomb's law of friction. Where for the static case

$$f^t \leq f_C^s = \mu_s f^n, \quad (2.32)$$

and the dynamic case

$$f^t = f_C^d = \mu_d f^n. \quad (2.33)$$

The parameters μ_s and μ_d are called the static and dynamic friction coefficients respectively; in general they follow $\mu_d \leq \mu_s$.

In analogy to the normal viscous force, for the tangential viscous force we have

$$f^t = -k_t \xi - \gamma_t v^t, \quad (2.34)$$

where ξ is the tangential displacement, k_t the tangential stiffness, γ_t the tangential dissipation and v^t the magnitude of the tangential relative velocity given by equation (2.13).

The implementation in a simulation of these contact forces is far from trivial and out of the scope of this manuscript. Thankfully, MercuryDPM integrates the equations of motion and forces for us, if the reader is interested in knowing more about the implementation, rolling, torsion and more contact models available in MercuryDPM, I will refer to Taghizadeh et al. [19].

2.4 Packing Fraction

One important quantity that characterizes a packing of granular matter is the volume fraction, also called packing fraction and it is defined, for example by Andreotti et al. [5], as the ratio of the volume occupied by the particles to the total volume occupied by the packing:

$$\phi = \frac{V_{particles}}{V_{total}}. \quad (2.35)$$

Naturally in 2D it is not the volume but the area, so

$$\phi = \frac{A_{particles}}{A_{total}}. \quad (2.36)$$

The packing fraction runs from 0 to 1, where 0 means there is no particles and 1 means they occupy the whole space of the packing.

In the community of astrophysics a similar concept is defined, the *optical depth*, which will be defined and discussed in Chapter VI.

2.5 Summary

In this section we made a definition of what is granular matter and gave examples of its three states: solid, liquid and gaseous. We discussed the contacts between particles that compose the granular material and defined the overlap as a measure of deformation when two particles are in contact

$$\delta = (a_i + a_j) - (\mathbf{r}_i - \mathbf{r}_j) \cdot \hat{\mathbf{n}}, \quad (2.37)$$

where a_i and a_j are the radii of the particles and \mathbf{r}_i and \mathbf{r}_j their respective position vectors with $\hat{\mathbf{n}}$ the normal unit vector pointing from the particle i to j .

We explained the easiest contact model, the so called Linear Spring Dashpot model (LSD). Afterwards, we derived the contact time

$$t_c = \frac{\pi}{\omega}, \quad (2.38)$$

and the coefficient of restitution

$$\epsilon = e^{-\eta t_c}. \quad (2.39)$$

The contact time is an important parameter for the simulations in MercuryDPM, as it dictates the time step. Normally one sets the time step as $t_c/50$ in order to resolve the collisions accurately. If we were to set the time step bigger, we would encounter numerical instability problems.

We defined the packing fraction ϕ in 3D and 2D as the space taken by the particles over the total space available in the container.

Chapter 3

From Discrete Particles to Continuum Fields

In order to formulate continuum models, we need to validate and calibrate them with discrete experimental or numerical data. For this, there are different mapping methods that accurately obtain continuum fields (like density, momentum or stress) from discrete data of individual elements (such as their positions, velocities, orientations and forces). The mapping technique that we will present here is an extension to the micro-macro transition method called coarse graining. Besides validating numerical data, coarse graining also helps us to reduce the amount of it and to make a faster solution analysis, in particular, we will use the coarse graining theory to analyse the results of the Saturn's rings simulations later in Chapter VI.

In Section 3.1, we will go through the work done by Goldhirsch (2010) [20] to derive the continuity and conservation of momentum equations; then, in Section 3.2, we will quickly revise the case of coarse graining near boundaries done by Weinhart et al. (2012) [21]; in Section 3.3, we are going to take a glimpse at the work done by Weinhart et al. (2013) [22] and Tunuguntla et al. (2016) [23], for the extension of coarse graining with body forces; finally, in Section 3.4, we show an exemplar problem to apply the concepts, an isotropic compression to a 2D disks packing.

3.1 Coarse Graining

The main purpose of coarse graining is to produce continuum fields and equations of motion out of microscopic dynamics. But first, we need to choose and define a set of continuum fields for which the equations will be derived. Normally it is chosen by symmetries, conservation laws or measurability. The fields should be defined everywhere in the space occupied by the system and the equations of motion must depend only on the chosen set of fields.

The results are general, but there are simplifying assumptions made for convenience. It is assumed that the particle interactions are binary and additive; the particles are convex, such that each interacting pair has only one contact area that is modelled as a contact point; the force distribution acting on the contact area can be replaced by a contact force at the corresponding contact point or a torque, meaning that the particles are quite stiff or at least not *too soft*. Effects such as attrition and breakup are ignored as well as plastic deformation. The resulting fields are valid for a single element and time step, then, there is no need of ensemble averaging.

We are going to derive the mass balance (continuity equation) and the momentum balance equation for the density and velocity fields as done by Goldhirsch [20]. But before that, in the first chapter, I mentioned about the similarity in the names of the variables, in particular this section uses practically the same notation as Chapter II, but to make it clear, we will start with some labelling.

Consider a granular packing with N particles (it can be a granular solid, liquid or gas) where the position of the particle i of mass m_i is given by the vector $\mathbf{r}_i(t)$, dependent on time; in index form this is written as $r_{i\alpha}$. This particle has a velocity defined by $\mathbf{v}_i(t) \equiv \dot{\mathbf{r}}_i(t)$. The relative position between particle i and another particle j is denoted as $\mathbf{r}_{ij}(t) = \mathbf{r}_i(t) - \mathbf{r}_j(t)$ and the relative velocity of their centres of mass is $\mathbf{v}_{ij}(t) = \mathbf{v}_i(t) - \mathbf{v}_j(t)$, not to be confused with the relative velocity of the surfaces at the contact point defined in Chapter II.

The total force that particle i feels due to contacts with others is written as $\mathbf{f}_i(t)$, if the force acting on i due to the particle j is $\mathbf{f}_{ij}(t)$, then, the total force that particle i feels is $\mathbf{f}_i(t) = \sum_j \mathbf{f}_{ij}(t)$, where the sum is over all the other particles $i \neq j$ in contact. An useful relation that we will use is Newton's third law, $\mathbf{f}_{ij}(t) = -\mathbf{f}_{ji}(t)$.

We will denote as \mathbf{r} a point in space where we want to measure a given quantity such as the stress tensor. We will use Greek indices to denote the components of a vector or tensor and Latin indices to label the particles' entities. Einstein summation convention is used for the Greek indices; and the explicit time dependency (t) might be dropped sometimes for convenience of notation, just keep in mind which quantities are time dependent.

3.1.1 Mass Balance

For a system where the mass or number density is conserved, the easiest equation of motion to derive is the mass balance or continuity equation. In statistical mechanics, we define the microscopic mass density at a point \mathbf{r} and time t as

$$\rho^{mic}(\mathbf{r}, t) \equiv \sum_i m_i \delta(\mathbf{r} - \mathbf{r}_i(t)), \quad (3.1)$$

where $\delta(\mathbf{r} - \mathbf{r}_i(t))$ is the Dirac delta distribution. As you might know, this quantity is singular, given that it is defined for *point particles*. In coarse graining, we change the delta distribution for a non-singular coarse graining function ψ with a finite width w , which sets the graining scale or resolution, then the mass density becomes

$$\rho(\mathbf{r}, t) = \sum_i m_i \psi(\mathbf{r} - \mathbf{r}_i(t)). \quad (3.2)$$

The coarse graining function must be positive definite and normalizable, so that the integral of the density over all the space of the packing provides the total mass. There are many functions that fulfil these requirements, but some of the most common ones are:

$$\psi(\mathbf{r}) = \frac{1}{\Omega(w)} H(w - |\mathbf{r}|), \quad (3.3)$$

where H is the Heaviside function and $\Omega(w)$ the volume of a sphere with radius w in d -dimensions, naturally for 3D this means $\Omega(w) = \frac{4}{3}\pi w^3$. One can also use a Gaussian function for smoother fields and differentiability.

$$\psi(\mathbf{r}) = \frac{1}{(\sqrt{2\pi}w)^3} e^{-|\mathbf{r}|^2/(2w)^2} H(3w - |\mathbf{r}|). \quad (3.4)$$

Since the Gaussian function has infinite domain, we set a cut-off length $3w$ provided by the Heaviside function $H(3w - |\mathbf{r}|)$ in (3.4). But one of the most convenient choices is to use a Lucy polynomial, where the 4th-order one is given by

$$\psi(\mathbf{r}) = \frac{105}{16\pi c^3} \left[-3 \left(\frac{a}{c}\right)^4 + 8 \left(\frac{a}{c}\right)^3 - 6 \left(\frac{a}{c}\right)^2 + 1 \right], \quad (3.5)$$

with $a = \frac{|\mathbf{r}|}{c}$ and the coarse graining width $w = \frac{c}{2}$. These have the advantage to be integrable and differentiable analytically, and fast to compute numerically. The choice depends mostly in the velocity of computation and smoothness of the field desired.

One can also think of the coarse graining procedure as a convolution of the microscopic density with the coarse graining function

$$\rho(\mathbf{r}, t) = \int d\mathbf{r}' \psi(\mathbf{r} - \mathbf{r}') \rho^{mic}(\mathbf{r}', t). \quad (3.6)$$

To show that the coarse grained definition of the density automatically satisfies the mass balance, we will make use of the relation

$$\frac{\partial}{\partial t} \psi(\mathbf{r} - \mathbf{r}_i(t)) = -\dot{r}_{i\beta}(t) \frac{\partial}{\partial r_\beta} \psi(\mathbf{r} - \mathbf{r}_i(t)) = -v_{i\beta}(t) \frac{\partial}{\partial r_\beta} \psi(\mathbf{r} - \mathbf{r}_i(t)), \quad (3.7)$$

then, we just need to take the derivative of equation (3.2) with respect to time

$$\begin{aligned} \frac{\partial \rho(\mathbf{r}, t)}{\partial t} &= \frac{\partial}{\partial t} \sum_i m_i \psi(\mathbf{r} - \mathbf{r}_i) \\ &= -\frac{\partial}{\partial r_\beta} \sum_i m_i v_{i\beta} \psi(\mathbf{r} - \mathbf{r}_i) \\ &= -\frac{\partial p_\beta(\mathbf{r}, t)}{\partial r_\beta}, \end{aligned} \quad (3.8)$$

where we have defined the coarse grained momentum density

$$\mathbf{p}(\mathbf{r}, t) = \sum_i m_i \mathbf{v}_i \psi(\mathbf{r} - \mathbf{r}_i), \quad (3.9)$$

that corresponds, in comparison, to the microscopic momentum density field $\mathbf{p}^{mic}(\mathbf{r}, t) = \sum_i m_i \mathbf{v}_i \delta(\mathbf{r} - \mathbf{r}_i)$. If we also define the coarse grained velocity field as

$$\mathbf{V}(\mathbf{r}, t) = \frac{\mathbf{p}(\mathbf{r}, t)}{\rho(\mathbf{r}, t)}, \quad (3.10)$$

and insert it into equation (3.8), we arrive automatically to the continuity equation

$$\dot{\rho} = -\frac{\partial}{\partial r_\beta}(\rho V_\beta). \quad (3.11)$$

The coarse grained mass and momentum density fields are well defined physical entities, since they stem from particles' parameters; however, the velocity $\mathbf{V}(\mathbf{r}, t)$ only makes sense as a coarse grained field, since it is constructed from other coarse grained fields.

3.1.2 Momentum Balance

Since we have already defined the momentum density in equation (3.9), we can now derive the momentum balance equation. This is a longer procedure than for the mass balance, but we start by taking the derivative with respect to time of the momentum density

$$\begin{aligned} \frac{\partial p_\alpha(\mathbf{r}, t)}{\partial t} &= \frac{\partial}{\partial t} \sum_i m_i v_{i\alpha} \psi(\mathbf{r} - \mathbf{r}_i) \\ &= \sum_i m_i \dot{v}_{i\alpha} \psi(\mathbf{r} - \mathbf{r}_i) + \sum_i m_i v_{i\alpha} \frac{\partial \psi(\mathbf{r} - \mathbf{r}_i)}{\partial t} \\ &= \sum_i m_i \dot{v}_{i\alpha} \psi(\mathbf{r} - \mathbf{r}_i) - \frac{\partial}{\partial r_\beta} \sum_i m_i v_{i\alpha} v_{i\beta} \psi(\mathbf{r} - \mathbf{r}_i). \end{aligned} \quad (3.12)$$

We rename the two terms in the right-hand-side of equation (3.12); the first one we will call A_α and the second one B_α . We start by simplifying the first term

$$A_\alpha = \sum_i m_i \dot{v}_{i\alpha} \psi(\mathbf{r} - \mathbf{r}_i), \quad (3.13)$$

when using Newton's second law $m_i \dot{v}_{i\alpha} = f_{i\alpha}$ for the particle i and the total contact force felt by it $\mathbf{f}_i(t) = \sum_j \mathbf{f}_{ij}(t)$, we can recast A_α as

$$\begin{aligned} A_\alpha &= \sum_i f_{i\alpha} \psi(\mathbf{r} - \mathbf{r}_i) \\ &= \sum_{ij} f_{ij\alpha} \psi(\mathbf{r} - \mathbf{r}_i), \end{aligned} \quad (3.14)$$

i and j are just dummy indices, so by exchanging them in equation (3.14)

$$A_\alpha = \sum_{ij} f_{ji\alpha} \psi(\mathbf{r} - \mathbf{r}_j), \quad (3.15)$$

and using Newton's third law $f_{ij\alpha} = -f_{ji\alpha}$

$$A_\alpha = - \sum_{ij} f_{ij\alpha} \psi(\mathbf{r} - \mathbf{r}_j). \quad (3.16)$$

Equations (3.14) and (3.16) represent the same entity A_α , then, it is possible to rewrite A_α as the sum of the half of each

$$A_\alpha = \frac{1}{2} \sum_{ij} f_{ij\alpha} [\psi(\mathbf{r} - \mathbf{r}_i) - \psi(\mathbf{r} - \mathbf{r}_j)]. \quad (3.17)$$

A helpful identity that holds for any smooth function ψ is

$$\begin{aligned} \psi(\mathbf{r} - \mathbf{r}_j) - \psi(\mathbf{r} - \mathbf{r}_i) &= \int_0^1 ds \frac{\partial}{\partial s} \psi(\mathbf{r} - \mathbf{r}_i + s\mathbf{r}_{ij}) \\ &= \int_0^1 ds r_{ij\beta} \frac{\partial}{\partial r_\beta} \psi(\mathbf{r} - \mathbf{r}_i + s\mathbf{r}_{ij}) \\ &= r_{ij\beta} \frac{\partial}{\partial r_\beta} \int_0^1 ds \psi(\mathbf{r} - \mathbf{r}_i + s\mathbf{r}_{ij}). \end{aligned} \quad (3.18)$$

So by inserting equation (3.18) into (3.17) we obtain

$$A_\alpha = -\frac{1}{2} \frac{\partial}{\partial r_\beta} \sum_{ij} f_{ij\alpha} r_{ij\beta} \int_0^1 ds \psi(\mathbf{r} - \mathbf{r}_i + s\mathbf{r}_{ij}). \quad (3.19)$$

Since the derivative $\frac{\partial}{\partial r_\beta}$ commutes with all variables that describe the particles' degrees of freedom, it can be taken out of the summation.

Before simplifying the second term

$$B_\alpha = -\frac{\partial}{\partial r_\beta} \sum_i m_i v_{i\alpha} v_{i\beta} \psi(\mathbf{r} - \mathbf{r}_i), \quad (3.20)$$

it is convenient to define the fluctuation velocity of a particle i at time t

$$\mathbf{v}'_i(\mathbf{r}, t) = \mathbf{v}_i(t) - \mathbf{V}(\mathbf{r}, t). \quad (3.21)$$

However, notice that \mathbf{v}'_i is defined with respect to the coarse grained velocity $\mathbf{V}(\mathbf{r}, t)$ at the coarse graining center \mathbf{r} and not the particle's position \mathbf{r}_i . There are other ways to define fluctuations that might not give consistent results with the equations of continuum mechanics. In kinetic theory, for example, one defines the velocity fluctuations with respect to the local value of the velocity field [20, 24], but a discussion of this issue is beyond the scope of this thesis.

From the relation (3.21) it follows

$$\begin{aligned}
\sum_i m_i \mathbf{v}'_i \psi(\mathbf{r} - \mathbf{r}_i) &\equiv \sum_i m_i [\mathbf{v}_i - \mathbf{V}] \psi(\mathbf{r} - \mathbf{r}_i) \\
&= \sum_i m_i \mathbf{v}_i \psi(\mathbf{r} - \mathbf{r}_i) - \mathbf{V} \sum_i m_i \psi(\mathbf{r} - \mathbf{r}_i) \\
&= \mathbf{p} - \rho \mathbf{V} = 0,
\end{aligned} \tag{3.22}$$

from the definition of \mathbf{V} ; which also implies

$$\sum_i m_i V_\alpha v'_{i\beta} \psi = V_\alpha \sum_i m_i v'_{i\beta} \psi = 0. \tag{3.23}$$

Then, using equations (3.21) and (3.23) to simplify B_α , one obtains

$$\begin{aligned}
B_\alpha &= -\frac{\partial}{\partial r_\beta} \sum_i m_i v_{i\alpha} v_{i\beta} \psi(\mathbf{r} - \mathbf{r}_i) \\
&= -\frac{\partial}{\partial r_\beta} \sum_i m_i (V_\alpha + v'_{i\alpha}) (V_\beta + v'_{i\beta}) \psi(\mathbf{r} - \mathbf{r}_i) \\
&= -\frac{\partial}{\partial r_\beta} \left[\sum_i m_i V_\alpha V_\beta \psi(\mathbf{r} - \mathbf{r}_i) + \sum_i m_i v'_{i\alpha} v'_{i\beta} \psi(\mathbf{r} - \mathbf{r}_i) \right] \\
&= -\frac{\partial}{\partial r_\beta} \left[\rho V_\alpha V_\beta + \sum_i m_i v'_{i\alpha} v'_{i\beta} \psi(\mathbf{r} - \mathbf{r}_i) \right].
\end{aligned} \tag{3.24}$$

Finally, inserting A_α from (3.19) and B_α from (3.24) into (3.12), we arrive at the momentum balance equation

$$\frac{\partial p_\alpha}{\partial t} = -\frac{\partial}{\partial r_\beta} [\rho V_\alpha V_\beta - \sigma_{\alpha\beta}], \tag{3.25}$$

having defined the stress tensor σ as

$$\sigma_{\alpha\beta} = -\frac{1}{2} \sum_{ij} f_{ij\alpha} r_{ij\beta} \int_0^1 ds \psi(\mathbf{r} - \mathbf{r}_i + s \mathbf{r}_{ij}) - \sum_i m_i v'_{i\alpha} v'_{i\beta} \psi(\mathbf{r} - \mathbf{r}_i). \tag{3.26}$$

The first term of the stress tensor corresponds to the bulk contact stress

$$\sigma_{\alpha\beta}^c = -\frac{1}{2} \sum_{ij} f_{ij\alpha} r_{ij\beta} \int_0^1 ds \psi(\mathbf{r} - \mathbf{r}_i + s \mathbf{r}_{ij}), \tag{3.27}$$

the second term is the kinetic stress, negligible for quasi-static deformations

$$\sigma_{\alpha\beta}^k = -\sum_i m_i v'_{i\alpha} v'_{i\beta} \psi(\mathbf{r} - \mathbf{r}_i). \tag{3.28}$$

Goldhirsch [20] makes a deep physical interpretation of the stress tensor and also derives the equation for the angular momentum density field, which is out of the scope of this thesis.

3.2 Coarse Graining Near Boundaries

Weinhart et al. [21] made an extension of Goldhirsch's work [20] adding the interaction due to boundaries, by treating the walls as K static particles as if they had infinite mass. Taking this into consideration, the total force that a particle i feels becomes

$$f_{i\alpha} = \sum_j f_{ij\alpha} + \sum_k f_{ik\alpha}, \quad (3.29)$$

where k runs over all the *wall particles* in contact with i . Naturally, if a particle is not in contact with any of the *wall particles*, the force $f_{ik\alpha}$ disappears. The mass balance equation remains the same as in equation (3.11) but the momentum balance equation takes the form

$$\frac{\partial p_\alpha}{\partial t} = -\frac{\partial}{\partial r_\beta} [\rho V_\alpha V_\beta - \sigma_{\alpha\beta}] + t_\alpha, \quad (3.30)$$

where the boundary interaction force density t_α has been included

$$t_\alpha = \sum_{ik} f_{ik\alpha} \psi(\mathbf{r} - \mathbf{c}_{ik}), \quad (3.31)$$

here, $c_{ik\alpha}$ is the vector directed to the contact point between i and the *wall particles*. The stress tensor components $\sigma_{\alpha\beta}$ also receive another contribution due to wall interactions given by

$$\sigma_{\alpha\beta}^w = -\sum_{ik} f_{ik\alpha} b_{ik\beta} \int_0^1 ds \psi(\mathbf{r} - \mathbf{r}_i + s\mathbf{b}_{ik}), \quad (3.32)$$

being $b_{ik\alpha} = r_{i\alpha} - c_{ik\alpha}$ the branch vector. In a contact between two *normal particles* one defines the relative position as \mathbf{r}_{ij} ; but near a boundary we use instead the branch vector, since the *wall particles* have no defined radius.

3.3 Coarse Graining of Body Forces

Until now, we have not included body forces, such as gravity; this can be done easily when adding the body force \mathbf{F} to the total force felt by a particle i

$$f_{i\alpha} = \sum_j f_{ij\alpha} + F_{i\alpha}, \quad (3.33)$$

Weinhart et al. [21] and Tunuguntla et al. [23] use the letter \mathbf{b} to denote body forces, but we reserved this label to the branch vector so we rename it as \mathbf{F} . The body force density is defined as

$$F_\alpha = \sum_i F_{i\alpha} \psi(\mathbf{r} - \mathbf{r}_i), \quad (3.34)$$

then, the total body force is computed when we sum over all the particles i

$$F_\alpha = \sum_i F_{i\alpha} \quad (3.35)$$

and appears as an extra source term in the momentum balance equation

$$\frac{\partial p_\alpha}{\partial t} = -\frac{\partial}{\partial r_\beta} [\rho V_\alpha V_\beta - \sigma_{\alpha\beta}] + t_\alpha + F_\alpha. \quad (3.36)$$

3.4 Coarse Graining of an Isotropic Compression

As an example to review the concepts and equations developed in this chapter, we will consider the case of an isotropic compression of a polydisperse disks packing in 2D, where the strain rate tensor is given by

$$\dot{E} = \dot{e} \begin{pmatrix} -1 & 0 \\ 0 & -1 \end{pmatrix},$$

being \dot{e} the rate amplitude. The simulation was done using MercuryDPM, where we placed in a square box, with periodic boundary conditions, 1000 non-overlapping disks with radii a varying between 0.013 and 0.032 m with an initial low packing fraction. The box is then compressed until a packing fraction of $\phi \approx 0.85$ is achieved, situation that is depicted in Figure 3.1; the lines represent the normal contact forces connecting the center of each particle to the contact point, being the width of the line proportional to the magnitude of the force.

Using the built-in statistics package of MercuryDPM we can compute: the coarse grained density in 2D

$$\Sigma = \frac{3\rho}{4a},$$

where ρ is the coarse grained density in 3D defined in equation (3.2); volume fraction

$$\phi = \rho / \rho_p,$$

with the particle density ρ^p ; the momentum density (equation (3.9)) and the stress tensor (equation (3.26)) at the maximum compression point. In Figure 3.2 we show these fields (only the xy component of the contact and kinetic stress) using a $w = 0.05$ m with no time averaging. Before discussing the dependency of the fields on w we will analyse what the contour maps in Figure 3.2 can tell us about the system.

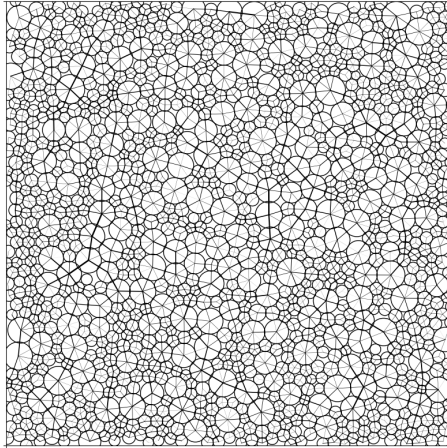


FIGURE 3.1: Isotropically compressed square box with 1000 polydisperse disks, the lines connecting each particle represent the normal contact forces.

The density of the particles themselves is $\rho_p = 2500 \text{ kg/m}^2$, therefore it is reasonable that the coarse grained density of a closely packed system is comparable in magnitude to the particle density, being less or equal for incompressible (but elastic) materials. We see some red and blue spots corresponding to highly and less packed regions respectively; the packing fraction follows the same pattern, since it is derived from the density. We see that, even though the global packing fraction is ≈ 0.85 , there are spots where locally ϕ is higher or smaller than the global value. In general, there is no visible structure in the density of packing fraction rather than the low values at the borders because of periodic boundary effects.

The x and y components of the momentum density display some interesting features. After the compression, the particles acquire a small velocity that would have been suppressed if the walls were infinite, however, due to the periodicity of the boundaries, the particles are free to go out and in of the box creating a flow visible from the components of the momentum density.

We chose the xy component of the stress as representative for this example. The total stress is given in this case by the sum of the contact and kinetic terms, which are shown in Figure 3.2. From the color bars, it is clear that the main component of the stress is the contact one, as it is expected from the high compression; the kinetic stress might become important in situations where we have a steady flow and higher velocities.

According to Weinhart et al. [23, 24, 25], the coarse grained fields depend weakly on the coarse graining function, but they depend highly on the width w ; each well defined macroscopic field should produce a range of values for w where the field does not depend on the coarse graining width. In Figure 3.3 we show the contour plots of the packing fraction for different choices of w , if we choose the width smaller than the particle size, say $w = 0.001 \text{ m}$, we might resolve details on the particle scale, but meaningless for a macroscopic description of the field. A width of 0.03 m

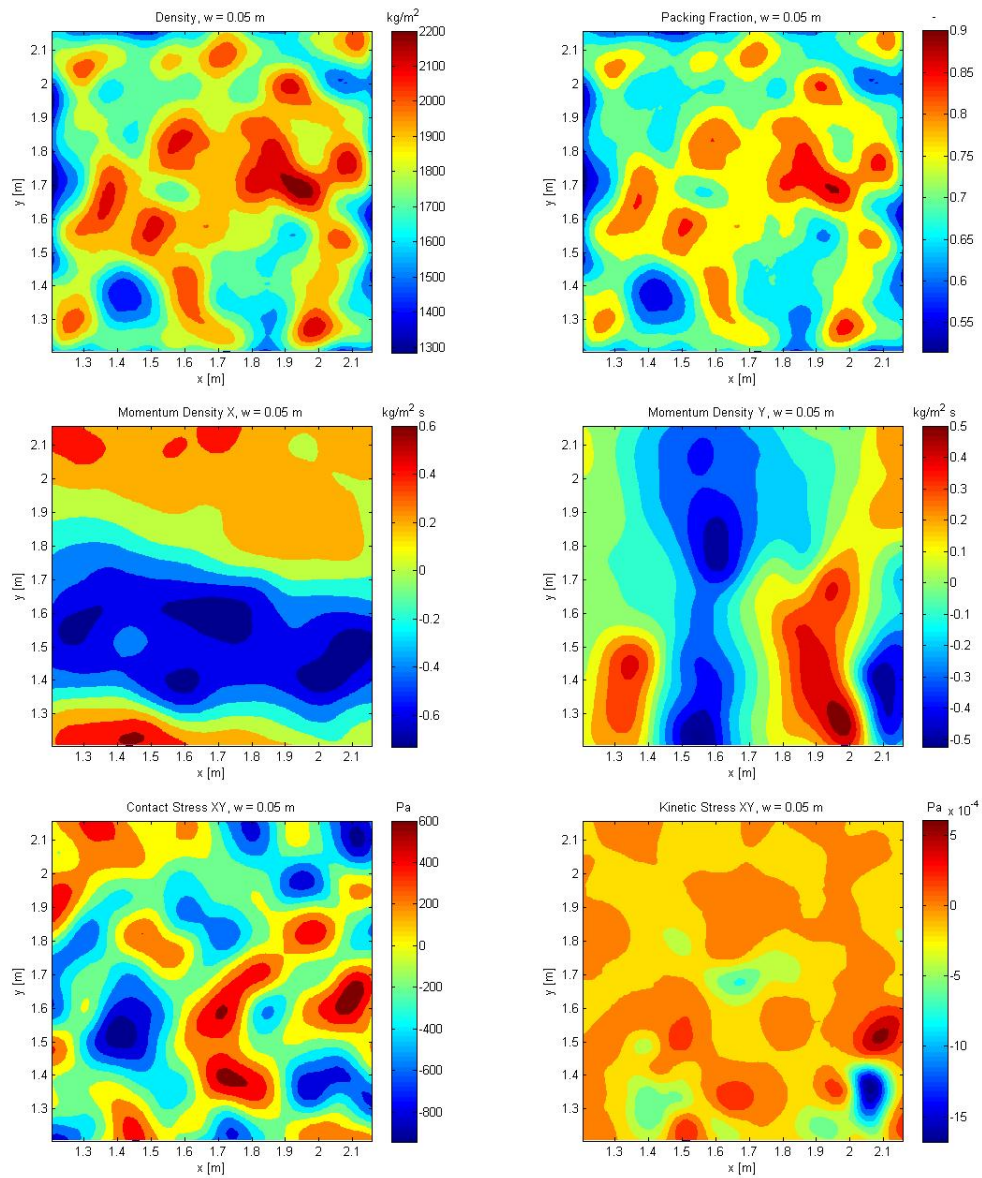


FIGURE 3.2: Coarse grained density, packing fraction, momentum density and the xy component of the contact and kinetic stress tensor of the disks packing shown in Figure 3.1.

still produces a highly fluctuating field as seen in Figure 3.3, but probably useful if we want to study the structure of the force chains at this scale. The election of $w = 0.05$ m was made to compute the fields shown in Figure 3.2; and it was found by try and error that a value around it (± 0.005 m) will give similar results. Finally, a $w = 0.1$ m yields to a very smoothed out field with the periodic boundary condition effect enhanced by the big scale.

3.5 Summary

We developed the basic theory of coarse graining to obtain continuum equations from discrete particle data. We introduced and gave examples of coarse graining functions ψ , in order to define the coarse grained mass density

$$\rho(\mathbf{r}, t) = \sum_i m_i \psi(\mathbf{r} - \mathbf{r}_i(t)), \quad (3.37)$$

the coarse grained momentum density

$$\mathbf{p}(\mathbf{r}, t) = \sum_i m_i \mathbf{v}_i \psi(\mathbf{r} - \mathbf{r}_i(t)) \quad (3.38)$$

and the coarse grained velocity field

$$\mathbf{V}(\mathbf{r}, t) = \frac{\mathbf{p}(\mathbf{r}, t)}{\rho(\mathbf{r}, t)}. \quad (3.39)$$

We showed that these relations automatically satisfy the mass and momentum balance equations, since they are derived from these definitions themselves. We also made a quick review of extensions for coarse graining near boundaries and body forces.

It is important to remark that these results are independent of the contact model between the particles. As long as the conditions described at the beginning of the chapter hold, the theory will apply if we use a linear contact model, like the one described in Chapter II, or a Hertzian model, etc. [18].

Finally, we showed through an example the application of the coarse grained equations, the way to analyse the results and the high dependence of these on the coarse graining width w .

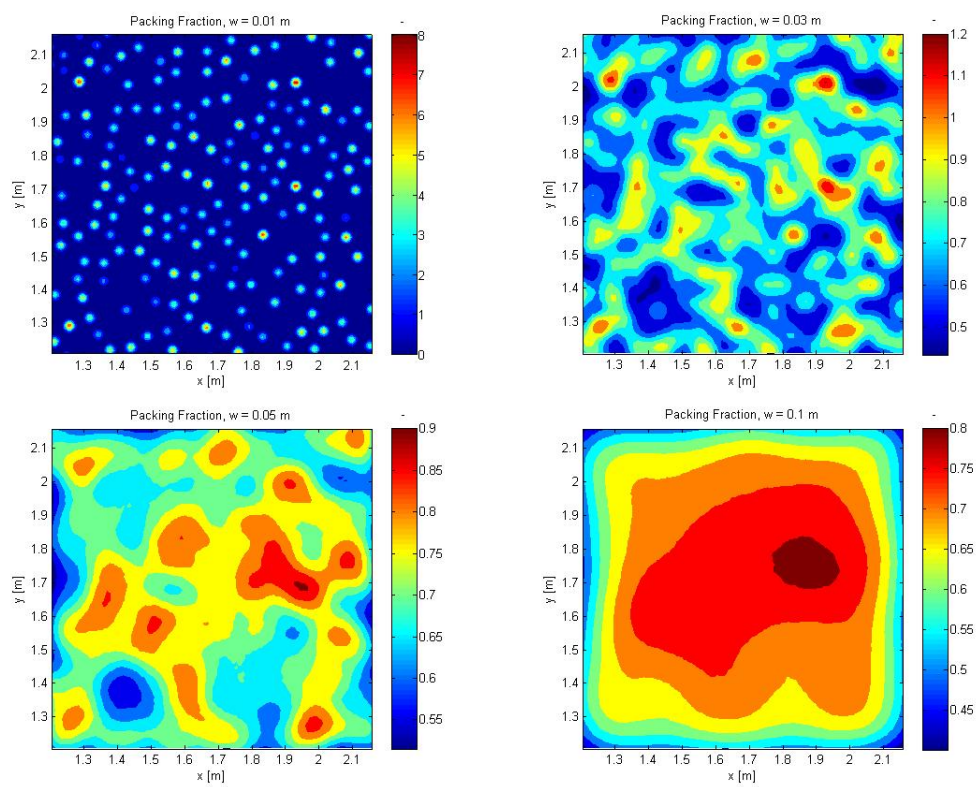


FIGURE 3.3: Coarse grained packing fraction using widths of $w = 0.001, 0.03, 0.05$ and 0.1 m.

Chapter 4

Gravitational Dynamics

In this chapter we are going to develop the basic theory of gravitation and the Two Body Problem, we will derive the radial equation of motion and apply it for the case of circular orbits; then, we will obtain the angular velocity of an object in circular orbit, called the Kepler Frequency. Finally, we will pose the N-body problem and show an example of an N-body simulation made with AMUSE.

There are many good books that address the Two Body Problem; from undergraduate level, such as *Classical Dynamics of Particles and Systems* of Marion [26] and *Classical Mechanics* of Taylor [27], to more advanced books for graduate students like *Classical Mechanics* of Goldstein [28]. This chapter and the next one have the mathematical and physical basis for the astrophysical part of the simulations presented later on. In particular, section 4.1.1 follows closely the derivation made by Taylor [27] (with some modifications) of the radial equation, which ultimately will lead us to the orbital frequency.

4.1 The Two Body Problem

4.1.1 Conservative Central Force Problem

We will consider the motion of two punctual bodies that exert a conservative central force on each other. The positions of the bodies with respect to an inertial reference frame are \mathbf{r}_1 and \mathbf{r}_2 with masses m_1 and m_2 respectively. The relative position of the bodies is just the difference of the position vectors

$$\mathbf{r} = \mathbf{r}_1 - \mathbf{r}_2, \quad (4.1)$$

the situation is depicted in Figure 4.1.

Since the forces that the bodies exert are conservative, they can be derived from a potential which we call U , this potential is dependent on the positions of the two particles, $U(\mathbf{r}_1, \mathbf{r}_2)$. Moreover, if the force is central, the potential depends on the magnitude of the relative position $r = |\mathbf{r}_1 - \mathbf{r}_2|$, so we can use the notation $U(r)$ for a conservative central potential.

Naturally, we are interested in the gravitational potential

$$U(\mathbf{r}_1, \mathbf{r}_2) = -\frac{Gm_1m_2}{|\mathbf{r}_1 - \mathbf{r}_2|}, \quad (4.2)$$

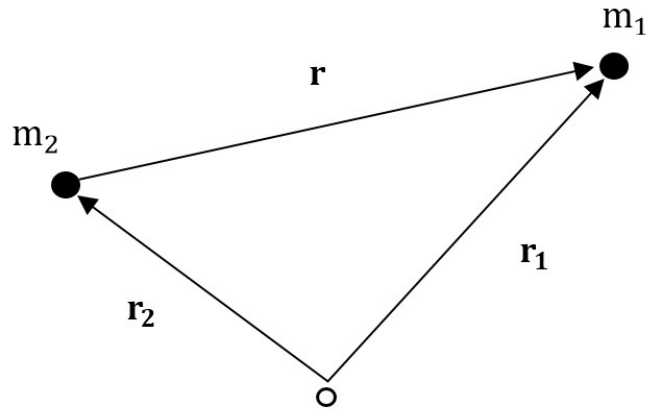


FIGURE 4.1: The particles with masses m_1 and m_2 have a position vector of \mathbf{r}_1 and \mathbf{r}_2 respectively. The relative position vector $\mathbf{r} = \mathbf{r}_1 - \mathbf{r}_2$ connects both masses.

but, for the time being, we will continue using $U(r)$ for shorter notation, since the theory we will develop applies for any conservative central potential.

We can write the Lagrangian \mathcal{L} of the system, which is just the total kinetic energy K minus the potential energy U : $\mathcal{L} = K - U$. In the current case this is

$$\mathcal{L} = \frac{1}{2}m_1\dot{\mathbf{r}}_1^2 + \frac{1}{2}m_2\dot{\mathbf{r}}_2^2 - U(r), \quad (4.3)$$

where the dots represent the derivative with respect to time. We will see later on that it is convenient to use the relative position \mathbf{r} and the position of the center of mass \mathbf{R} as generalized coordinates to describe the problem, where

$$\mathbf{R} = \frac{m_1\mathbf{r}_1 + m_2\mathbf{r}_2}{m_1 + m_2} = \frac{m_1\mathbf{r}_1 + m_2\mathbf{r}_2}{M}, \quad (4.4)$$

and $M = m_1 + m_2$.

In a two body problem, the position of the center of mass lies on the line that connects particle 1 with particle 2, as seen in Figure 4.2. If we use this point as a new origin for the reference frame the equations of motion will become simpler.

Now our task is to transform the Lagrangian in (4.3) to a Lagrangian with our choice of generalized coordinates, $\mathcal{L}(\mathbf{r}, \mathbf{R})$. Using equations (4.1) and (4.4) we obtain

$$\begin{aligned} \mathbf{r}_1 &= \mathbf{R} + \frac{m_2}{M}\mathbf{r}, \\ \mathbf{r}_2 &= \mathbf{R} - \frac{m_1}{M}\mathbf{r}. \end{aligned} \quad (4.5)$$

Inserting equations (4.5) into the total kinetic energy we can rewrite K in terms of the new variables:

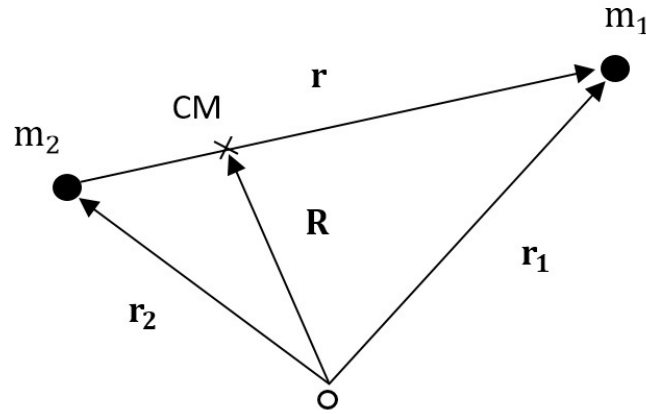


FIGURE 4.2: The position vector of the center of mass is defined as $\mathbf{R} = \frac{m_1\mathbf{r}_1 + m_2\mathbf{r}_2}{m_1 + m_2}$ and lies at the line that connects both masses.

$$\begin{aligned}
 K &= \frac{1}{2} (m_1 \dot{\mathbf{r}}_1^2 + m_2 \dot{\mathbf{r}}_2^2) \\
 &= \frac{1}{2} \left(m_1 \left[\dot{\mathbf{R}} + \frac{m_2}{M} \dot{\mathbf{r}} \right]^2 + m_2 \left[\dot{\mathbf{R}} - \frac{m_1}{M} \dot{\mathbf{r}} \right]^2 \right) \\
 &= \frac{1}{2} \left(M \dot{\mathbf{R}}^2 + \frac{m_1 m_2}{M} \dot{\mathbf{r}}^2 \right), \tag{4.6}
 \end{aligned}$$

if we define the reduced mass μ as

$$\mu = \frac{m_1 m_2}{m_1 + m_2} = \frac{m_1 m_2}{M}, \tag{4.7}$$

we obtain

$$K = \frac{1}{2} M \dot{\mathbf{R}}^2 + \frac{1}{2} \mu \dot{\mathbf{r}}^2. \tag{4.8}$$

You may notice that we need not to rewrite the potential energy $U(r)$, since it is already dependent only on the relative position, one of the new variables. Now we can write the Lagrangian in these coordinates.

$$\begin{aligned}
 \mathcal{L} &= K - U \\
 &= \frac{1}{2} M \dot{\mathbf{R}}^2 + \left(\frac{1}{2} \mu \dot{\mathbf{r}}^2 - U(r) \right) \\
 &= \mathcal{L}_{cm} + \mathcal{L}_{rel}. \tag{4.9}
 \end{aligned}$$

We have divided \mathcal{L} into one term dependent only on the motion of the center of mass \mathcal{L}_{cm} and other term dependent on the relative motion \mathcal{L}_{rel} . To obtain the equations

of motion we make use of the Euler-Lagrange equations

$$\frac{\partial \mathcal{L}}{\partial q} - \frac{d}{dt} \left(\frac{\partial \mathcal{L}}{\partial \dot{q}} \right) = 0. \quad (4.10)$$

If we take formally $\frac{\partial}{\partial \mathbf{q}} = \nabla_q$, for \mathbf{R}

$$\frac{\partial \mathcal{L}}{\partial \mathbf{R}} - \frac{d}{dt} \left(\frac{\partial \mathcal{L}}{\partial \dot{\mathbf{R}}} \right) = 0, \quad (4.11)$$

the equation of motion for the center of mass becomes

$$M\ddot{\mathbf{R}} = 0, \quad (4.12)$$

which integrating once with respect to time means

$$\dot{\mathbf{R}} = \text{constant}. \quad (4.13)$$

Similarly the equation of motion for \mathbf{r} is obtained computing

$$\frac{\partial \mathcal{L}}{\partial \mathbf{r}} - \frac{d}{dt} \left(\frac{\partial \mathcal{L}}{\partial \dot{\mathbf{r}}} \right) = 0, \quad (4.14)$$

which after the derivatives becomes:

$$\mu \ddot{\mathbf{r}} = -\nabla U(r). \quad (4.15)$$

Note that in this case the gradient is done with respect to the relative position coordinates.

4.1.2 Motion in the Center of Mass Reference Frame

We notice from equation (4.13) that, since the position of the center of mass moves with a constant velocity, it is also an inertial reference frame. It is clever to take the center of mass origin for our new coordinate system as $\mathbf{R} = 0$, since in here $\dot{\mathbf{R}} = 0$ and

$$\begin{aligned} \mathbf{r}_1 &= \frac{m_2}{M} \mathbf{r}, \\ \mathbf{r}_2 &= -\frac{m_1}{M} \mathbf{r}. \end{aligned} \quad (4.16)$$

as depicted in Figure 4.3.

It is important to take a moment to analyse equations (4.16). If one of the masses, say m_2 , is much bigger than the other one, $m_2 \gg m_1$, then $r_1 \gg r_2$ and the position of the center of mass would be very close to the particle two. Equivalently, the size of \mathbf{r}_1

would be comparable to \mathbf{r} , meaning $\mathbf{r}_1 \approx \mathbf{r}$ and $\mathbf{r}_2 \approx \mathbf{0}$. Such situations can be easily found, for example the system Sun-Earth where the mass of the Sun is much bigger than the one of the Earth, or, the case that concerns us, the Saturn's rings system, where the mass of Saturn is much bigger than the mass of one ring particle, or a moonlet for that matter.

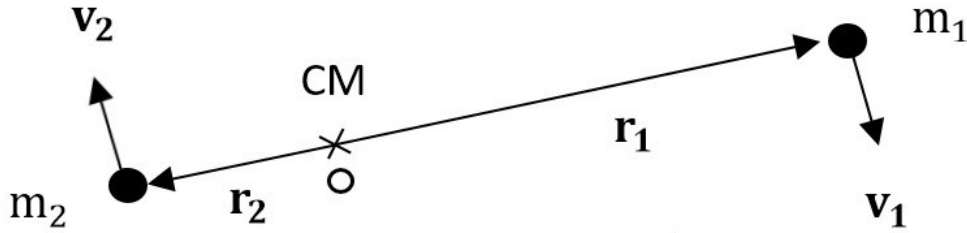


FIGURE 4.3: The center of mass moves with a constant velocity, therefore, it can be taken as an inertial reference frame. Both particles move with respect to this frame with velocities \mathbf{v}_1 and \mathbf{v}_2 at positions \mathbf{r}_1 and \mathbf{r}_2 respectively.

In the center of mass reference frame, the Lagrangian (4.9) simplifies to only the Lagrangian of the relative motion

$$\mathcal{L} = \mathcal{L}_{rel} = \frac{1}{2}\mu\dot{\mathbf{r}}^2 - U(r). \quad (4.17)$$

We have reduced the problem to one that resembles the motion of a particle with mass μ at position \mathbf{r} from the origin. The motion of this *virtual* (in the sense that it is not real) particle lies within a plane, since the two body problem can always be reduced to a two dimensional problem. Say we choose the plane xy , then, polar coordinates are the fittest to describe it. If we write the velocity $\dot{\mathbf{r}}$ in equation (4.17) in polar coordinates we obtain

$$\mathcal{L} = \frac{1}{2}\mu \left(\dot{r}^2 + r^2\dot{\phi}^2 \right) - U(r), \quad (4.18)$$

where r is the radial distance from the origin to this *virtual* particle and ϕ the azimuthal angle.

With the help of the Euler-Lagrange equation it is easy to write the equations of motion. For ϕ this reads

$$\frac{\partial \mathcal{L}}{\partial \phi} - \frac{d}{dt} \left(\frac{\partial \mathcal{L}}{\partial \dot{\phi}} \right) = 0, \quad (4.19)$$

and we obtain the *polar equation*

$$\frac{\partial \mathcal{L}}{\partial \dot{\phi}} = \mu r^2 \dot{\phi} = \text{constant} = l. \quad (4.20)$$

Given that ϕ does not appear explicitly in the Lagrangian (4.18), it is said to be an ignorable coordinate, which implies that there is a conserved quantity, in this case the z component of the angular momentum, l .

Similarly, to obtain the *radial equation* we compute

$$\frac{\partial \mathcal{L}}{\partial r} - \frac{d}{dt} \left(\frac{\partial \mathcal{L}}{\partial \dot{r}} \right) = 0, \quad (4.21)$$

giving us

$$\mu \ddot{r} = \mu r \dot{\phi}^2 - \frac{dU}{dr}. \quad (4.22)$$

Equation (4.22) is a coupled second order differential equation for the variables r and ϕ . Thankfully, we can solve for $\dot{\phi}$ in equation (4.20)

$$\dot{\phi} = \frac{l}{\mu r^2}, \quad (4.23)$$

and insert it into (4.22)

$$\mu \ddot{r} = -\frac{dU}{dr} + \frac{l^2}{\mu r^3}. \quad (4.24)$$

The last term corresponds to the centrifugal force $F_{cent} = \frac{l^2}{\mu r^3}$, which you might find more familiar written in terms of the azimuthal velocity $v_\phi = r\dot{\phi}$ as $F_{cent} = \frac{\mu v_\phi^2}{r}$.

Until now, we have written the radial equation in terms of the potential $U(r)$, but we can easily rewrite it in terms of the force $F(r)$ as

$$\mu \ddot{r} = F(r) + \frac{l^2}{\mu r^3}. \quad (4.25)$$

The reason we are doing this is because we are going to look into a particular kind of forces, the ones that have the form

$$F(r) = -\frac{k}{r^2} \quad (4.26)$$

in the case of the gravitational force $k = Gm_1m_2$. Equation (4.25) with this type of forces can be solved by applying the clever transformation:

$$u = \frac{1}{r}, \quad r = \frac{1}{u}. \quad (4.27)$$

With this transformation, the derivative with respect to time turns into

$$\frac{d}{dt} = \frac{d\phi}{dt} \frac{d}{d\phi} = \dot{\phi} \frac{d}{d\phi} = \frac{l}{\mu r^2} \frac{d}{d\phi} = \frac{lu^2}{\mu} \frac{d}{d\phi}, \quad (4.28)$$

so the radial velocity becomes

$$\dot{r} = \frac{d}{dt} r = \frac{lu^2}{\mu} \frac{d}{d\phi} \left(\frac{1}{u} \right) = -\frac{l}{\mu} \frac{du}{d\phi} \quad (4.29)$$

and the radial acceleration

$$\ddot{r} = \frac{d}{dt} \dot{r} = \frac{lu^2}{\mu} \frac{d}{d\phi} \left(-\frac{l}{\mu} \frac{du}{d\phi} \right) = -\frac{l^2 u^2}{\mu^2} \frac{d^2 u}{d\phi^2}. \quad (4.30)$$

Recasting equation (4.25) using equations (4.27), (4.29) and (4.30)

$$u''(\phi) = -u(\phi) - \frac{\mu}{l^2 u(\phi)^2} F(u), \quad (4.31)$$

and inserting now the force

$$F(r) = -\frac{k}{r^2} = -ku^2 \quad (4.32)$$

into (4.31) we arrive at

$$u''(\phi) = -u(\phi) + \frac{k\mu}{l^2}, \quad (4.33)$$

which has the general solution

$$u(\phi) = \frac{k\mu}{l^2} + A \cos(\phi + \delta), \quad (4.34)$$

A and δ are constants of integration; nevertheless, δ is just a phase that can be set to zero using a smart choice of the position $\phi = 0$. Then equation (4.34) can be rewritten as

$$u(\phi) = \frac{k\mu}{l^2} (1 + \epsilon \cos(\phi)), \quad (4.35)$$

where

$$\epsilon = \frac{Al^2}{k\mu}. \quad (4.36)$$

We can introduce the length given by $c = \frac{l^2}{k\mu}$, such that (4.35) transform into

$$\frac{1}{r(\phi)} = \frac{1}{c}(1 + \epsilon \cos(\phi))$$

and taking the inverse we finally arrive at the solution for the radial equation

$$r(\phi) = \frac{c}{(1 + \epsilon \cos(\phi))}. \quad (4.37)$$

We recognize (4.37) as the equation of a conic section, with ϵ called the eccentricity and $2c$ called the latus rectum of the orbit. When $\epsilon > 1$, (4.37) describes a hyperbola, if $\epsilon = 1$, it describes a parabola, when $1 < \epsilon < 0$, it is an ellipse and the special case when $\epsilon = 0$, it is the equation of a circle. Specifically, the case we are interested in are the orbits of moonlets and particles around Saturn, it is observed [2] that their eccentricities are nearly zero, i.e., their orbits are almost circular and r corresponds approximately to the radial distance from the center of Saturn to the rings and/or moonlets.

4.2 Kepler Frequency

After this long preamble, we can now find the angular velocity for circular orbits, also called Kepler Frequency, Ω . It will be an important parameter throughout the rest of this manuscript. To obtain an expression for it, we compute the angular momentum \mathbf{l} of a small mass, call it m_1 for continuity from our previous discussion, orbiting a much bigger mass m_2 in a circular motion of radius r , such that

$$\mathbf{l} = \mathbf{r} \times \mathbf{p} = \mathbf{r} \times m_1 \mathbf{v}_\phi = m_1 \mathbf{r} \times r \boldsymbol{\Omega}, \quad (4.38)$$

where \mathbf{p} is the linear momentum given by $\mathbf{p} = m_1 \mathbf{v} = m_1 \mathbf{v}_\phi = m_1 r \boldsymbol{\Omega}$, since for circular motion the only non-zero component of the velocity is the azimuthal one. We assume that the motion is planar and the Kepler Frequency $\boldsymbol{\Omega}$ is perpendicular to the position vector \mathbf{r} , so that the magnitude of l is

$$l = mr^2 \Omega. \quad (4.39)$$

Making use of equation (4.37) for the especial case when it describes a circle, $\epsilon = 0$ and inserting the constants

$$k = Gm_1 m_2$$

and

$$\mu = \frac{m_1 m_2}{m_1 + m_2},$$

we obtain

$$r = c = \frac{l^2}{k\mu} = \frac{m_1^2 r^4 \Omega^2}{G m_1 m_2 \mu}, \quad (4.40)$$

which can be solved for Ω

$$\Omega^2 = \frac{G}{r^3} \frac{m_2^2}{m_1 + m_2}. \quad (4.41)$$

Given that we assumed $m_2 \gg m_1$, we can approximate to

$$\Omega^2 \approx \frac{G m_2}{r^3}, \quad (4.42)$$

which leads us to the famous expression for the Kepler Frequency

$$\Omega \approx \sqrt{\frac{G m_2}{r^3}}. \quad (4.43)$$

4.3 N-body Problem

A self-gravitating system is an example of what is called an *N*-body problem. For a system of *N* particles, the gravitational acceleration \mathbf{a}_i for a particle *i* due to a group of massive objects *j* is

$$\mathbf{a}_i \equiv \ddot{\mathbf{r}}_i = G \sum_{j \neq i}^N m_j \frac{(\mathbf{r}_j - \mathbf{r}_i)}{|\mathbf{r}_j - \mathbf{r}_i|^3}. \quad (4.44)$$

Here *G* is the already mentioned gravitational constant, m_j and \mathbf{r}_j are the mass and position of particle *j* [16]. Equation (4.44) is a set of coupled, second-order, non-linear, singular ordinary differential equations with no known analytical solution. Posing the problem and evaluating (4.44) is not hard, nor integrating the equations of motion with an *N*-body solver, using the AMUSE framework for example.

However, there are limitations that we need to be aware of; first of all, we take the *N* particles as point masses, neglecting the spatial extent or shape of the gravitating bodies, with the center of mass being the geometrical center of the particle. Second, we assume that the relativistic effects are negligible, meaning that the velocity of the particles is much smaller than the velocity of light. Third, it is assumed that gravity acts instantaneously, where in a relativistic and more physically correct sense, the speed of gravitational waves is the same as the speed of light [16].

4.3.1 Very Close Titan System

To apply the ideas developed throughout the chapter, we will start by simulating a rather artificial and simplistic model of the Saturn system, but interesting to illustrate the effect of gravity on the rings.

Using the AMUSE framework, we place Saturn in the middle of the computation domain. Around it, we set 1000 spherical particles whose radii are of 2 m, situated in a circular ring that spans from 95,000 km to 120,000 km in the radial direction. The density of the particles is set to 500 kg/m^3 . We artificially place the biggest moon of Saturn, Titan, at 130,000 km from the planet, as seen in Figure 4.4 a). Notice that the figure is not in scale, the size of the particles in the ring was enhanced to be able to visualize them.

In reality, Titan is located at approximately 1,221,870 km away from Saturn [3]. But, even with its huge mass of $\approx 1.3 \times 10^{23} \text{ kg}$, there is no visible effect of Titan on the rings at short temporal scales. Nevertheless, when placing the moon so close to the ring particles, the effects are observed on a time scale of hours.

Before attempting to integrate equation (4.44) for the system, one must choose *realistic* initial conditions. For this, we will assume that not only the ring particles but also Titan undergo a circular motion, such that their orbital frequency is given by equation (4.43) with m_2 the mass of Saturn. Then, their orbital velocity is given by

$$v_\phi = r\Omega, \quad (4.45)$$

with r the radial distance of each object with respect to the center of Saturn. In the simulation, we set them all in a plane rotating clockwise as seen from above.

We chose to use a symplectic N-body integrator called Huayno (more about symplecticity and Huayno in the next subsection), which helps us to integrate numerically equation (4.44). We let the system evolve for 5 days or 432,000 s including self-gravity, i.e., each particle in the simulation feels the gravitational interaction of all the others. Snapshots of the system are shown in Figures 4.4 b), c) and d) at 108,000 s (≈ 2.2 Titan orbits), 216,000 s (≈ 4.5 Titan orbits) and 324,000 s (≈ 6.7 Titan orbits) respectively.

The effect of Titan is evident, attracting the closest ring particles and launching them around on its way as a slingshot. From this didactic experiment we recognize that if an object, comparable in size to Titan, catches Saturn's orbit, it will destroy the rings in a matter of days. If we considered Titan as just another *big* particle orbiting Saturn and we did not include self-gravity, the rings would have not been destroyed, showing the difference between a self and a non gravitating case. Naturally this is a very extreme example.

As an interesting fact, it is theorized that Saturn's rings are no older than 100 million years, and will last no longer than 100 million years, since the rings are being pulled into Saturn by gravity under the influence of the planet's magnetic field [29]. If this age estimate of the rings is correct, it will favour the theory that they were created from a moon that was able to form inside the Roche limit, but a later collision destroyed both bodies and the debris did not re-accrete into a new moon [2].

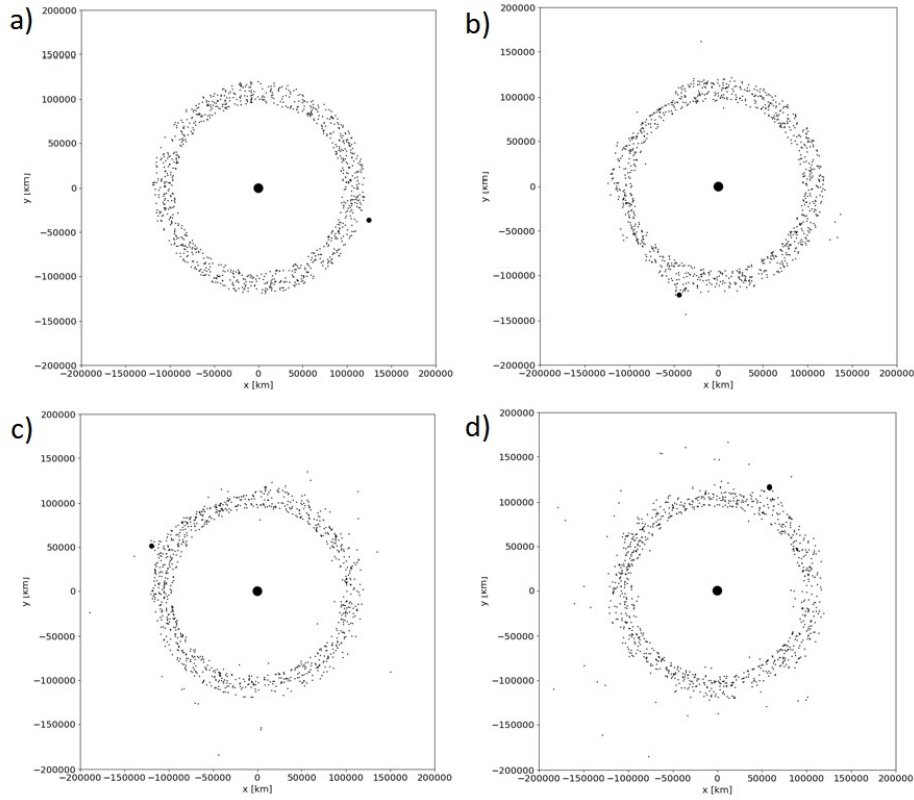


FIGURE 4.4: Simulation of 1000 ring particles around Saturn, with Titan placed artificially close to the rings. The snapshots are taken at a) 0s, b) 108,000s, c) 216,000s and d) 324,000s of integration. The effect of the gravitational pull of Titan shows the delicate equilibrium of the ring system.

4.3.2 A Comment on Symplecticity

The Lagrangian of an N-body problem can be written as

$$\mathcal{L} = K - U = \sum_{i=1}^N K_i - \sum_{i,j=1, i<j}^N U_{ij}, \quad (4.46)$$

where the first term K corresponds to the total kinetic energy of all the N particles in the system, the kinetic energy of each particle is

$$K_i = \frac{1}{2} m_i \mathbf{v}_i^2 \quad (4.47)$$

and U is the total gravitational potential energy, where the binary relation between a particle i and j is given by

$$U_{ij} = -G \frac{m_i m_j}{r_{ij}}. \quad (4.48)$$

The Lagrangian in equation (4.46) does not depend explicitly on time, therefore, there must be a conserved quantity related to temporal invariance, that is the energy. For this case, the Hamiltonian,

$$H(\mathbf{p}_i, \mathbf{r}_i) = K + U = \sum_{i=1}^N K_i + \sum_{i,j=1, i<j}^N U_{ij}, \quad (4.49)$$

corresponds exactly to the total energy, meaning, it is conserved. In the Hamiltonian, the kinetic energy it is now written in terms of the linear momentum of the particles

$$K_i = \frac{\mathbf{p}_i^2}{2m_i}. \quad (4.50)$$

In the previous section, we mentioned that we used the symplectic N-body integrator called *Huayno*, but, what does symplectic mean? A numerical scheme is said to be symplectic if it preserves phase-space area in a dynamical system [16, 30, 31].

In the case of a one dimensional system, symplecticity really corresponds to preservation of the area of a parallelogram P after a certain mapping. As for the N-dimensional case, it corresponds to the preservation of the sum of the oriented areas of the projections of the N-dimensional parallelogram P onto the phase space [30].

Hamiltonian systems that are explicitly independent of time also share these area-preserving properties; then, symplectic integration of these systems will preserve conserved quantities, such as the energy, over long periods of integration. These kind of schemes are also time-reversible, so that the initial conditions can be recovered by running the simulation backward in time.

It is common in a symplectic scheme, to split the Hamiltonian of an N-body system into slowly and rapidly varying parts

$$H = H_{kep} + H_{int}, \quad (4.51)$$

method called *Hamiltonian splitting* [32, 33]. In the case of the Saturn system, the first term H_{kep} represents the interactions between the ring particles and moons with Saturn, and the second term H_{int} represents the interactions between the ring particles and/or moons with each other.

In the example described in the last subsection, there is no collisions between particles, and therefore, the energy should be conserved. Using the *Huayno* integrator should preserve conservation of energy. As a measure of error, we can plot the relative total energy

$$\Delta E = \frac{E_i - E_t}{E_t}$$

against the integration time, as seen in Figure 4.5. E_i corresponds to the total initial energy and E_t is the total energy at each time step.

The first feature that we should notice is the order of magnitude, we realize that the error in the energy stays bounded with a maximum of $\approx -8.5 \times 10^{-9}[-]$, which is pretty good for such a big and chaotic system. The second important characteristic

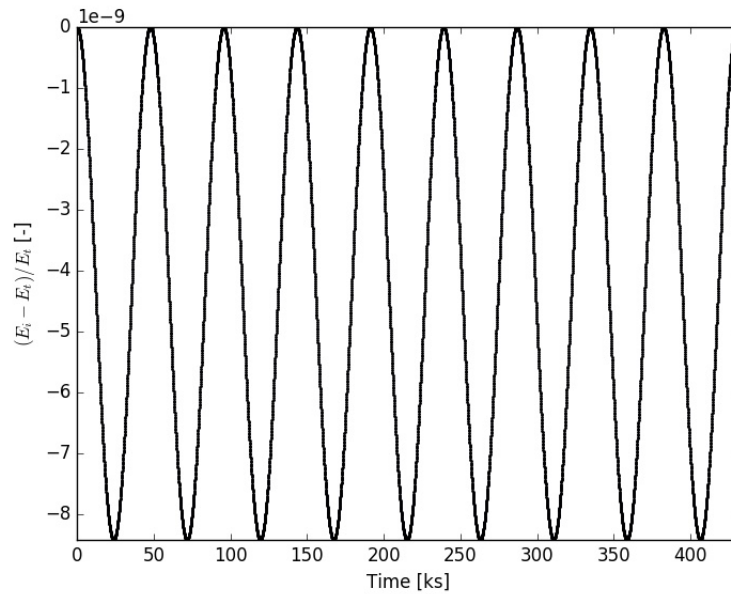


FIGURE 4.5: Relative total energy plotted against time for 5 days of integration. We can see that the maximum error does not exceed the order of magnitude of 10^{-9} even after days of integration.

is the sinusoidal behaviour of the relative energy. To explain why it acts in such a manner, we first need to recognize that the maximum contribution to the total energy is the kinetic and gravitational potential energy of Titan; due to its big mass, it highly surpasses the contribution of the ring particles. Naturally Saturn has a bigger mass, but the planet is considered to be practically static, so that its kinetic energy is considerably smaller than Titan's.

If we compute the orbital period of Titan, given by

$$T = \frac{2\pi}{\Omega}, \quad (4.52)$$

at a position $r = 130,000$ km, we obtain $T \approx 47,820.4$ s. When we compare this number with Figure 4.5, we realize that it corresponds to one period of the relative total energy plot. But, why does the maximum error occurs at each half orbital period and the minimum at each full orbital period? This is a consequence of the time-reversibility of the scheme, which seeks the recovery of the initial conditions by running the simulation backward in time. When Titan is at a half orbital period, it is the furthest away from running the simulation forward or backward and, therefore, the error is maximum. When Titan is approaching a full orbit, no matter if clockwise or counter-clockwise, it is also approaching its initial position, where the error is minimum.

In theory, symplectic schemes ensure reversibility, but in reality it is hard to recover the exact initial conditions by running the simulation backward in time, since even a small change in the initial backward conditions can lead to a big difference in the particles trajectories for such a chaotic system.

4.4 Summary

In this chapter we derived the radial equation for two particles orbiting one another due to a conservative central force. We reduced the problem to a *virtual particle* having a mass μ orbiting around the center of mass. When one of the particles has a mass much bigger than the other, we can consider that the center of mass is approximately in the center of the bigger body which is practically static and the smaller body orbits around the former.

For the case when the eccentricity is zero, we derived the angular velocity at which the small mass m_1 orbits the bigger one m_2 ; the so called Kepler Frequency

$$\Omega \approx \sqrt{\frac{Gm_2}{r^3}}. \quad (4.53)$$

This parameter is rather important, since it is the basis for realistic initial conditions and sets the time scale for orbital motion.

In an N-body problem, when we want to take into account the self-gravity of all the particles, we posed the set of equations to solve

$$\mathbf{a}_i \equiv \ddot{\mathbf{r}}_i = G \sum_{j \neq i}^N m_j \frac{(\mathbf{r}_j - \mathbf{r}_i)}{|\mathbf{r}_j - \mathbf{r}_i|^3}, \quad (4.54)$$

and showed an example of an N-body integrator that solves this equation within the AMUSE framework.

Chapter 5

Motion in a Rotating Reference Frame

In the last chapter we derived the radial orbital equation and its solution for two particles orbiting one another and made the approximation that one of the particles has a much bigger mass, such that it is considered to be static, and the smaller particle orbits around it in a circular manner. This was done knowing that Newton's law of universal gravitation

$$\mathbf{F} = Gm_1m_2 \frac{(\mathbf{r}_1 - \mathbf{r}_2)}{|\mathbf{r}_1 - \mathbf{r}_2|^3} \quad (5.1)$$

applies for an inertial reference frame, which in our case we chose the one of the center of mass; with m_1 and m_2 the masses of the particles at positions \mathbf{r}_1 and \mathbf{r}_2 respectively from this reference frame.

However, sometimes it is useful, depending on the problem we want to address, to work in the reference frame of the orbiting particle. As an example we can take the case we are interested in; if we want to simulate particles that move in the vicinity of a small moon orbiting a planet, it is natural to think of that moonlet as the origin of the coordinate system. Nevertheless, it is a non-inertial reference frame given that it undergoes a centripetal acceleration due to its circular motion.

Newton's second law of motion only applies in an inertial reference frame [26], therefore, it is necessary to develop a theory for non-inertial ones, where we can work with a *Newton-like* law of motion. This chapter develops the necessary tools, and a bit more, to address our moonlet problem. The theory of motion in non-inertial reference frames can be found in books like the ones mentioned in the last chapter (Marion [26], Taylor [27] and Goldstein [28]) to different extent. In Section 5.1, we will follow closely the derivation made by Marion [26] for the theory of non-inertial reference frames and later, in Section 5.2, apply the results for the motion in the rotational reference frame of a moon.

5.1 General Non-inertial Reference Frames

First, we will consider two frames of reference: one fixed (with respect to fixed stars if you wish), that will be denoted with the primed coordinates x'_i , where $i = 1, 2, 3$; and a rotating one denoted with coordinates x_i , where also $i = 1, 2, 3$. Let us study a

particle P that has a position vector \mathbf{r}' with respect to the fixed frame and a position vector \mathbf{r} with respect to the rotating frame, the situation can be seen in Figure 5.1.

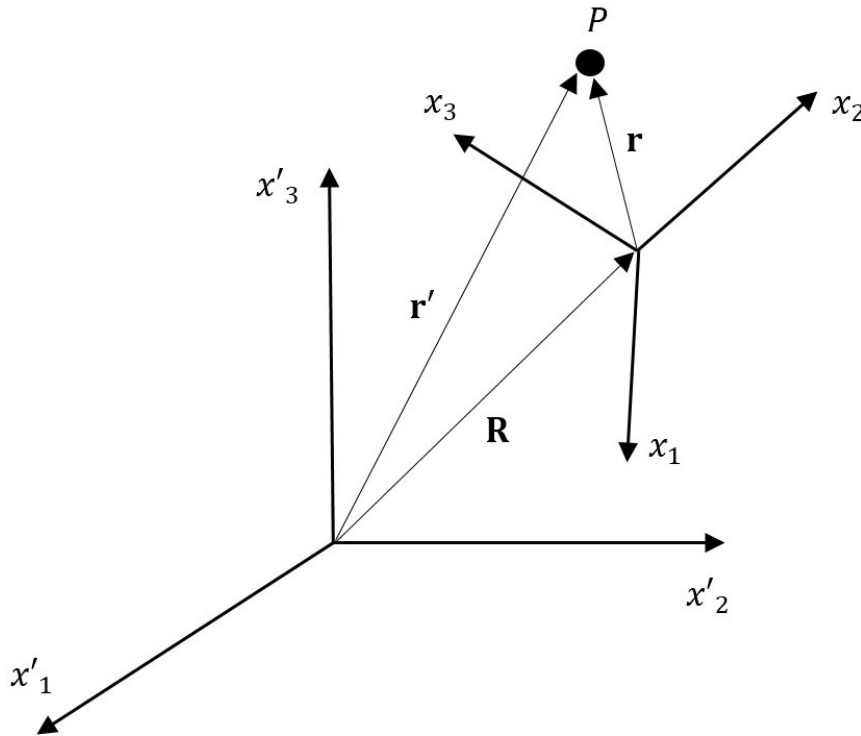


FIGURE 5.1: A particle P has a position vector \mathbf{r}' with respect to a fixed reference frame with coordinates x'_i , but it can also be described with a position vector \mathbf{r} as measured from a rotating reference frame with coordinates x_i . The way to relate both vectors is through \mathbf{R} , which connects both reference frames.

Now, if we call \mathbf{R} to the vector that goes from the origin of the fixed frame to the origin of the rotating one, then the relation between \mathbf{r}' and \mathbf{r} is given by

$$\mathbf{r}' = \mathbf{R} + \mathbf{r}. \quad (5.2)$$

If the rotating system x_i experiences an infinitesimal rotation $\delta\boldsymbol{\theta}$, and the particle P has an infinitesimal displacement $\delta\mathbf{r}$ with respect to the rotating system, then the motion of P can be described using

$$(\delta\mathbf{r})_f = (\delta\mathbf{r})_r + \delta\boldsymbol{\theta} \times \mathbf{r}. \quad (5.3)$$

We will use the subscript f when we mean quantities measured in the *fixed* coordinate system x'_i and we will write the subscript r when they are measured in the *rotating* coordinate system x_i .

If we divide equation (5.3) by the infinitesimal time interval δt at which the rotation and displacement occurs and take the limit when $\delta t \rightarrow 0$, we get the rate of change of \mathbf{r} measured from the fixed coordinate system

$$\left(\frac{d\mathbf{r}}{dt}\right)_f = \left(\frac{d\mathbf{r}}{dt}\right)_r + \frac{d\boldsymbol{\theta}}{dt} \times \mathbf{r}, \quad (5.4)$$

the quantity $\frac{d\boldsymbol{\theta}}{dt}$ is the angular velocity of the rotating reference frame

$$\boldsymbol{\omega} = \frac{d\boldsymbol{\theta}}{dt} \quad (5.5)$$

then we rewrite (5.4) as

$$\left(\frac{d\mathbf{r}}{dt}\right)_f = \left(\frac{d\mathbf{r}}{dt}\right)_r + \boldsymbol{\omega} \times \mathbf{r}. \quad (5.6)$$

Equation (5.6) is not only valid for the position vector \mathbf{r} but for any arbitrary vector \mathbf{Q}

$$\left(\frac{d\mathbf{Q}}{dt}\right)_f = \left(\frac{d\mathbf{Q}}{dt}\right)_r + \boldsymbol{\omega} \times \mathbf{Q}, \quad (5.7)$$

this is an important relation that we will use throughout the chapter. For example, if we apply (5.7) to the angular velocity $\boldsymbol{\omega}$ of the rotating system

$$\left(\frac{d\boldsymbol{\omega}}{dt}\right)_f = \left(\frac{d\boldsymbol{\omega}}{dt}\right)_r + \boldsymbol{\omega} \times \boldsymbol{\omega} = \left(\frac{d\boldsymbol{\omega}}{dt}\right)_r = \dot{\boldsymbol{\omega}}, \quad (5.8)$$

we notice that the angular acceleration $\dot{\boldsymbol{\omega}}$ is the same as measured from the fixed or the rotating frame.

We can also take a look at the derivative with respect to time of the vector \mathbf{r}' as measured from the fixed frame $\left(\frac{d\mathbf{r}'}{dt}\right)_f$.

Remember that \mathbf{r}' points from the origin of the fixed system to the particle P and that $\mathbf{r}' = \mathbf{R} + \mathbf{r}$, so we can write its rate of change as

$$\left(\frac{d\mathbf{r}'}{dt}\right)_f = \left(\frac{d\mathbf{R}}{dt}\right)_f + \left(\frac{d\mathbf{r}}{dt}\right)_f, \quad (5.9)$$

employing the formula (5.7) to the second term in the right hand side of (5.9) we arrive at

$$\left(\frac{d\mathbf{r}'}{dt}\right)_f = \left(\frac{d\mathbf{R}}{dt}\right)_f + \left(\frac{d\mathbf{r}}{dt}\right)_r + \boldsymbol{\omega} \times \mathbf{r}. \quad (5.10)$$

Now following the notation of Marion [26], it is practical to make the following definitions

$$\begin{aligned}
\mathbf{v}_f &= \dot{\mathbf{r}}_f = \left(\frac{d\mathbf{r}'}{dt} \right)_f \quad (\text{velocity relative to fixed axes}), \\
\mathbf{V} &= \dot{\mathbf{R}}_f = \left(\frac{d\mathbf{R}}{dt} \right)_f \quad (\text{linear velocity of the moving origin}), \\
\mathbf{v}_r &= \dot{\mathbf{r}}_r = \left(\frac{d\mathbf{r}}{dt} \right)_r \quad (\text{velocity relative to rotating axes}),
\end{aligned} \tag{5.11}$$

and equation (5.10) takes the shorter form

$$\mathbf{v}_f = \mathbf{V} + \mathbf{v}_r + \boldsymbol{\omega} \times \mathbf{r}. \tag{5.12}$$

In order to formulate a *Newton-like* equation of motion, we will need the acceleration \mathbf{a}_r as measured from the rotating reference frame, so as to be able to write

$$\mathbf{F}_{\text{eff}} = m\mathbf{a}_r = m \left(\frac{d\mathbf{v}_r}{dt} \right)_r, \tag{5.13}$$

for doing so, we take the derivative with respect to time of equation (5.12) as measured from the fixed system

$$\left(\frac{d\mathbf{v}_f}{dt} \right)_f = \left(\frac{d\mathbf{V}}{dt} \right)_f + \left(\frac{d\mathbf{v}_r}{dt} \right)_f + \dot{\boldsymbol{\omega}} \times \mathbf{r} + \boldsymbol{\omega} \times \left(\frac{d\mathbf{r}}{dt} \right)_f, \tag{5.14}$$

taking into account that the angular acceleration does not change irrespective of the reference frame. Let us work out the equation (5.14) a bit further. The left hand side of (5.14) is just the acceleration with respect to the fixed coordinate system

$$\mathbf{a}_f = \left(\frac{d\mathbf{v}_f}{dt} \right)_f. \tag{5.15}$$

The linear acceleration of the rotating frame can be denoted as

$$\ddot{\mathbf{R}} = \left(\frac{d\mathbf{V}}{dt} \right)_f, \tag{5.16}$$

we can again use the formula (5.7) to express the second term of the right hand side in equation (5.14) as

$$\begin{aligned}
\left(\frac{d\mathbf{v}_r}{dt} \right)_f &= \left(\frac{d\mathbf{v}_r}{dt} \right)_r + \boldsymbol{\omega} \times \mathbf{v}_r \\
&= \mathbf{a}_r + \boldsymbol{\omega} \times \mathbf{v}_r,
\end{aligned} \tag{5.17}$$

notice that the acceleration of the particle with respect to the rotating frame, \mathbf{a}_r , has appeared. And the last term of (5.14) is expanded to be

$$\begin{aligned}\boldsymbol{\omega} \times \left(\frac{d\mathbf{r}}{dt} \right)_f &= \boldsymbol{\omega} \times \left(\frac{d\mathbf{r}}{dt} \right)_r + \boldsymbol{\omega} \times (\boldsymbol{\omega} \times \mathbf{r}) \\ &= \boldsymbol{\omega} \times \mathbf{v}_r + \boldsymbol{\omega} \times (\boldsymbol{\omega} \times \mathbf{r}).\end{aligned}\quad (5.18)$$

It is now possible to recast Newton's second law of motion: $\mathbf{F} = m\mathbf{a}_f$, using equations (5.14)-(5.18)

$$\mathbf{F} = m\mathbf{a}_f = m\ddot{\mathbf{R}}_f + m\mathbf{a}_r + m\dot{\boldsymbol{\omega}} \times \mathbf{r} + m\boldsymbol{\omega} \times (\boldsymbol{\omega} \times \mathbf{r}) + 2m\boldsymbol{\omega} \times \mathbf{v}_r, \quad (5.19)$$

and, after solving for $m\mathbf{a}_r$ we are finally able to express a *Newton-like* equation

$$\mathbf{F}_{\text{eff}} = m\mathbf{a}_r = \mathbf{F} - m\ddot{\mathbf{R}}_f - m\dot{\boldsymbol{\omega}} \times \mathbf{r} - m\boldsymbol{\omega} \times (\boldsymbol{\omega} \times \mathbf{r}) - 2m\boldsymbol{\omega} \times \mathbf{v}_r. \quad (5.20)$$

Let us analyse the right hand side of equation (5.20). The first term \mathbf{F} corresponds to any external force, such as gravity for example. Then, $-m\ddot{\mathbf{R}}_f$ arises due to the linear acceleration of the rotating reference frame, which is zero if the system moves with linear constant velocity. The term $-m\dot{\boldsymbol{\omega}} \times \mathbf{r}$ stems from the angular acceleration and disappears if the angular velocity is constant or the angular acceleration is parallel to the vector position \mathbf{r} . The last two terms receive special names: the centrifugal force

$$\mathbf{F}_{\text{cent}} = -m\boldsymbol{\omega} \times (\boldsymbol{\omega} \times \mathbf{r}), \quad (5.21)$$

dependent on the position of the particle, and the Coriolis force

$$\mathbf{F}_{\text{cor}} = -2m\boldsymbol{\omega} \times \mathbf{v}_r, \quad (5.22)$$

dependent on its velocity with respect to the rotating frame.

5.2 Rotating Reference Frame of a Moon

5.2.1 Forces in the Rotating Reference Frame of a Moon

Now let us work out the problem we are interested in, where we want to simulate a particle, or better said, many particles that move in the vicinity of a moonlet orbiting Saturn. Each one of these particles will feel an effective force given by

$$\mathbf{F}_{\text{eff}} = \sum_i \mathbf{F}_i - m\ddot{\mathbf{R}}_f - m\dot{\boldsymbol{\omega}} \times \mathbf{r} - m\boldsymbol{\omega} \times (\boldsymbol{\omega} \times \mathbf{r}) - 2m\boldsymbol{\omega} \times \mathbf{v}_r, \quad (5.23)$$

in the rotating reference frame, which is just equation (5.20) but with $\sum_i \mathbf{F}_i$ representing the gravitational forces due to Saturn \mathbf{F}_S and the moonlet \mathbf{F}_M ,

$$\sum_i \mathbf{F}_i = \mathbf{F}_S + \mathbf{F}_M.$$

We need to make further simplifications to equation (5.23); we consider the static and inertial reference frame to be in the center of Saturn and the rotating reference frame at the center of the moonlet that is orbiting at a constant radius \mathbf{R} , as seen from Figure 5.2.

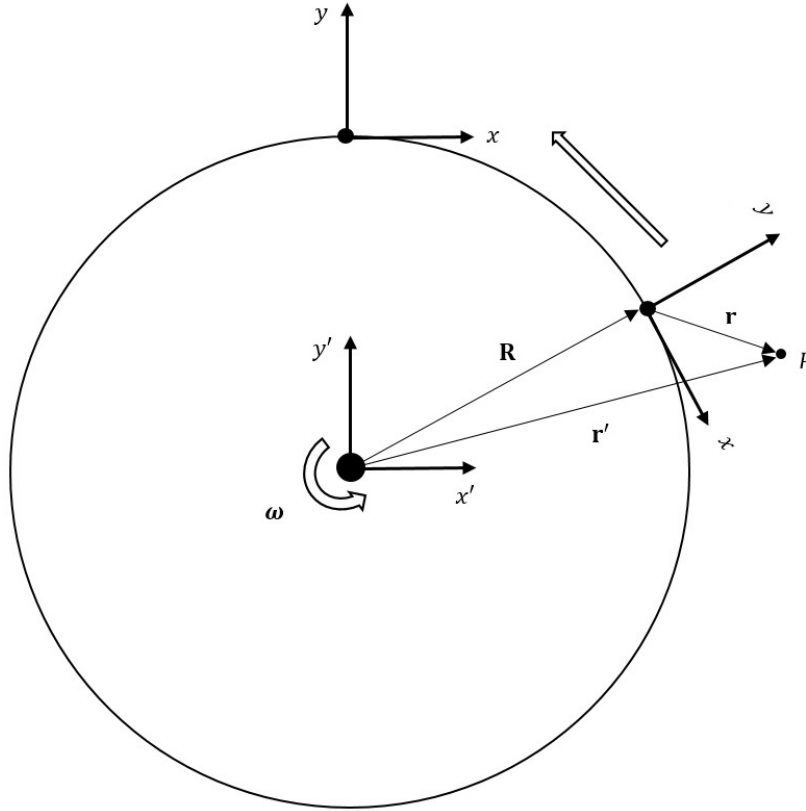


FIGURE 5.2: A diagram representing a fixed reference frame at the center of Saturn with coordinates x'_i . A moonlet is orbiting Saturn with angular velocity ω , then a second reference frame with coordinates x_i is placed in the center of the moonlet following its rotation. A particle P moving in its vicinity can be described in both coordinate systems.

We assume that the moonlet is in a stable circular orbit with constant angular velocity ω , therefore the angular acceleration is zero, $\dot{\omega} = 0$ and the effective force becomes

$$\mathbf{F}_{\text{eff}} = \mathbf{F}_S + \mathbf{F}_M - m\ddot{\mathbf{R}}_f - m\omega \times (\omega \times \mathbf{r}) - 2m\omega \times \mathbf{v}_r, \quad (5.24)$$

one can naively think that $m\ddot{\mathbf{R}}_f = 0$, but just remember that the derivatives are done with respect to the fixed system (thus the subscript f), hence we need to make use of the formula (5.7) twice

$$\ddot{\mathbf{R}}_f = \omega \times \dot{\mathbf{R}}_f = \omega \times (\omega \times \mathbf{R}), \quad (5.25)$$

given that the rate of change of \mathbf{r} in the rotating system is zero. Inserting now (5.25) into (5.24) yields

$$\begin{aligned}
\mathbf{F}_{\text{eff}} &= \mathbf{F}_S + \mathbf{F}_M - m\boldsymbol{\omega} \times (\boldsymbol{\omega} \times \mathbf{R}) - m\boldsymbol{\omega} \times (\boldsymbol{\omega} \times \mathbf{r}) - 2m\boldsymbol{\omega} \times \mathbf{v}_r \\
&= \mathbf{F}_S + \mathbf{F}_M - m\boldsymbol{\omega} \times (\boldsymbol{\omega} \times (\mathbf{r} + \mathbf{R})) - 2m\boldsymbol{\omega} \times \mathbf{v}_r \\
&= \mathbf{F}_S + \mathbf{F}_M + \mathbf{F}_{\text{cent}} + \mathbf{F}_{\text{cor}},
\end{aligned} \tag{5.26}$$

where we have written the four forces \mathbf{F}_i acting on a particle moving in this rotating system.

It is finally time to write the forces explicitly. Consider Saturn, with mass M_S , situated at the origin of the fixed reference frame and at $\mathbf{r}_S = (0, -r_0)$ from the rotating reference frame; and a moonlet, with mass M_M , is orbiting in a stable circular orbit with Kepler Frequency $\boldsymbol{\omega} = \Omega_0 \hat{e}_k$, situated at the origin of the rotating reference frame $\mathbf{r}_M = (0, 0)$. The vector that connects the origins of both systems is given by $\mathbf{R} = (0, r_0)$.

Consider a particle P having a mass m , with $\mathbf{r} = (x, y)$ its position vector and $\mathbf{v}_r = (v_x, v_y)$ its velocity with respect to the rotating reference frame. Then, the forces acting on this particle in the rotating reference frame are:

The gravitational force of Saturn,

$$\mathbf{F}_S = GM_S m \frac{(\mathbf{r}_S - \mathbf{r})}{|\mathbf{r}_S - \mathbf{r}|^3} = -GM_S m \frac{(x, y + r_0)}{(x^2 + (y + r_0)^2)^{3/2}}, \tag{5.27}$$

the gravitational force of the moonlet,

$$\mathbf{F}_M = GM_M m \frac{(\mathbf{r}_M - \mathbf{r})}{|\mathbf{r}_M - \mathbf{r}|^3} = -GM_M m \frac{(x, y)}{(x^2 + y^2)^{3/2}}, \tag{5.28}$$

the centrifugal force

$$\mathbf{F}_{\text{cent}} = -m\boldsymbol{\omega} \times (\boldsymbol{\omega} \times (\mathbf{r} + \mathbf{R})) = m(x\Omega_0^2, (y + r_0)\Omega_0^2), \tag{5.29}$$

and the Coriolis force,

$$\mathbf{F}_{\text{cor}} = -2m\boldsymbol{\omega} \times \mathbf{v}_r = 2m(v_y\Omega_0, -v_x\Omega_0). \tag{5.30}$$

In Chapter IV we derived the Kepler Frequency

$$\Omega \approx \sqrt{\frac{Gm_2}{r^3}}, \tag{5.31}$$

for a small object orbiting a much bigger one. We can take the case of Saturn and a moonlet at a distance r_0 , then $m_2 = M_S$ and $r = r_0$, so that the expression for Ω_0 becomes

$$\Omega_0 \approx \sqrt{\frac{GM_S}{r_0^3}}. \tag{5.32}$$

5.2.2 Velocity Shear in the Reference Frame of a Moon

The Coriolis force depends on the velocity of the particle as measured from the rotating reference frame, however we have not written an expression for it yet; that is the goal of this section. Now, consider that there is not only one particle but thousands, a sector of the planetary ring. In the fixed coordinate system of Saturn we are able to *see* the whole ring so it is natural to use polar coordinates to describe it, but when we want to study just a sector, it is convenient to work with the rotating local Cartesian reference frame located at a distance $R = r_0$, as seen in Figure 5.2.

We derived in Chapter IV, and revisited just in the last section, the Kepler Frequency (5.32); from that equation we notice that the difference in the velocities of the inner and outer particles of the ring induce a constant shear. The problem arises when we want to apply an expression derived in a fixed system with polar coordinates, into a rotating Cartesian one. Thankfully, we can make use of equation (5.12) and linearise equation (5.32) to write an expression for the shear velocity in the rotating Cartesian system, without taking into account the effect of a moonlet.

From (5.12), we want to know the velocity relative to the rotating axes \mathbf{v}_r

$$\mathbf{v}_r = \mathbf{v}_f - \mathbf{V} - \boldsymbol{\omega} \times \mathbf{r}, \quad (5.33)$$

using (5.7) we notice that $\mathbf{V} = \boldsymbol{\omega} \times \mathbf{R}$ so

$$\mathbf{v}_r = \mathbf{v}_f - (\boldsymbol{\omega} \times (\mathbf{r} + \mathbf{R})). \quad (5.34)$$

Now, the Keplerian velocity of a particle P orbiting Saturn at a distance r' as measured from the fixed system is just

$$\mathbf{v}_f = r' \Omega \hat{e}_\phi = \sqrt{\frac{GM_S}{r'}} \hat{e}_\phi, \quad (5.35)$$

with \hat{e}_ϕ the unit vector in the azimuthal direction. We can rewrite equation (5.35) as

$$\begin{aligned} \mathbf{v}_f &= \sqrt{GM_S} r'^{-1/2} \begin{pmatrix} -\frac{y'}{r'} & \frac{x'}{r'} \end{pmatrix} \\ &= \sqrt{GM_S} \left[((y+r_0)^2 + x^2)^{1/2} \right]^{-3/2} (-y', x') \\ &\approx \sqrt{GM_S} (y+r_0)^{-3/2} (-y', x'), \end{aligned} \quad (5.36)$$

where we have used the fact that $\mathbf{r}' = (x', y')$, $(x', y') = (x, y + r_0)$ and $\frac{x}{y+r_0} \ll 1$. Continuing with the calculation in (5.36)

$$\begin{aligned}
\mathbf{v}_f &\approx -\sqrt{GM_S} (y+r_0)^{-3/2} (y+r_0, -x) \\
&= -\sqrt{GM_S} (y+r_0)^{-3/2} r_0 (1+y/r_0, -x/r_0) \\
&\approx -\sqrt{GM_S} r_0^{-1/2} \left(1 - \frac{3y}{2r_0}\right) (1+y/r_0, -x/r_0) \\
&\approx -\sqrt{\frac{GM_S}{r_0}} \left(1 + \frac{y}{r_0} - \frac{3y}{2r_0}, -\frac{x}{r_0}\right), \tag{5.37}
\end{aligned}$$

using $\frac{y}{r_0} \ll 1$ and neglecting second order terms. For the second term in the right-hand-side of equation (5.34)

$$\begin{aligned}
\boldsymbol{\omega} \times (\mathbf{r} + \mathbf{R}) &= -\Omega_0 (y+r_0, -x) \\
&= -\sqrt{\frac{GM_S}{r_0^3}} (y+r_0, -x) \\
&= -\sqrt{\frac{GM_S}{r_0}} \left(1 + \frac{y}{r_0}, -\frac{x}{r_0}\right). \tag{5.38}
\end{aligned}$$

Inserting (5.37) and (5.38) into equation (5.34) we arrive at the linearised expression for the shear velocity in the rotating Cartesian reference frame

$$\begin{aligned}
\mathbf{v}_r &= \frac{3y}{2r_0} \sqrt{\frac{GM_S}{r_0}} \hat{e}_x \\
&= \frac{3y}{2} \sqrt{\frac{GM_S}{r_0^3}} \hat{e}_x \\
&= \frac{3}{2} \Omega_0 y \hat{e}_x. \tag{5.39}
\end{aligned}$$

The only non-zero component of the velocity of the particles in the rotating axes is in the x direction and dependent on the position y , as it should be for a constant shear velocity. Equation (5.39) gives us the average velocity of a system of particles moving in a ring section, schematically it is shown in Figure 5.3. Further on, we will use this expression to implement realistic initial and boundary conditions to the simulations with and without a moonlet.

5.3 Summary

Newton's second law does not apply for non-inertial reference frames, therefore, we tasked ourselves to derive a Newton-like equation where we can describe the motion of a particle even in non-inertial reference frames. We arrived at the general expression

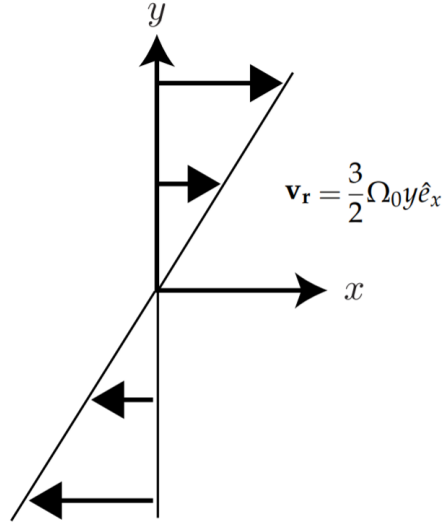


FIGURE 5.3: Plane shear for a ring section given by equation (5.39).

$$\mathbf{F}_{\text{eff}} = m\mathbf{a}_r = \mathbf{F} - m\ddot{\mathbf{R}}_f - m\dot{\boldsymbol{\omega}} \times \mathbf{r} - m\boldsymbol{\omega} \times (\boldsymbol{\omega} \times \mathbf{r}) - 2m\boldsymbol{\omega} \times \mathbf{v}_r. \quad (5.40)$$

Then, we made use of this equation to write the forces that affect a particle moving in the vicinity of a moonlet orbiting Saturn as measured in its reference frame:

$$\mathbf{F}_S = -GM_S m \frac{(x, y + r_0)}{(x^2 + (y + r_0)^2)^{3/2}}, \quad (5.41)$$

$$\mathbf{F}_M = -GM_M m \frac{(x, y)}{(x^2 + y^2)^{3/2}}, \quad (5.42)$$

$$\mathbf{F}_{\text{cent}} = m(x\Omega_0^2, (y + r_0)\Omega_0^2), \quad (5.43)$$

$$\mathbf{F}_{\text{cor}} = 2m(v_y\Omega_0, -v_x\Omega_0). \quad (5.44)$$

Finally, we derived an expression for the linearised shear velocity of the particles in the rotating reference frame attached to a moonlet

$$\mathbf{v}_r = \frac{3}{2} \Omega_0 y \hat{e}_x, \quad (5.45)$$

which will be necessary for initial and boundary conditions in the simulations.

Chapter 6

Ring Section and Propellers Simulations

Throughout this thesis, we have developed the basic theory of granular matter and coarse graining; we went through gravitational dynamics and derived the forces that a particle overcomes when we *see* it from a non-inertial reference frame. In this chapter we are going to apply what we have discussed until now; we will start with an elementary simulation in MercuryDPM, a section of the ring with no influence of a moonlet, to be able to compare the results with the next set of simulations, where we insert a moonlet and follow the evolution of the ring section in its frame of reference.

6.1 Simulations of Ring Sections

Consider a planar section of a ring, where a local Cartesian coordinate system is placed in the middle of the simulation box with dimensions ($L_x = 18,000$ m, $L_y = 2,000$ m). The reference frame orbits Saturn at a distance of $r_0 = 117,000$ km such that $\Omega_0 = 1.538 \times 10^{-4}$ s $^{-1}$ and an orbital period of $T_0 = 40,852.96$ s; 30,000 spherical particles of radii $a = 2$ m and a density of 500 kg/m 3 are positioned randomly on the equatorial plane.

As initial conditions, the granules are placed inside the box with an initial velocity given by equation (5.45)

$$\mathbf{v}_r = \frac{3}{2}\Omega_0 y \hat{e}_x,$$

according to their y coordinate, but with a small velocity dispersion of $0.01|\mathbf{v}_r|$.

For the collisions between the grains, we use the linear contact model described in Chapter II, section 2.3. The coefficient of restitution of the particles, given by equation (2.39)

$$\epsilon = e^{-\eta t_c},$$

is fixed at $\epsilon = 0.25$ unless specified otherwise; for this case we consider them to be frictionless. Simulations in the range $\epsilon \in [0.15, 0.99]$ did not show any peculiarity or major difference for the same geometry, number of particles and time of integration, therefore we chose $\epsilon = 0.25$ as an exemplary case.

In the absence of a moonlet, the forces that the particles experience as measured in the rotating reference frame are given by equations (5.41), (5.43) and (5.44)

$$\begin{aligned}\mathbf{F}_S &= -GM_S m \frac{(x, y + r_0)}{(x^2 + (y + r_0)^2)^{3/2}}, \\ \mathbf{F}_{\text{cent}} &= m(x\Omega_0^2, (y + r_0)\Omega_0^2), \\ \mathbf{F}_{\text{cor}} &= 2m(v_y\Omega_0, -v_x\Omega_0),\end{aligned}$$

respectively. Self-gravity was not included due to limiting computational time, but we consider that it is not so relevant for such a dilute case. We have mentioned almost all the necessary elements for the simulation, except for one: the boundary conditions. We will use a special kind of boundary conditions called Lees-Edwards that we will describe in the next subsection.

6.1.1 Lees-Edwards Boundary Conditions

As the name suggests, these boundary conditions were created by Lees & Edwards in 1972 [34] for Molecular Dynamics simulations. The goal of these boundary conditions was to achieve an uniform shear velocity profile

$$\mathbf{v} = \dot{\gamma}y\hat{e}_x, \quad (6.1)$$

being $\dot{\gamma}$ a constant shear rate. In a 2D simulation, where the positions of the particles are given by (x, y) , their velocities are (v_x, v_y) and the computational domain has dimensions of (L_x, L_y) with the origin of the coordinates at the center, the particles that leave the box in the direction perpendicular to the velocity gradient \hat{e}_y are reinserted at the mirror boundary with the same velocity and mirror position, i.e., if a particle leaves from the left or from the right boundary with a certain velocity, it is inserted in the right or left boundary respectively with the same velocity and the same y coordinate; these are called periodic boundary conditions. However, particles leaving in the $\pm\hat{e}_y$ direction (top or bottom boundaries) are reinserted with their x -velocity decreased (or increased if leaving from the bottom boundary) by the shear velocity

$$\Delta\mathbf{v} = \dot{\gamma}L_y\hat{e}_x,$$

at a position given by their mirror image displaced by the time-dependent offset

$$d_x = t|\Delta\mathbf{v}|.$$

Mathematically the Lees-Edwards boundary conditions are described by

$$x^* = \begin{cases} (x - d_x) \bmod L_x, & y > L_y/2 \\ x \bmod L_x, & -L_y/2 \leq y \leq L_y/2 \\ (x + d_x) \bmod L_x, & y < -L_y/2 \end{cases}$$

$$y^* = y \bmod L_y,$$

$$v_x^* = \begin{cases} v_x - \Delta v_x, & y > L_y/2 \\ v_x, & -L_y/2 \leq y \leq L_y/2 \\ v_x + \Delta v_x, & y < -L_y/2 \end{cases}$$

$$v_y^* = v_y,$$

where the * quantities refer to the positions or velocities after the particles are reinserted and mod represents the modular function [35, 36]. Comparing equation (6.1) with (5.45), we realize that the shear rate corresponds to the linearised Keplerian one

$$\dot{\gamma} = \frac{3}{2}\Omega_0. \quad (6.2)$$

6.1.2 Ring Sections and Coarse Graining

In astrophysics it is common to use the optical depth τ as a measurement of transparency or opaqueness, for planetary rings for example. It is defined by some authors [37, 38] as

$$\tau = \int \int 2\pi a n(x, y, z, a) dz da, \quad (6.3)$$

with a being the radius of the particles and n the 3D number density dependent on the coordinates and the radius itself. By definition, τ can acquire values from 0 and even bigger than 1; however, when we consider a monodisperse and pseudo-two-dimensional ring as our case, the expression for the optical depth simplifies to

$$\tau = \frac{N\pi a^2}{L_x L_y}, \quad (6.4)$$

which corresponds exactly to the two-dimensional packing fraction ϕ defined in Chapter II. For this example the packing fraction, or optical depth for that matter, is $\phi \approx 0.01$, a very dilute case.

If the diameter of the particles is d and a typical velocity is v , the collision rate goes like $2dvn$, with n being now the 2D number density. The mean free path in the 2D plane is the typical velocity times the inverse of the collision rate

$$\lambda \sim \frac{1}{2dn},$$

then, $\lambda \sim 150$ m in this case.

After integrating for one orbital period T_0 , we can examine the state of the box. In Figure 6.1 we see the full computational domain with all the particles inside; the radius of the particles was enhanced by a factor 4 in order to see them clearly.

Figure 6.1 does not tell us many things, since there is no visible structure or important feature. However, making use of the Coarse Graining theory developed in

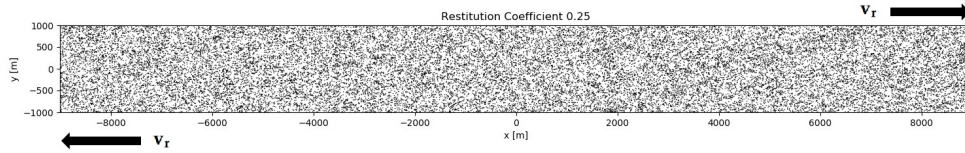


FIGURE 6.1: Ring section with 30,000 particles of 2 m of radius integrated around one orbit with $\epsilon = 0.25$.

Chapter III and the built-in statistics package of MercuryDPM we can obtain coarse grained fields that show us more about the system.

In Figure 6.2 we see four images of different coarse grained fields. They were obtained using a Gaussian coarse graining function with $w = 100$ m. The choice of the width w depends mostly on the sizes of the particles and the structures formed in the system. There are no visible structures in the ring section, and a width of $\mathcal{O}(10$ m) or shorter than the particle radius would be very small to build a continuous smooth field, thus, a typical size can be the mean free path of $\mathcal{O}(100$ m), hence the choice $w = 100$ m.

The fields were time averaged over 1000 s with 10,000 evaluation points spread evenly on a grid over the domain $[-9000, 9000] \times [-1000, 1000]$.

The first field shown in Figure 6.2 corresponds to the coarse grained density in 2D,

$$\Sigma = \frac{3\rho}{4a},$$

where ρ is the coarse grained density defined in equation (3.37), plotted in a logarithmic scale to highlight any possible structures. This will be important for the next set of simulations with a moonlet, for now, we notice that the density field is rather homogeneous with some random fluctuations over the domain.

For the following three fields we need to make an important definition. It is clear that the purpose of the Lees-Edwards boundary conditions is to create an uniform shear velocity profile as given by \mathbf{v}_r , equation (5.45); nevertheless, we also mentioned that we introduced a velocity fluctuation $\delta\mathbf{v}$ in the particles, as it is normal for a granular gas, then it is natural to separate the total velocity of the particles in a Reynolds-like decomposition

$$\mathbf{v} = \mathbf{v}_r + \delta\mathbf{v}, \quad (6.5)$$

where the first term of the right-hand-side corresponds to the unperturbed or averaged velocity field defined in equation (5.45) and the second term are the fluctuations. The unperturbed velocity has only one component in the x direction, so that any component of the velocity in the y direction is considered as a fluctuation $v_y = \delta v_y$. Remember that \mathbf{v} is computed as the coarse grained velocity given by equation (3.39).

The second field in Figure 6.2 represents the fluctuations of the velocity in the x direction, i.e., $\delta v_x = v_x - v_r$, which also looks homogeneous, as well as the third field, the y component of the velocity.

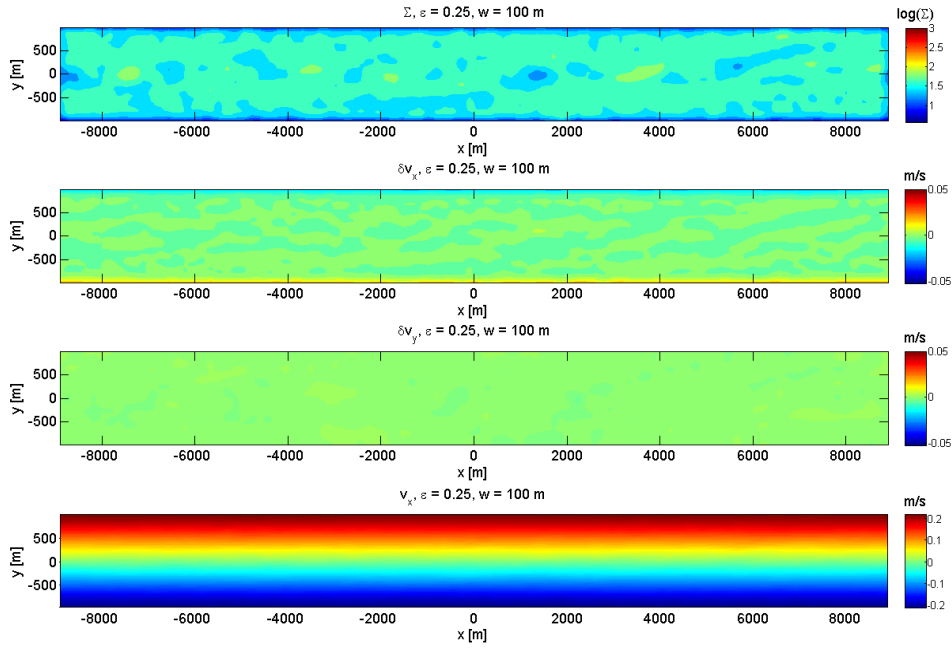


FIGURE 6.2: Coarse grained density, velocity fluctuations in x and y direction, and velocity in x direction for the ring section of Figure 6.1.

Probably the most interesting field for this case is the total coarse grained velocity in x direction, shown in the fourth panel, where we see in a very colourful colour map that indeed the Lees-Edwards boundary conditions created a uniform shear flow. Problems will arise if we lower the density enough so that $\lambda \sim L_y$; then, particles could cross the Lees-Edwards boundaries (multiple times) before colliding, with their velocity being augmented at each crossing. This will lead to a great increment in the granular temperature and disperse the shear velocity profile.

6.2 Simulations of Propellers

6.2.1 Simulations Setup

For the next set of simulations, we consider again a planar section of a ring, but in this case we place a moonlet of radius $r_M = 150$ m and mass $M_M = 1.27 \times 10^{10}$ kg in the middle of the local Cartesian system with dimensions $L_x = 2,000$ m and $L_y = 18,000$ m, like in section 6.1. The moonlet is orbiting Saturn at a distance $r_0 = 117,000$ km such that its Kepler frequency is $\Omega_0 = 1.538 \times 10^{-4} \text{ s}^{-1}$ and the orbital period $T_0 = 40,852.96$ s. The 30,000 frictionless particles of radii $a = 2$ m and density of 500 kg/m^3 are placed randomly over the plane with an initial velocity given by equation (5.45) with a velocity dispersion of $0.01|\mathbf{v}_r|$. In order to keep the shear velocity profile, Lees-Edwards boundary conditions were implemented in the simulations as explained in section 6.1.1.

The forces that the particles feel in the non-inertial reference frame of the moon are the same as the ones specified in section 6.1, plus the gravitational force of the moonlet

$$\mathbf{F}_M = -GM_{Mm} \frac{(x, y)}{(x^2 + y^2)^{3/2}}.$$

Self-gravity was neglected once more.

6.2.2 Propellers

Several simulations with the same initial conditions but different restitution coefficients were performed to study its influence on the creation of propellers. We consider that coefficients of restitution in the range $\epsilon \in [0.15, 0.99]$ are representative to illustrate their effect. After integrating for one orbital period one can already see the creation of these structures, as shown in Figure 6.3, where we show nine different restitution coefficients in this range.

The outcome of the simulations is evident; we can see in Figure 6.3 the state after one orbital period from lower to higher ϵ , from top image to bottom image. The most noticeable propeller is the top one, as expected, where $\epsilon = 0.15$. The low coefficient of restitution allows any structure to last longer since the particles do not simply *bounce off* but lose energy in each collision. The bottom image, where $\epsilon = 0.99$, resembles Figure 6.1 as it looks homogeneous throughout the domain.

Now it is a good moment to make some remarks about the capabilities and drawbacks of the approach used. Using MercuryDPM, it is very simple to vary the coefficient of restitution; it is relatively straightforward to create particles and implement the Lees-Edwards boundary conditions within the MercuryDPM environment, and there are several contact models available. Nevertheless, one problem that arises when studying planetary rings is the extent of its structures, in particular, propellers are quite long, depending on the size of the moonlet and ring particles properties, the *wingspan* of the propellers can be hundreds of kilometers. If the moonlet is big enough, of around 500 m radius approximately, the *blades* of the propeller would be so long that they span the whole planetary ring creating a gap [7, 39]. In that sense, the propellers that we reproduced are not fully developed in time nor in space, and thus they are not in equilibrium.

Since we are not able to simulate the whole azimuthal extent because of computational cost and time, the particles are still perturbed by the moonlet when they cross the periodic boundaries (right and left boundaries). Therefore, we only focus on their creation and compare their states at same times for different restitution coefficients. One advantage is that their complete development is fairly slow (months or years depending on the radial distance, density and particle properties), which will allow us to average in time the coarse grained fields over 1000 seconds to obtain a smooth field, as in section 6.2.3.

In Appendix A, we discuss about one concept that will be essential in the next subsection, the granular temperature T . It is important to be aware of its evolution since a high T might destroy any structure created by the moonlet. The shear induced by the Lees-Edwards boundaries heats up the system considerably more the higher the restitution coefficient. It is found that for $\epsilon < 0.90$ the granular temperature stays bounded within the same order of magnitude as the initial temperature and saturates to its final value at approximately one orbit of integration for $\epsilon = 0.90$; for

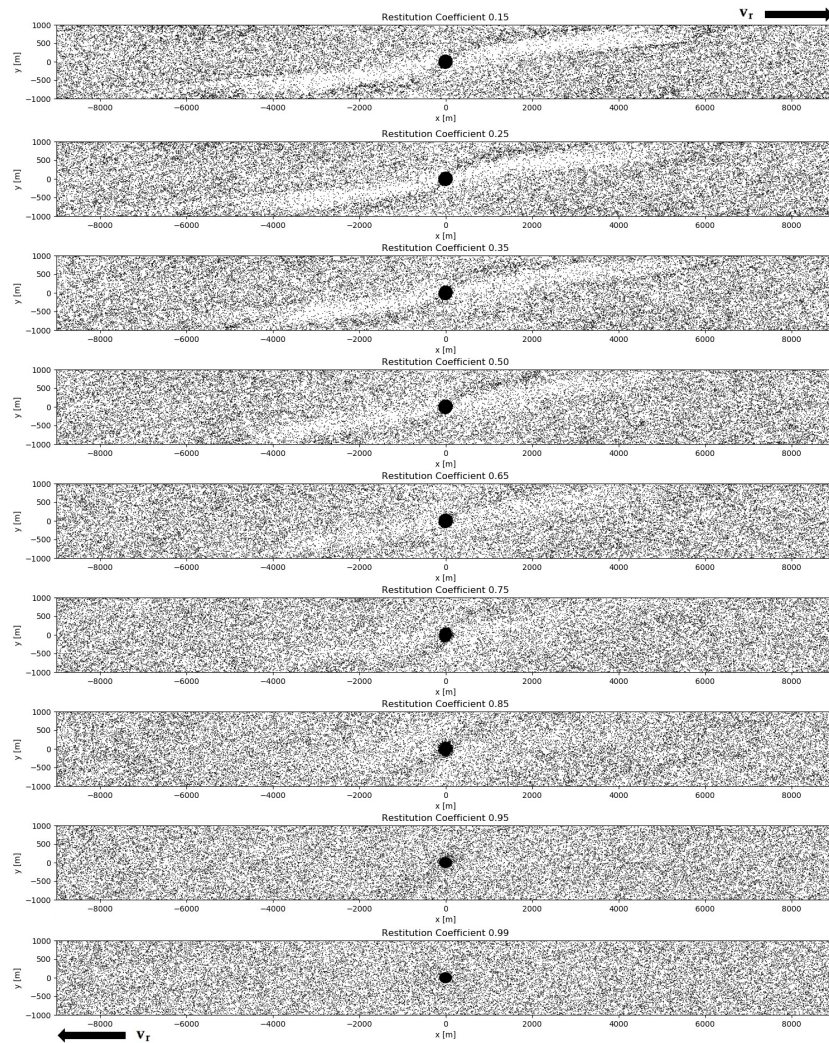


FIGURE 6.3: After the integration of one orbit around Saturn (T_0), one can see the formation of propellers, whose sharpness and length depends on the coefficient of restitution of the particles. The simulations were done with 30,000 particles of 2 m radius each, and $\phi \approx 0.01$.

higher restitution coefficients the saturation time takes more than one orbit and its saturation value can be orders of magnitude higher than the initial temperature.

6.2.3 Coarse Graining of Propeller Simulations

Even though Figure 6.3 allows us to see clearly the *leading* and *trailing edge* of the propellers for low coefficients of restitution, their fading, as we increase ϵ , makes it difficult to distinguish between propeller and no-propeller for $\epsilon = 0.65$ and higher. Therefore we make use of the Coarse Graining tool of MercuryDPM to analyse the data and set a criterion to distinguish when there is no structure at all. In Figure 6.4 we show the coarse grained density in 2D, Σ , in a logarithmic scale to enhance visually any possible structure that might be imperceptible in Figure 6.3. We averaged the fields over 1000 seconds and used a Gaussian coarse graining function with a width $w = 100$ m as in section 6.1, since the mean free path is of similar magnitude.

Before discussing about the most prominent feature of the color maps in Figure 6.4, i.e., the *blades* of the propellers, let us focus on the red spots in the middle of the *hub*, these correspond to high density regions. This is due to particle agglomeration near the stable Lagrangian points L_1 and L_2 inside the Roche lobe, that is the region around the moonlet within which orbiting material is gravitationally bound to it [13, 41]. When the orbital eccentricity of the moonlet is negligible (as it is the case, since we assumed circular motion), the Lagrangian points are approximated by the Hill radius [41]

$$h = r_0 \left(\frac{M_M}{3M_S} \right)^{1/3}, \quad (6.6)$$

$h = 228.5$ m for our system. The Lagrangian points L_1 and L_2 lie on the line that connects Saturn with the moonlet, symmetrically opposite against each other in the case of zero eccentricity, L_1 at $(0, -228.5$ m) and L_2 at $(0, 228.5$ m); any further discussion about Lagrangian points is beyond the scope of this thesis, but we refer to Koon et al. [41]; it is enough for us to know that these Lagrangian points are stable and particles tend to cluster in the region between them, except for the cases $\epsilon = 0.95$ and 0.99 , where the granular temperature becomes so high that these clusters of particles get destroyed by collisions.

Focusing now our attention on the *blades* of the propellers, we must establish a criterion to differentiate when there is no propeller-like structure any more. We follow the idea of Michikoshi & Kokubo [12] and propose that there is no propeller when $\Sigma_{max}/\Sigma_{min} < 2$ along a line of constant x . Notice that this criterion is arbitrary, since it does not necessarily hold for systems with different packing fractions; however, we confirm that a propeller-shaped structure is observed when this condition is satisfied. A limitation to this criterion is that the difference between systems where $\Sigma_{max}/\Sigma_{min} \approx 2$ (values of 1.99 and 2.1 for instance) is not clear and can possibly jump between *propeller* and *no-propeller* state if we slightly change the average time or initial conditions for example.

Keeping these disclaimers in mind, we choose to sample the density along $x = 990$ m to apply our criterion for each coefficient of restitution. In Figure 6.5 we plot the coarse grained density for all the ϵ 's; we are aware that it is hard to analyse the plot with the curves being so packed together, therefore we plotted them separately in

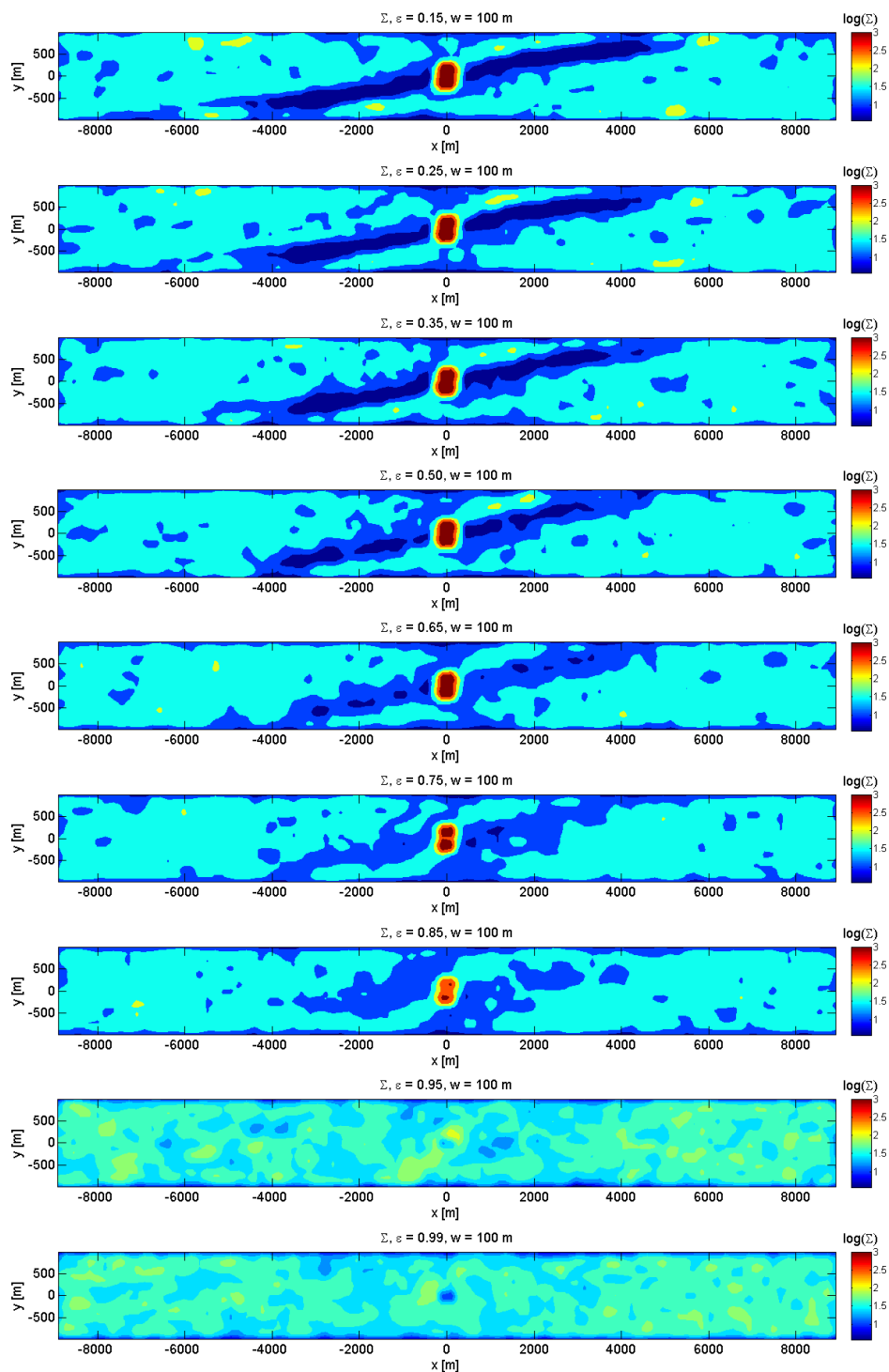


FIGURE 6.4: Coarse grained density Σ of the ring section plotted in a logarithmic scale to enhance the features of the propellers. One can see the gradual blurring of the propeller structure as the the coefficient of restitution increases.

Appendix B Figure B.1. For reference, the red dashed line in Figure 6.5 corresponds to the average density in the unperturbed ring section, i.e., without a moonlet. One feature that is prominent in all of the plots is that the density tends to lower values at the extrema ($y = 1000, -1000$ m), this is due to the periodic boundary condition effects as discussed in Chapter III, section 3.4.

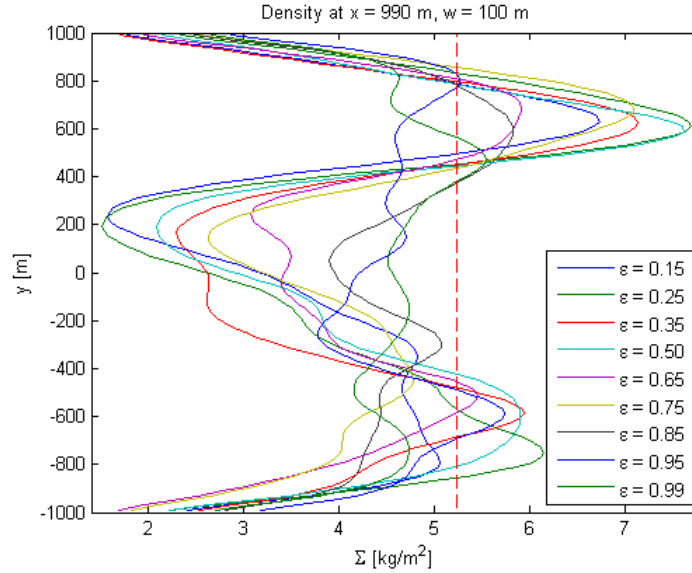


FIGURE 6.5: Coarse grained density of the ring section at $x = 990$ m for different restitution coefficients.

Then, ignoring the density values that are at a distance less than $2w$, we plot in Figure 6.6 (A) the ratio $\Sigma_{max}/\Sigma_{min}$ against the restitution coefficient. The criterion proposed is seen in dashed lines, where points above it show a propeller structure and the ones below it do not. The trend of the ratio is decreasing with increasing ϵ as expected, but also the transition between propeller and no-propeller seems to be smooth, showing no critical ϵ at which the propeller structures abruptly disappear. The error bars correspond to the error associated to the homogeneous-most case, $\epsilon = 0.99$, where the effect of the moonlet is practically invisible; the simulations with the other restitution coefficients have the same error intrinsically. Considering this, we notice that it would be easy for cases when $\epsilon \in [0.70, 0.90]$ to jump between propeller and no-propeller by just changing the initial conditions slightly or averaging over a different time. In order to improve the level of confidence and know more precisely the ϵ at which the no-propeller state is presented, it would be necessary to run several simulations changing the initial conditions, or, if the propellers were developed completely, one could average over different times in order to make statistics and reduce the error bars.

In Figure 6.6 (B) we see the same ratio $\Sigma_{max}/\Sigma_{min}$ but now plotted against the inelasticity $1 - \epsilon^2$. The energy density dissipation rate I is proportional to this factor, $I \propto 1 - \epsilon^2$. We notice that when $\Sigma_{max}/\Sigma_{min} = 2$, which is around $\epsilon \sim 0.70$, this factor is $1 - \epsilon^2 \approx 1/2$. Then, simulations with $1 - \epsilon^2 > 1/2$ tend to show propeller structures and simulations with $1 - \epsilon^2 < 1/2$ will not. The colors just help us to associate both plots to their corresponding ϵ .

One can also think of a criterion comparing velocities instead of densities. Following

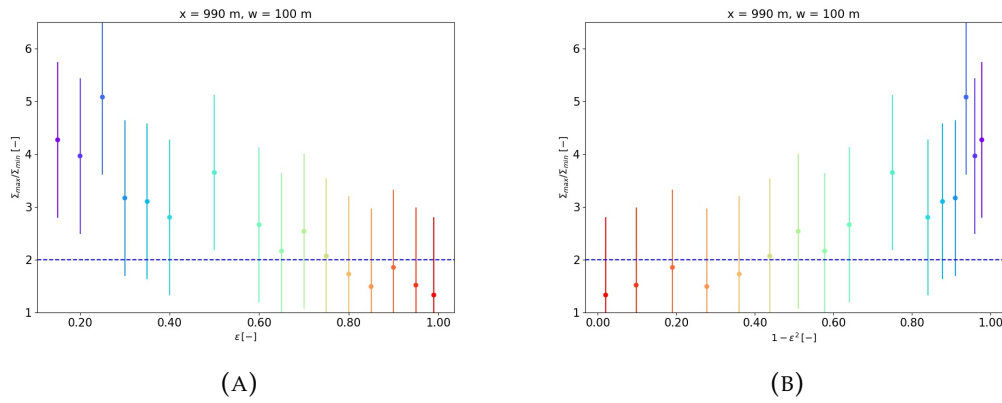


FIGURE 6.6: One can see in figure (A) the ratio of the maximum over the minimum density $\Sigma_{max}/\Sigma_{min}$ against the restitution coefficient ϵ ; in figure (B) the ratio is plotted against the inelasticity $1 - \epsilon^2$. The colors help to associate the data from the same restitution coefficient. The error bars correspond to the error associated to the homogeneous-most case $\epsilon = 0.99$, intrinsic to all ϵ 's.

the work done by Salo [43], we propose that a propeller structure is present when the Hill velocity, given by $v_H = h\Omega_0 = 0.035$ m/s, is higher than the radial velocity dispersion, which in our case can be translated to δv_y . The Hill velocity is a typical velocity due to scattering by the moonlet, so with this criterion we are comparing the thermal velocity with the one induced by an embedded body in the rings. We do not know the exact value for δv_y , nevertheless, we can approximate its saturation value for homogeneous systems without a moonlet using $\delta v_y \approx \sqrt{T_f/m}$, assuming that $\delta v_y = \delta v_x$ and where T_f is the final temperature computed using equation A.21.

We plot this new criterion for the presence of propellers, $v_H > \delta v_y$, in Figure 6.7, where the blue region shows the values of the restitution coefficient where a propeller structure is seen. The upper limit of this region is given by $\epsilon \approx 0.62$, which is similar to the one obtained by comparing densities. We did not write this result as a strict equality due to the assumptions made on δv_y . However, this criterion has the advantage that it can be applied to all densities as long as δv_y is approximated using equation A.21, assuming that the temperature of an homogeneous system is similar to a perturbed system with a moonlet, as it is shown in Appendix A, and assuming that the value of the velocity fluctuation in x and y directions are equal. At larger ϵ 's the granular temperature is big enough to randomize the propellers such that they are not present any more.

Ultimately, we would like to discuss the special cases when $\epsilon = 0.95$ and 0.99 , where we clearly see in Figure 6.4 a big difference in density from all the other cases. There is no visible structure and almost no remnant of the existence of a propeller due to heating by the Lees-Edwards boundaries shear. In fact, the saturation time of the granular temperature in a weakly dissipative system can not be reached within one orbital period of integration, such as with these coefficients of restitution, as discussed in Appendix A.

The simulations provide us with values of the particles velocity throughout the integration, which can be subsequently coarse grained, as done for the density, to obtain a continuum field easier to analyse. When we plot the coarse grained velocity in the

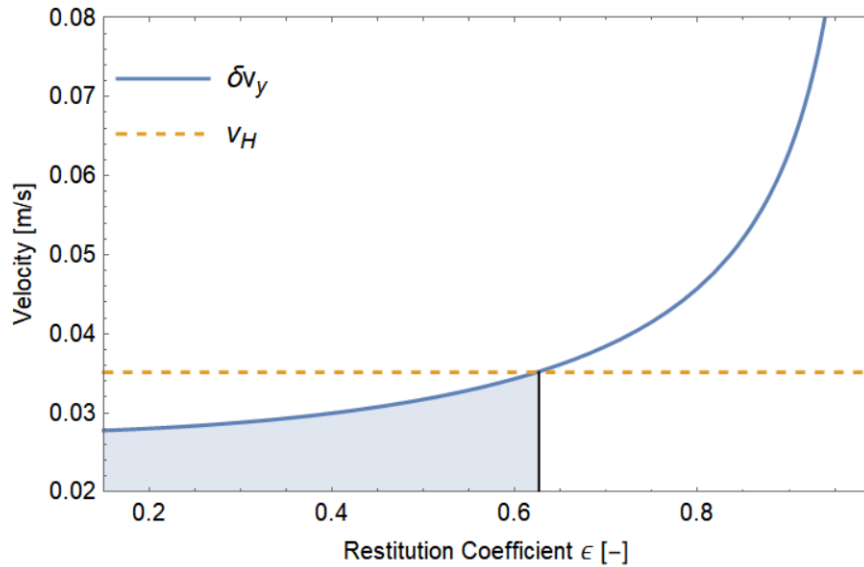


FIGURE 6.7: Velocity fluctuation in the x direction δv_x compared to the Hill velocity v_H . The region in blue shows the values of ϵ where a propeller structure is present.

x direction v_x , for each restitution coefficient, shown in Appendix B Figure B.2, we obtain a constant shear profile similar to that in Figure 6.2. The gravitational effect of the moonlet is barely visible in the middle of the domain and practically invisible for $\epsilon = 0.99$.

It is more instructive to look at the coarse grained velocity fluctuation. The magnitude of the velocity fluctuation is given by

$$\delta v = \sqrt{(\delta v_x)^2 + (\delta v_y)^2}. \quad (6.7)$$

We can see in Figure 6.8 the total velocity fluctuation δv on top, and the velocity fluctuation components δv_x and δv_y in the middle and bottom panels respectively for the case when $\epsilon = 0.15$, since these are the sharpest images; their respective counterparts for the other restitution coefficients are shown in Appendix B.

A large portion of the δv field is blue, meaning that there is little fluctuation in those areas with respect to the shear flow shown in Figure B.2. Naturally, the effect of the moonlet is most visible just around it and following the propeller structure, with the highest fluctuation velocities near the Lagrangian points once again. We have mentioned a couple of times that propellers and gaps in the rings are formed due to gravitational scattering and direct collision with the moonlet; the problem of classical scattering due to a massive body has been known for many years now, and it is addressed in every good book of theoretical classical mechanics [26, 27, 28]. For us, it is not important to compute the trajectory of each individual particle, since collisions with the others make it practically impossible to predict. We are interested in the collective macroscopic field, but that does not mean that we cannot give a qualitative description of how propellers are formed.

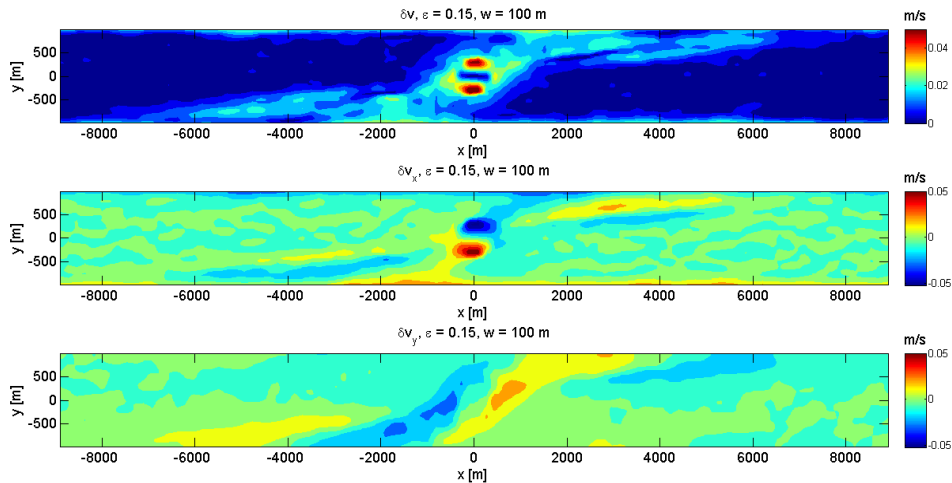


FIGURE 6.8: From top to bottom we see the magnitude of the total coarse grained fluctuation velocity, the fluctuation velocity in x and in the y direction for the case when $\epsilon = 0.15$.

Rein & Papaloizou [13] made a schematic image, shown in Figure 6.9, that will help us explain the formation of these structures. In the middle we see the moonlet (not in scale) surrounded by ring particles gravitationally bounded inside the Roche lobe. Rein & Papaloizou suggest five different types of trajectories, particles can (a) fly by the moonlet without being considerably affected by its gravity and orbiting in a circular motion, (b) collide with the particles inside the Roche lobe and either bounce off or get themselves stuck in there, (c) collide with the moonlet directly, from where they can bounce or roll into the Roche lobe, (d) orbit in what it is called a Horseshoe orbit, or (e) leave the vicinity of the moonlet due to any collision or wiggling inside the Roche lobe that might kick them out.

From our point of view, all the types of orbits look natural, except for one, the horseshoe orbits. For a reader that has no experience in astrodynamics, they can be counterintuitive because particles seem to change the direction of orbital rotation. In reality this is not true, they appear to do so since we are looking from a non-inertial reference frame. The particles in horseshoe orbits co-rotate with the moonlet and all the others; nevertheless, when they accelerate along its orbit due to the presence of another body, they move outwards from Saturn into a larger orbital radius. On the other hand, when they decelerate, the orbital radius decreases [42].

Keeping in mind these five types of trajectories it is now easy to explain Figure 6.8. The spots where the fluctuation velocity is higher near the Lagrangian points are due to particles inside the Roche lobe. In the reference frame of the moonlet they are static, therefore highly deviating from the shear velocity.

In the three images of Figure 6.8, we see formations that follow the shape of the *blades* of the propeller. These are formed when particles in horseshoe orbits collide with particles that just left the Roche lobe and the ones in circular orbit, trajectories labelled (d), (e) and (a) respectively. In Figures B.3, B.4 and B.5 we show the respective velocity fluctuations for the different restitution coefficients. The images in each Figure resembles one another, except for the cases when $\epsilon = 0.95$ and 0.99 , where the granular temperature is so high that it destroys every formation. However, we are certain that it is still a shear flow as seen from Figure B.2.

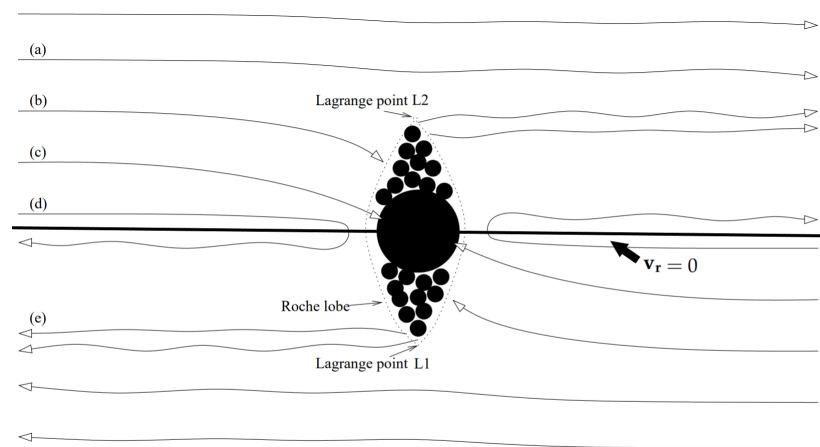


FIGURE 6.9: Schematic trajectories of ring particles in the reference frame of the moonlet. Particles accumulate inside the Roche lobe. Particles on trajectories labelled (a) are on circular orbits. Particles on trajectories labelled (b) collide with other particles in the moonlet's vicinity. Particles on trajectories labelled (c) collide with the moonlet directly. Particles on trajectories labelled (d) are on horseshoe orbits. Particles on trajectories labelled (e) leave the vicinity of the moonlet.

Image taken from [13].

Chapter 7

Clogging in a Constricted Suspension Flow

In parallel to the *propeller project*, I worked with professor Álvaro Marín in what I call the *clogging project*. He and his post-doc, Mathieu Souzy, have performed multiple experiments in order to investigate the clogging phenomenon in a constricted suspension flow inside a micro-channel [44, 45]. Interestingly, the clogging behaviour was found to be qualitatively similar to that of dry granular systems, as in an hour-glass or a hopper. Our purpose is to replicate the clogging phenomenon in micro-channels using DEM simulations.

Studying clogging in a micro-channel is relevant to understand the obstruction mechanism in blood capillaries for example. But clogs do not only occur in biological tissue, but everywhere in our daily life: when you are seasoning your food using the salt shaker and it suddenly stops due to a little salt clog; when you try to get in the train during rush hour but people also try to get out (those who have lived in big cities can relate); or in traffic jams because of the huge number of cars in small streets (again people from big cities will understand). We see that in all these situations, the main ingredients for clogging are a constriction and a sufficient amount of *some material*.

In a more industrial example, clogging is a common issue when designing silos and hoppers, and can happen when stable arches of falling grains form at the outlet of a silo [46]. If the aperture of the silo is much bigger than the typical diameter of the particles, stable arches are very unlikely to form and the material falls uninterrupted; in this continuous situation, the mass rate of the discharged grains is well described by the empirical Beverloo equation [47].

The problem of clogging in silos has been well studied by many researchers [48, 49]. By doing experiments either varying the width of the outlet constriction D or the particle diameter d , one can explore the values of the ratio D/d where the flow is no longer continuous and clogs, which was found to be $D/d \sim 5$. Around this value it is also possible to encounter intermittent flow, where temporal clogs are formed and then destroyed by a sufficiently strong perturbation. Similar behaviours were found when tilting the hopper [50] as well as by submerging it into water [51] to investigate the effect of a tilting angle and interstitial fluid in the clogging mechanism respectively. The studies show that the ratio D/d is in fact the most important parameter to describe the behaviour of clogging, besides the interaction forces between particles.

We mentioned as an everyday example that clogging occurs when people are trying to enter or exit from a place, like the subway; interestingly, it is also found in crowd swarming, when one tries to evacuate a building in an emergency situation, and in sheep herds rushing through a gate to obtain food. Zuriguel et al. [52], investigated crowd swarming, sheep herds, granular materials and colloids, and found that the probability distribution of time lapses between the passages of consecutive bodies exhibits a power-law tail with an exponent that depends on the system condition.

As D/d approaches 1, it is found that the probability of a clogging event occurring increases for any system [53], in theory becoming certain when $D/d < 1$ for hard particles. When performing many experiments far from the intermittent regime ($D/d < 5$), a simple histogram of the number of particles that escape the constriction before the clog occurs is well fitted by an exponential distribution, which is characteristic of a Poisson process, meaning that consecutive clogging events are statistically independent of one another and each of them has a constant probability of occurrence for a given D/d .

A great advantage of doing simulations is that we can easily explore different values of D/d for as many repetitions as time allows in order to obtain good statistics. Our approach is simple, in order to simulate the clogging of particles flowing through a micro-channel with a constriction we need to know, first of all, the forces involved in the system, i.e., the driving force that moves the particles across the channel and the contact forces between particles.

For the contact force, we can use the linear contact model described in Chapter II and for the driving force, we need an expression for the drag felt by the particles due to the fluid; later in this chapter we will discuss whether to use the Drag equation or the Stokes drag. Regardless of which one we use, we also need to know the value of the fluid velocity at each point inside the channel.

7.1 Constricted Suspension Flow

In this section we will develop the basic theory needed to simulate the clogging of particles inside a micro-channel with a bottleneck. For this, we will assume that all the particles are identical and have a diameter d and radius a , the micro-channel has a rectangular cross section of height $h = D$ and width $w = 4D$, where D is the width of the bottleneck, with $d < D$; the length of the channel is considerably bigger in magnitude than the height and width, see Figure 7.1.

Inside the channel there is a flowing liquid that drags the particles which form clogs randomly at the neck; the liquid has a density ρ and viscosity η . Such a system has been researched experimentally by Alvaro Marin et al., [44], where they studied particles of different diameters to vary the neck-to-particle size ratio D/d , finding that the statistics of the clogging events are Poissonian as explained in the last subsection.

Following their experiments, we chose to simulate particles with a diameter between $98 \mu\text{m}$ and $53 \mu\text{m}$, a neck of $D = 100 \mu\text{m}$ and a 135° angle contraction that opens back up into a 120° angle expansion. The density of the liquid is $\rho = 1050 \text{ kg/m}^3$ and its viscosity $\eta = 1.8 \text{ mPa s}$; the density of the particles matches the one of the liquid so that gravitational effects can be neglected.

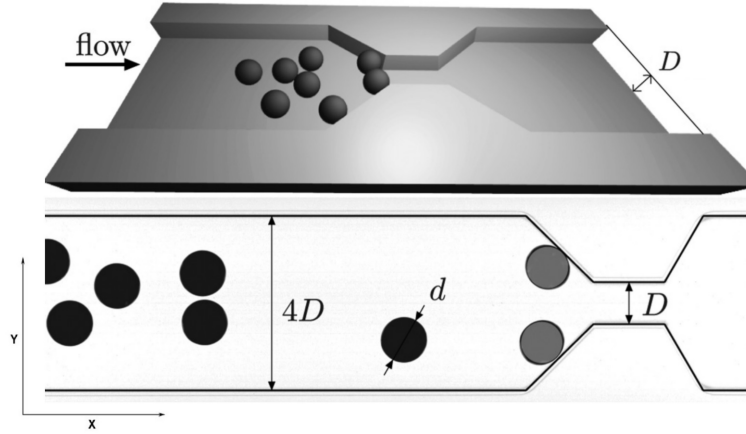


FIGURE 7.1: Diagram of the micro-channel with a width of 4 times the size of the neck D . Particles with diameter d follow the flow driven by a drag force and eventually clog by forming a force arch at the beginning of the neck. Image taken from Marin et al. [44].

In section 7.1.1 we will follow the derivation for the velocity profile in a channel with rectangular cross section, as done by Henrik Bruus in his book *Theoretical Microfluidics* [54]; the manuscript encompasses many and varied problems, but the summary in section 7.1.1 will suffice to obtain an expression for the velocity far away from the constriction. In section 7.1.2 we solve numerically the flow near and inside the constriction. Finally, in section 7.2 we will derive and discuss which drag force expression is more convenient to our system. An excellent book to learn more about hydrodynamics and the drag force is *Fluid Mechanics* by Kundu et al. [55].

7.1.1 Poiseuille Flow Far from the Neck

As stated by Bruus [54], the type of flow that one can find in a lab-on-a-chip micro-channel is a Poiseuille Flow; they have the characteristic that are pressure-driven and in a steady state. If we suppose that the channel is infinite (or very long in comparison to the particles inside it), with constant cross section in the yz -plane and parallel to the x axis, there would be translational invariance with respect to that axis no matter its cross sectional shape.

Given the symmetry of the problem, the forces would vanish in the yz -plane; the velocity would be independent of x due to its translational invariance in the x direction but the only non-zero component of the velocity is along that same axis.

The equation that describes the motion of a liquid inside a channel is the Navier-Stokes equation for incompressible fluids

$$\rho [\partial_t \mathbf{v} + (\mathbf{v} \cdot \nabla) \mathbf{v}] = -\nabla p' + \eta \nabla^2 \mathbf{v} + \rho \mathbf{g}, \quad (7.1)$$

where \mathbf{v} is the velocity vector field, ρ represents the density of the fluid, η its dynamic viscosity, p' the pressure and \mathbf{g} any body forces, in this case, gravity.

Equation (7.1) is difficult to solve analytically, but with the afore mentioned assumptions we can simplify it considerably. The steady state condition tells us that $\partial_t \mathbf{v} = 0$.

By symmetry, the only non-zero component of the velocity field is in the x direction but independent of x , $\mathbf{v} = v_x(y, z)\hat{e}_x$. As a consequence, the non-linear term in (7.1) cancels out, $(\mathbf{v} \cdot \nabla)\mathbf{v} = 0$.

Moreover, we can define the pressure as

$$p' = p + \rho g z, \quad (7.2)$$

such that its hydrostatic part $\rho g z$ cancels the gravitational body force $\rho \mathbf{g}$; p is called auxiliary pressure, but we will refer to it as simply the pressure.

After all these considerations we can rewrite what is left of equation (7.1)

$$0 = -\nabla p + \eta \nabla^2 [v_x(y, z)\hat{e}_x], \quad (7.3)$$

furthermore, if a constant pressure difference Δp is applied over a segment of length L of the channel, we can write the gradient as

$$\nabla p = -\frac{\Delta p}{L}, \quad (7.4)$$

such that Δp is a positive quantity and the gradient is negative (the liquid flows from high pressure to low pressure).

The channel we want to simulate has rectangular cross section with its width running from $-\frac{1}{2}w$ to $\frac{1}{2}w$ in the y axis, and a height from 0 to h in the z axis, as seen in Figure 7.2,

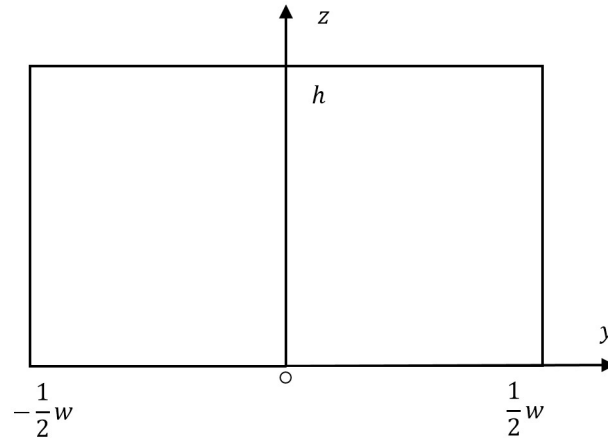


FIGURE 7.2: Rectangular cross section of the channel with a height h and width w .

thus the problem we need to solve is:

$$\begin{aligned} \left[\partial_y^2 + \partial_z^2 \right] v_x(y, z) &= -\frac{\Delta p}{\eta L}, \\ \text{for } -\frac{1}{2}w < y < \frac{1}{2}w, \\ &0 < z < h. \end{aligned} \quad (7.5)$$

Equation (7.5) is a second order partial differential equation in 2D, therefore we need four conditions to solve it uniquely. In this case, we have the *no-slip* conditions at the walls of the channel, meaning, the velocity is zero at the walls

$$\begin{aligned} v_x(y, z) &= 0, \\ \text{for } y &= \pm \frac{1}{2}w, \\ z &= 0, z = h. \end{aligned} \quad (7.6)$$

The method by which we will solve (7.5) is called eigenfunction expansion [54, 56], if the reader is interested in knowing more about this method, I recommend the book *Applied Partial Differential Equations* of Richard Haberman [56].

We start by expanding the functions in (7.5) as Fourier series along the z direction. To ensure the conditions $v_x(y, 0) = v_x(y, h) = 0$, we expand only in Fourier sine series with terms proportional to $\sin\left(n\pi\frac{z}{h}\right)$ and $n \in \mathbb{N}$. If we were to use the full Fourier series, we would have found that the terms proportional to the cosine cancel out due to the boundary conditions.

For the constant term $-\frac{\Delta p}{\eta L}$ in (7.5), the expansion is given by

$$-\frac{\Delta p}{\eta L} = -\frac{\Delta p}{\eta L} \frac{4}{\pi} \sum_{n, \text{odd}}^{\infty} \frac{1}{n} \sin\left(n\pi\frac{z}{h}\right). \quad (7.7)$$

The velocity v_x is a function of y and z ; we expand in Fourier sine series along z and leave the y dependent part as an undetermined function $f_n(y)$

$$v_x(y, z) = \sum_{n=1}^{\infty} f_n(y) \sin\left(n\pi\frac{z}{h}\right), \quad (7.8)$$

then, when we insert this ansatz into the left hand side of (7.5) we obtain

$$\left[\partial_y^2 + \partial_z^2 \right] v_x(y, z) = \sum_{n=1}^{\infty} \left[f_n''(y) - \frac{n^2\pi^2}{h^2} f_n(y) \right] \sin\left(n\pi\frac{z}{h}\right). \quad (7.9)$$

Each term at the right hand side of equations (7.7) and (7.9) must be equal since any two sine functions $\sin\left(n\pi\frac{z}{h}\right)$ and $\sin\left(m\pi\frac{z}{h}\right)$ are linearly independent $\forall n \neq m$. To achieve this

$$f_n(y) = 0, \text{ for } n \text{ even} \quad (7.10)$$

so all even terms of (7.9) cancel out. And the odd terms of both sizes must be equal

$$f_n''(y) - \frac{n^2\pi^2}{h^2} f_n(y) = -\frac{\Delta p}{\eta L} \frac{4}{\pi n}, \text{ for } n \text{ odd.} \quad (7.11)$$

We reduced the second order partial differential equation in 2D to a second order ordinary differential equation in one dimension. If we solve (7.11) we have solved our problem. A general solution of (7.11) can be expressed as

$$f_n(y) = f_n^{inhom}(y) + f_n^{homog}(y), \quad (7.12)$$

where $f_n^{inhom}(y)$ is a particular solution of the inhomogeneous equation and $f_n^{homog}(y)$ is a general solution of the homogeneous equation. By inspection

$$f_n^{inhom}(y) = \frac{4h^2 \Delta p}{\pi^3 \eta L} \frac{1}{n^3}, \text{ for } n \text{ odd.} \quad (7.13)$$

In order to solve the homogeneous equation

$$f_n''(y) - \frac{n^2\pi^2}{h^2} f_n(y) = 0, \quad (7.14)$$

we follow standard methods and propose a solution of the form

$$f_n^{homog}(y) = A \cosh\left(\frac{n\pi}{h}y\right) + B \sinh\left(\frac{n\pi}{h}y\right), \quad (7.15)$$

with A and B constants of integration. Adding the inhomogeneous (7.13) and homogeneous (7.15) solutions and employing the boundary conditions (7.6) we arrive to an expression for $f_n(y)$

$$f_n(y) = \frac{4h^2 \Delta p}{\pi^3 \eta L} \frac{1}{n^3} \left[1 - \frac{\cosh\left(n\pi \frac{y}{h}\right)}{\cosh\left(n\pi \frac{w}{2h}\right)} \right], \text{ for } n \text{ odd.} \quad (7.16)$$

inserting (7.16) into (7.8) we get the solution for the x component of the velocity inside the channel

$$v_x(y, z) = \frac{4h^2 \Delta p}{\pi^3 \eta L} \sum_{n, odd} \frac{1}{n^3} \left[1 - \frac{\cosh\left(n\pi \frac{y}{h}\right)}{\cosh\left(n\pi \frac{w}{2h}\right)} \right] \sin\left(n\pi \frac{z}{h}\right). \quad (7.17)$$

As you may notice, the solution is not straightforward to attain, but due to the symmetry, this is the only non-zero component of the velocity. All the parameters in (7.17) are given, except for one, the pressure difference Δp . Alvaro Marin and Mathieu Souzy have made experiments with rectangular micro-channels and in particular

with the same flow-controlled set-up we are trying to simulate [44, 45]; in this kind of experiment, the inlet and outlet flow rates are kept constant making the pressure drop dependent on the average velocity. I was able to talk to Alvaro in person so he could provide us with a typical measurement for the average velocity

$$\bar{v}_x \approx 15 d/s, \quad (7.18)$$

given in diameters of particle d per second.

In order to obtain Δp we need to compute analytically the average of v_x and equate it with (7.18); the process of averaging (7.17) correctly is tricky, fortunately Bruus [54] did most of the calculations, which we present hereunder.

We start by computing the flow rate Q that is just the integral of v_x over the cross sectional area

$$\begin{aligned} Q &= 2 \int_0^{w/2} dy \int_0^h dz v_x(y, z) \\ &= \frac{4h^2 \Delta p}{\pi^3 \eta L} \sum_{n, \text{odd}} \frac{1}{n^3} \frac{2h}{n\pi} \left[w - \frac{2h}{n\pi} \tanh \left(n\pi \frac{w}{2h} \right) \right] \\ &= \frac{8h^3 w \Delta p}{\pi^4 \eta L} \sum_{n, \text{odd}} \left[\frac{1}{n^4} - \frac{2h}{\pi w} \frac{1}{n^5} \tanh \left(n\pi \frac{w}{2h} \right) \right] \\ &= \frac{h^3 w \Delta p}{12\eta L} \left[1 - \sum_{n, \text{odd}} \frac{1}{n^5} \frac{192}{\pi^5} \frac{h}{w} \tanh \left(n\pi \frac{w}{2h} \right) \right], \end{aligned} \quad (7.19)$$

where in the last step we used the relation $\sum_{n, \text{odd}} \frac{1}{n^4} = \frac{\pi^4}{96}$. Now, the hyperbolic tangent has a very convenient property, it goes to 1 pretty quickly. In the geometry of the channel we want to simulate $w = 4h$, that means that even when $n = 1$ the hyperbolic tangent becomes $\tanh(2\pi) = 0.99999$. Then, it is reasonable to make the approximation $\frac{h}{w} \tanh \left(n\pi \frac{w}{2h} \right) \approx \frac{h}{w}$, so that inserting in equation (7.19)

$$\begin{aligned} Q &\approx \frac{h^3 w \Delta p}{12\eta L} \left[1 - \frac{192}{\pi^5} \frac{h}{w} \sum_{n, \text{odd}} \frac{1}{n^5} \right] \\ &= \frac{h^3 w \Delta p}{12\eta L} \left[1 - \frac{192}{\pi^5} \frac{h}{w} \frac{31}{32} \zeta(5) \right] \\ &\approx \frac{h^3 w \Delta p}{12\eta L} \left[1 - 0.63 \frac{h}{w} \right], \quad h < w, \end{aligned} \quad (7.20)$$

where we made use of the Riemann zeta function, $\zeta(x) = \sum_{n=1}^{\infty} \frac{1}{n^x}$, and the following property for n odd and $x = 5$

$$\sum_{n, \text{odd}} \frac{1}{n^5} = \sum_{n=1}^{\infty} \frac{1}{n^5} - \sum_{n, \text{even}} \frac{1}{n^5} = \zeta(5) - \sum_{k=1}^{\infty} \frac{1}{(2k)^5} = \zeta(5) - \frac{1}{32} \zeta(5) = \frac{31}{32} \zeta(5).$$

The approximations done to obtain Q are really good, even for the worst case scenario, $h = w$, the error in the flow rate is just 13%. Now that the tricky calculations are done, we proceed to compute the average velocity by just dividing the flow rate by the cross sectional area

$$\bar{v}_x = \frac{Q}{A} \approx \frac{\frac{h^3 w \Delta p}{12 \eta L} \left[1 - 0.63 \frac{h}{w} \right]}{hw}, \quad (7.21)$$

so after solving for Δp we obtain a nice expression in terms of the geometry of the system and the fluid properties valid for any value of h and w

$$\Delta p \approx \frac{12 \eta L \bar{v}_x}{h^2 \left[1 - 0.63 \frac{h}{w} \right]}. \quad (7.22)$$

7.1.2 Poiseuille Flow Near and Inside the Neck

Solving Navier-Stokes equation even for a channel with such a high symmetry as our case, is not straightforward, not to mention that there is no analytical solution for the flow velocity along the channel including the neck. Therefore, we make use of the software called COMSOL Multiphysics[®], which is a general purpose simulation software for engineering and science, to solve numerically the velocity near and inside the neck. The platform can be used for research in the areas of electromagnetics, structural mechanics, acoustics, fluid flow, heat transfer, and chemical engineering. More information about COMSOL in the official website <https://www.comsol.com>.

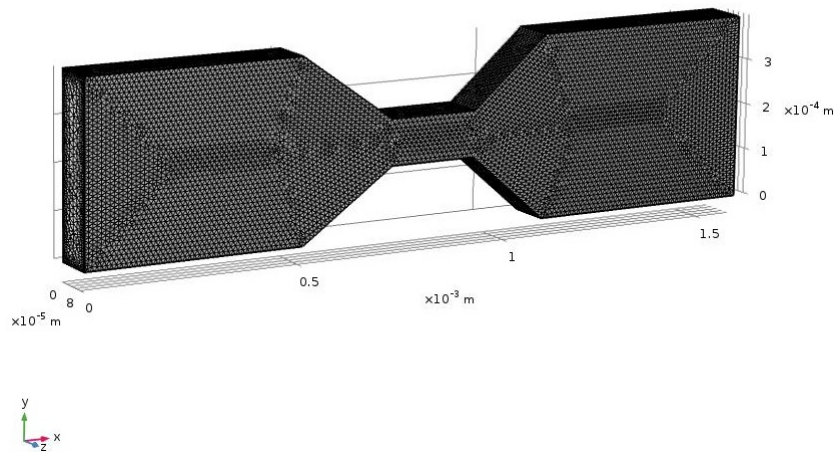


FIGURE 7.3: Mesh of the rectangular channel near the neck.

We start by building a mesh in the channel with the geometry of our system, as seen in Figure 7.3. The solution is approximated through the Finite Element Method, which discretizes the domain, meaning, breaking it into smaller discrete parts called elements, and then stitching the solution of each element together to form a piecewise global function.

As a matter of ease, the origin of coordinates is positioned in the lower left corner of the prism; in the MercuryDPM simulations it is easier to place the origin in the middle of the neck, but we can easily do a translation of coordinates for compatibility.

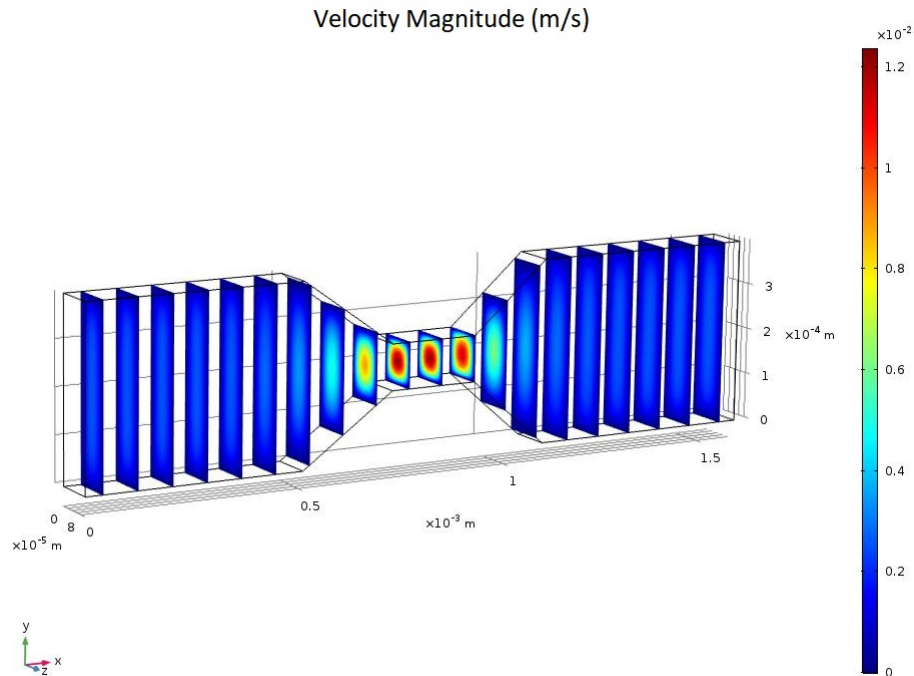


FIGURE 7.4: Transversal slices in the plane yz showing with a color map the magnitude of the velocity inside the channel.

The equation to solve is (7.1) in the absence of gravity and in steady state, with the no-slip conditions at the walls. The parameters that need to be specified are the viscosity and density of the fluid, and the average inlet and outlet flow velocity, which was set to $\bar{v}_x = 15 d/s$, with $d = 98 \mu\text{m}$ for all the simulations even with different particle diameters.

In Figure 7.4 we can see many transversal slices in the plane yz showing the magnitude of the velocity. The slices that are further away from the neck are similar between each other and show non x dependent behaviour as described by equation (7.17). But, as the flow approaches the neck, the average velocity grows due to the conservation of flow rate, therefore being dependent on the coordinate along the channel.

Since the cross sectional area of the channel is reduced to one fourth of its value inside the neck, the average velocity increases by a factor of four. In the area decreasing sections, to the left and to the right of the center of the neck, the flow velocity gains a component in the y direction. We consider that this component is fundamental in the stability of force bridges between clogging particles, therefore, something we wanted to capture with the numerical results.

In Figure 7.5 we show again the magnitude of the velocity, in this case on one slice in the xy plane. The maximum velocity is naturally at the center of the neck and gradually decreases as we go closer to the walls or the entrance and exit of the neck.

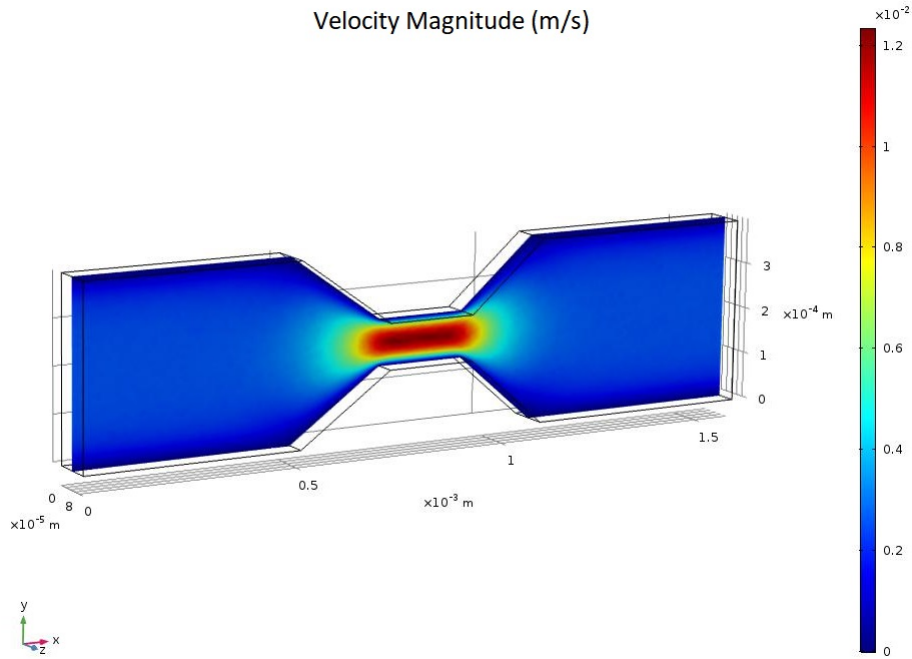


FIGURE 7.5: Slice in the plane xy showing the magnitude of the velocity near the neck region.

7.2 Drag Force

An object that is moving around with velocity \mathbf{u} inside a fluid of velocity \mathbf{v} will feel a drag force that is dependent on the velocity difference $\mathbf{V} = \mathbf{v} - \mathbf{u}$. But we have to be careful which expression for the drag we should use, it could be either the *Drag Equation* [55]

$$\mathbf{F}_D = \frac{1}{2} \rho C_D A |\mathbf{V}|^2 \hat{V}, \quad (7.23)$$

or the *Stokes Drag* [54, 55]

$$\mathbf{F}_S = 6\pi\eta a \mathbf{V}, \quad (7.24)$$

both are widely used and have different origins.

The Drag equation comes completely from dimensional analysis, as it will be shown in Appendix C, section C.1. Assuming that the drag force \mathbf{F}_D on a particle depends on its cross sectional area A , the density of the fluid ρ , its viscosity η and the velocity difference \mathbf{V} , one can find a dimensionless number called the drag coefficient C_D . This dimensionless quantity is identical for dynamically similar flows, it is dependent on the Reynolds number and, naturally, on the shape of the submerged object [55].

On the other hand, the Stokes drag is found by making an approximation for very low Reynolds number ($\text{Re} \ll 1$), when solving the linear Stokes equation to get the velocity and pressure fields, then integrating to obtain the stress tensor at the

surface of the particle and, from it, the force. It is dependent on \mathbf{V} , the viscosity η , the particle radius a and valid only for spherical particles far away from boundaries [54, 55].

It can be shown that the drag equation can be reduced to the Stokes drag for small particle Reynolds number, when $C_D = \frac{24}{\text{Re}_p}$ [57]. The particle Reynolds number is defined as

$$\text{Re}_p = \frac{\rho v d}{\eta}, \quad (7.25)$$

with ρ and η the density and viscosity of the fluid the particle is immersed in, v the particle terminal velocity and d its diameter. For typical values inside the channel, $\rho = 1050 \text{ kg/m}^3$, $\eta = 1.8 \text{ mPa s}$, $d = 98 \mu\text{m}$ and $v = 15 \text{ d/s}$, assuming that the particle terminal velocity is the same as the average of the fluid velocity, we obtain $\text{Re}_p \approx 0.084$, which is considered small Re_p .

On one hand, we cannot assume that the Drag Coefficient is a constant for spherical particles, it depends non-linearly on Re_p and there are many experimental and theoretical expressions to approximate its value at a given particle Reynolds number [57, 58]; on the other hand, the Stokes Drag equation is valid for spherical particles that are far away from others and walls. For the case of constricted suspensions, the force must be modified taking into account the change of the local packing fraction when a clogging event occurs [59]. As we will see in the next subsection, the modified expression of the Stokes drag is simple and easy to implement, which will be the reason why we choose it over the Drag equation.

7.2.1 Stokes Drag

There is no exact solution to the Navier-Stokes equation for incompressible fluids, equation (7.1). But to derive the expression for the Stokes Drag, we make some simplifying assumptions. For the moment being, we consider the flow around a single spherical particle far away from other particles and boundaries, such that the flow is steady and the velocity of the fluid is U far from the particle in question and going in the x direction. In spherical coordinates, we set the radial direction pointing outward from the center of the sphere, the polar angle θ is measured from the x axis, as in Figure 7.6, and the azimuthal angle ϕ lies on the plane perpendicular to the x axis.

We can either assume that the density of the particle matches that of the fluid, as it is for the experimental set up we want to simulate; or we can redefine pressure as in (7.2) to cancel out gravity body forces. Then, the Navier-Stokes equation is reduced to

$$\rho(\mathbf{v} \cdot \nabla)\mathbf{v} = -\nabla p + \eta \nabla^2 \mathbf{v}, \quad (7.26)$$

it is still a non-linear second order differential equation with no analytical solution. If we define the dimensionless variables

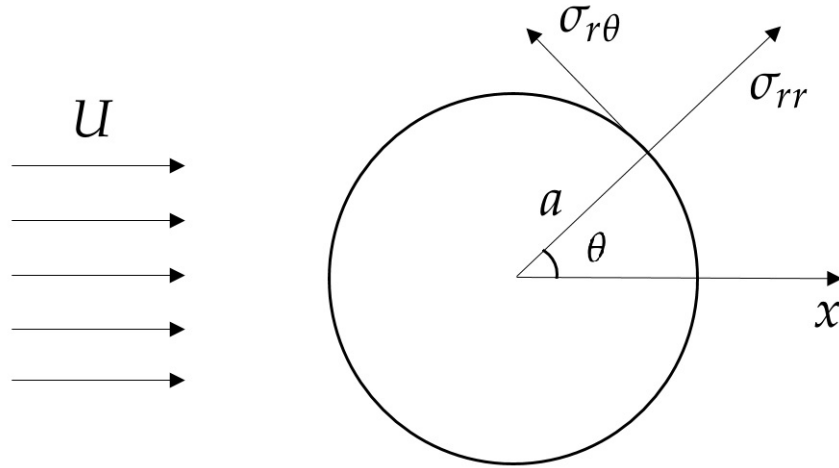


FIGURE 7.6: Creeping flow over a spherical particle of radius a when it is at rest and the flow velocity is U . The viscous stress components at the surface are σ_{rr} and $\sigma_{r\theta}$.

$$\begin{aligned} x_i^* &= x_i/L, \\ v_j^* &= v_j/U, \\ p^* &= (p - p_\infty) \frac{L}{\eta U}, \end{aligned} \quad (7.27)$$

we can recast equation (7.26) in a dimensionless form

$$\text{Re}(\mathbf{v}^* \cdot \nabla^*) \mathbf{v}^* = -\nabla^* p^* + \nabla^{2*} \mathbf{v}^*, \quad (7.28)$$

and balance which terms are more important in the momentum equation. The terms in the right-hand-side of (7.28) are of order unity, but for a low flow speed of viscous fluid going around a small object, the Reynolds number is very small, $\text{Re} \rightarrow 0$; meaning that the term in the left-hand-side of (7.28) can be neglected. These kinds of flows are called creeping flows, which are described by the (now dimensional) equation

$$\eta \nabla^2 \mathbf{v} = \nabla p. \quad (7.29)$$

Solving equation (7.29) in spherical coordinates for the flow around a spherical particle is not straightforward; our main reference books solve it in slightly different ways [54, 55], we will derive the Stokes Drag following half of the derivation made by Kundu and half made by Bruus.

We start by taking the curl of (7.29) to obtain an equation for the vorticity $\boldsymbol{\omega} = \nabla \times \mathbf{v}$

$$\nabla^2 \boldsymbol{\omega} = 0, \quad (7.30)$$

since the curl of a gradient is equal to zero, the right-hand-side gets cancelled out. The full expression for the vorticity in spherical coordinates is long and complicated

$$\boldsymbol{\omega} = \frac{\hat{e}_r}{r \sin \theta} (\partial_\theta (v_\phi \sin \theta) - \partial_\phi v_\phi) + \frac{\hat{e}_\theta}{r \sin \theta} (\partial_\phi v_r - \sin \theta \partial_r (r v_\phi)) + \frac{\hat{e}_\phi}{r} (\partial_r (r v_\theta) - \partial_\theta v_r), \quad (7.31)$$

but thanks to the symmetry of the problem, the only non-zero component of the vorticity is the azimuthal one

$$\omega_\phi = \frac{1}{r} [\partial_r (r v_\theta) - \partial_\theta v_r], \quad (7.32)$$

Furthermore, since the problem is axisymmetric, the r and θ components of the velocity can be found from an axisymmetric stream function ψ

$$\begin{aligned} v_r &= \frac{1}{r^2 \sin \theta} \partial_\theta \psi, \\ v_\theta &= -\frac{1}{r \sin \theta} \partial_r \psi, \end{aligned} \quad (7.33)$$

so that after inserting equations (7.33) into (7.32) we obtain the azimuthal vorticity in terms of the stream function

$$\omega_\phi = -\frac{1}{r} \left[\frac{1}{\sin \theta} \partial_r^2 \psi + \frac{1}{r^2} \partial_\theta \left(\frac{1}{\sin \theta} \partial_\theta \psi \right) \right]. \quad (7.34)$$

With this result we recast (7.30) to obtain an equation for ψ written in operator form

$$\left[\partial_r^2 + \frac{\sin \theta}{r^2} \partial_\theta \left(\frac{1}{\sin \theta} \partial_\theta \right) \right]^2 \psi = 0, \quad (7.35)$$

where the boundary conditions now become

$$\begin{aligned} v_r(r = a) = 0 &\longrightarrow \psi(r = a) = 0 \\ v_\theta(r = a) = 0 &\longrightarrow \partial_r \psi(r = a) = 0 \\ \psi(r \rightarrow \infty) &= \frac{1}{2} U r^2 \sin^2 \theta. \end{aligned} \quad (7.36)$$

The last condition comes from writing the stream function for an uniform flow in spherical coordinates. The solution of (7.35) is given by

$$\psi = U r^2 \sin^2 \theta \left(\frac{1}{2} - \frac{3a}{4r} + \frac{a^3}{4r^3} \right). \quad (7.37)$$

Then, by inserting into (7.33) we arrive at the expressions for the components of the r and θ velocities

$$\begin{aligned} v_r &= U \cos \theta \left(1 - \frac{3a}{2r} + \frac{a^3}{2r^3} \right), \\ v_\theta &= -U \sin \theta \left(1 - \frac{3a}{4r} - \frac{a^3}{4r^3} \right). \end{aligned} \quad (7.38)$$

One can obtain the pressure field by solving (7.29) using the expressions for the velocities

$$p - p_\infty = -\frac{3\eta a U \cos \theta}{2r^2}. \quad (7.39)$$

The drag force acting on the sphere is derived after integrating the x component of the surface force density $\hat{e}_x \cdot (\sigma \cdot \hat{e}_r)$ over the surface of the sphere.

$$F_s = \int_{\partial\Omega} dA \hat{e}_x \cdot (\sigma \cdot \hat{e}_r). \quad (7.40)$$

The total stress tensor

$$\sigma_{ij} = -p\delta_{ij} + \sigma_{ij}^D \quad (7.41)$$

is divided into an isotropic, $-p\delta_{ij}$, and a deviatoric part, σ_{ij}^D , where the deviatoric viscous stresses over the surface of the sphere are given by

$$\begin{aligned} \sigma_{rr}^D &= 2\eta \partial_r v_r, \\ \sigma_{r\theta}^D &= \eta \left(\frac{1}{r} \partial_\theta v_r + \partial_r v_\theta - \frac{1}{r} v_\theta \right). \end{aligned} \quad (7.42)$$

At the surface of the sphere, $r = a$, the pressure and the viscous stresses are simply

$$\begin{aligned} (p - p_\infty)(r = a) &= -\frac{3\eta U \cos \theta}{2a} \\ \sigma_{rr}^D(r = a) &= 0, \\ \sigma_{r\theta}^D(r = a) &= -\frac{3\eta U}{2a} \sin \theta. \end{aligned} \quad (7.43)$$

Then, we can integrate equation (7.40)

$$F_s = \int_{\partial\Omega} dA \hat{e}_x \cdot (\sigma \cdot \hat{e}_r) = \int_0^a r dr \int_{-1}^1 d(\cos \theta) (-p \cos \theta + \sigma_{rr}^D \cos \theta - \sigma_{r\theta}^D \sin \theta), \quad (7.44)$$

to arrive at the drag force in the x direction

$$F_s = 6\pi\eta aU, \quad (7.45)$$

expression that we call *Stokes Drag*, which can be generalized for a 3D case

$$\mathbf{F}_s = 6\pi\eta a(\mathbf{v} - \mathbf{u}) = 6\pi\eta a\mathbf{V}. \quad (7.46)$$

As you may notice, many of the assumptions done for the derivation of the Stokes Drag are unrealistic for a suspension of particles and a clogging event: the particles are not isolated, they might be in contact even before clogging at the neck, and, for such a confined system, the particles are always close to a boundary.

When the particle packing fraction ϕ rises inside the channel, due to clogging for example, the fluid has less empty space to flow through, and, as a consequence of conservation of flow rate, the velocity of the fluid between the particles rises. We see from equation (7.46) that the drag force is proportional to the velocity of the fluid *far* from any particles, then, we must correct the Stokes Drag with a voidage function $f(\phi)$ dependent on the packing fraction, to take into account the increment in the drag force. In the literature [59], one defines a voidage function, $f(\varepsilon)$, in terms of the porosity

$$\varepsilon = 1 - \phi, \quad (7.47)$$

such that when the porosity is reduced, the drag force increases. There are many expressions for $f(\varepsilon)$, but looking at the work done by Beetstra [59], we consider that the expression that best fits our system is $f(\varepsilon) = 2k \frac{(1 - \varepsilon)}{\varepsilon^2}$, with the numerical constant $k = 5.34$; then, the corrected Stokes Drag becomes

$$\mathbf{F}_s = f(\varepsilon)6\pi\eta a\mathbf{V} = 12k \frac{(1 - \varepsilon)}{\varepsilon^2} \pi\eta a\mathbf{V}, \quad (7.48)$$

valid for $\text{Re} \ll 1$ and for systems where the porosity does not tend to 1, i.e., very dilute systems. In the experiments done by Marin [44], the packing fraction inside the micro-channel is between 0.20 and 0.30, and the velocities of the particles always satisfy the low Reynolds number condition imposed on equation (7.48), which also takes into account the rising of the drag force due to a clogging event; therefore, we consider that the corrected Stokes Drag equation (7.48) is appropriate to model our system.

7.3 Summary

In this chapter we solved the Navier-Stokes equation for an infinite channel with rectangular cross section and derived the expression for the only component of the flow velocity

$$v_x(y, z) = \frac{4h^2 \Delta p}{\pi^3 \eta L} \sum_{n, \text{odd}}^{\infty} \frac{1}{n^3} \left[1 - \frac{\cosh\left(n\pi \frac{y}{h}\right)}{\cosh\left(n\pi \frac{w}{2h}\right)} \right] \sin\left(n\pi \frac{z}{h}\right), \quad (7.49)$$

which applies far from the channel neck; we consider that a distance of $4D$ from the center of the neck is good enough to be able to use equation (7.49). All the parameters are given except for the pressure difference Δp , in order to obtain it, we compute the flow rate in terms of a measurable parameter, the average velocity \bar{v}_x , so that after solving we get

$$\Delta p \approx \frac{12\eta L \bar{v}_x}{h^2 \left[1 - 0.63 \frac{h}{w} \right]}. \quad (7.50)$$

The flow near and inside the channel neck was obtained using the software called COMSOL, that gives us numerical results for the x and y components of the velocity. It is advisable to just use the numerical solutions at the neck and nearby because it is more expensive computationally speaking than the exact velocity result throughout the whole channel.

Finally, after a long discussion, we considered that the most accurate expression for the drag force that a particle inside the channel feels is

$$\mathbf{F}_s = 12k \frac{(1 - \varepsilon)}{\varepsilon^2} \pi \eta a \mathbf{V}, \quad (7.51)$$

equation (7.51) takes into account the presence of other particles and the increase of the drag force at a clogging event.

Chapter 8

Simulations of Clogging in a Constricted Suspension Flow

In the previous chapter, we went through a long discussion of the theoretical tools required to simulate a constricted suspension flow. In this chapter we are going to show and discuss the main results of the clogging simulations. Here, we will apply the derived equations, analyse the results and show the advantages and disadvantages of our approach.

8.1 Simulations Setup

Using the MercuryDPM framework, we insert particles of the same diameter d in a channel like the one described in section 7.1. We insert them randomly at the left side of the channel, so that the particles flow from left to right, at a distance of $15D$ from the center of the constriction and at a rate such that the particle volume fraction is kept at $\phi = 0.20$ along the channel before a clogging event.

The driving force is given by the modified Stokes drag, equation (7.51). Where the value of the flow velocity is obtained from equation (7.49) at a distance further than $4D$ away from the center of the constriction, and from the COMSOL numerical results at a distance closer than the aforementioned value, as explained in section 7.1.

When the particles come into contact with each other or with the walls of the micro-channel, they feel a force given by the linear contact model described in section 2.3. Unlike the propeller simulations of Chapter VI, these particles have non-zero friction coefficients, since we consider that friction is a mechanism that helps in the formation and stability of arches at the bottleneck.

It is a good moment to discuss the pros and contras of the approach followed. Using MercuryDPM, it is very simple to vary the size of the particles inserted (or the size of the constriction for that matter) in order to investigate different values of D/d . The static and dynamic friction coefficients are input parameters that we can also explore to see the effect of friction in the statistics of clogging; however, this can lead to complications if we want to tune both parameters to experimental results where the friction is unknown.

A big approximation done is the assumption that the flow is unaffected by the particles immersed in it, which is naturally not true. In reality, the fluid velocity field will deviate from the Poiseuille profile the more particles are inserted, not to mention at a

clogging event. In order to solve the velocity field accurately, a CFD solver (Computational Fluid Dynamics) should be coupled with MercuryDPM, which is in practice complicated and expensive computationally speaking. In that sense, our approach is much faster, being able to run 1000 simulations in a matter of hours, depending on the particle size.

We try to capture the physics using a Poiseuille flow, since it reproduces the behaviour of the particles inside the channel. Being their velocity lower the closer to the walls; and making up for the lack of accuracy in the flow by using the modified Stokes drag.

The particle diameters are chosen to be in the range $d \in [53, 98] \mu\text{m}$, fixing the constriction width at $D = 100 \mu\text{m}$ as described in section 7.1. The static and dynamic friction coefficients were set to $\mu_s = \mu_d = 0.5$. In order to calculate the drag force, as in equation (7.51), the local volume fraction is needed (or, equivalently, the porosity); we compute it by employing a coarse graining approach as described in Chapter III, with a coarse graining width of $100 \mu\text{m}$.

We let the simulations run until the local volume fraction at the neck remained the same for a sufficiently long time. In practice, this time is set to 1 second of simulation, since this is approximately the minimum time that a particle takes to travel the distance from the insertion point to the constriction. In this range of particle sizes, the clogs are permanent and the time at which the simulation should be stopped is arbitrary. However, when reducing even further the particle diameter, one has to be careful how to define a clogged state since temporal clogs can occur. Some authors define it in multiples of the time a particle takes to move the length of its own diameter [60], but an exact number is not established.

The number of particles s that escaped the constriction before the clog occurs is counted for all simulations. A total of one thousand simulations were done for each particle diameter, changing the random seed of MercuryDPM every time to obtain different values of s in each experiment and, from it, the mean number of escapees $\langle s \rangle$. The events where s is higher than $5 \langle s \rangle$ are very rare cases and they were removed in order to get more representative statistics.

In Figure 8.1 we show two exemplary clogging events for the cases when $D/d = 1.88$ and 1.02 , which are the two limiting cases in our simulation sample.

8.2 Results and Statistics of Clogging in a Constricted Suspension Flow

In Figure 8.2 (A), we plot the normalized histogram of escaped particles s for the representative example $D/d = 1.02$; the size of the bins was assigned according to the Scott's normal reference rule. The number N of events observed decreases for increasing s ; in Chapter VII, we mentioned that the histogram can be fitted by an exponential distribution

$$N = \frac{1}{\langle s \rangle} e^{-s/\langle s \rangle}, \quad (8.1)$$

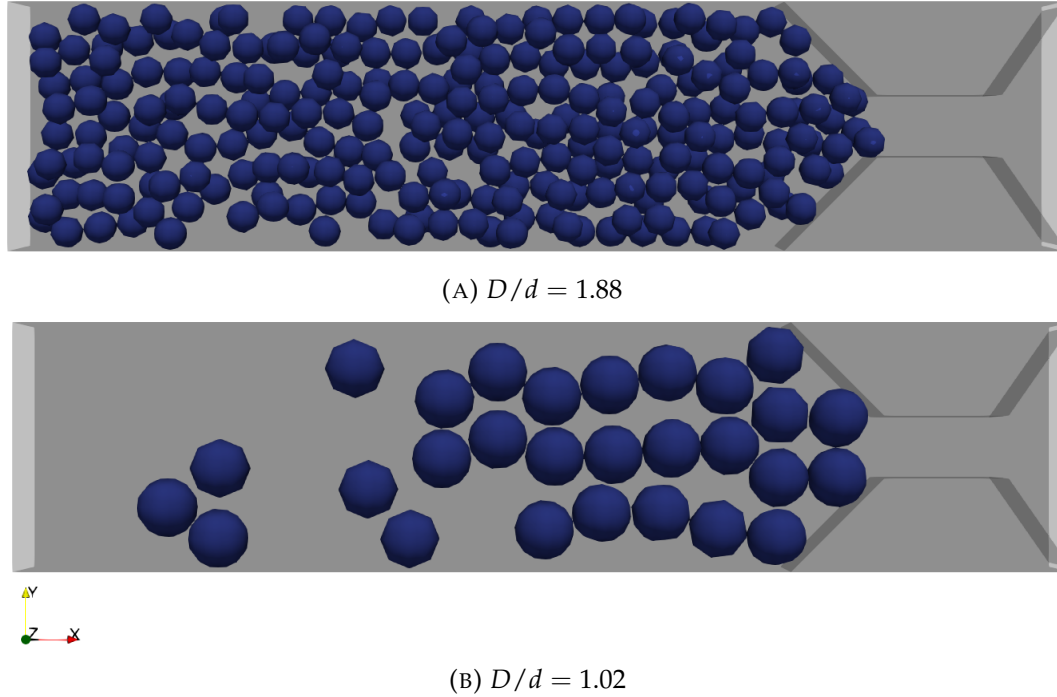


FIGURE 8.1: Clogging events for particles of sizes (A) $53 \mu\text{m}$ and (B) $98 \mu\text{m}$.

meaning that the probability of clogging is constant and the same for each particle, characteristic of a Poisson process. For this case the mean number of escapees is $\langle s \rangle = 7.41$ and the fitted function is shown in dashed black lines.

The Cumulative Distribution Function (CDF) is shown in Figure 8.2 (B),

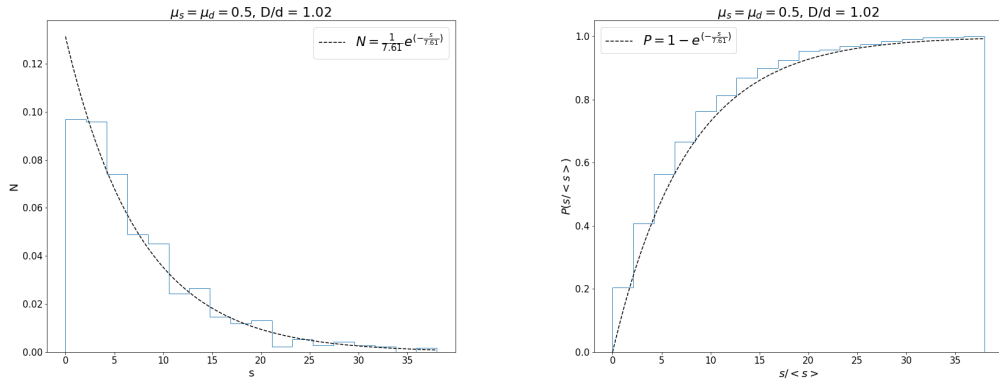
$$P = 1 - e^{-s/\langle s \rangle}, \quad (8.2)$$

this represents the probability of having less than s particles passing through the constriction.

One feature that is important to discuss is that the exponential distribution is best fitted for s greater than the mode. For s less than the mode (the first step in the histogram in Figure 8.2 (A)) the data does not tend to follow the exponential distribution, but N is usually lower than predicted. One can see more examples of PDF's for different values of D/d in the Appendix C, where the effect of small s is observed clearly.

Zuriguél et al. [48], discussed about the origin of the region of *small avalanches* (small s); they came to the conclusion that it is dependent on the way one starts the experiment. In our case, it is interpreted to how we insert the particles into the computational domain. Since they are inserted randomly at the left side of the channel, the particles spawning closer to the middle travel faster due to the Poiseuille profile, then, they usually arrive to the constriction with no partner to form a stable arch. The cases where the first fast particles arrive with a partner to form an arch are scarce, being these the *small avalanches* described by Zuriguél et al.

As a general trend, the mean number of escapees increases with D/d , i.e., with decreasing d , as can be seen in Figure 8.3 (A). Koivisto & Durian [51], proposed an



(A) Probability Density Function (PDF) (B) Cumulative Distribution Function (CDF)

FIGURE 8.2: Plots of the (A) PDF and (B) CDF for the case when $D/d = 98\mu\text{m}$ and $\mu_s = \mu_d = 0.5$.

exponential function to describe the mean mass discharged for a submerged granular hopper, which in our case can be translated to a function for the mean number of escapees

$$\langle s \rangle = e^{a(D/d)^b} + c, \quad (8.3)$$

the parameter b is related to the dimensionality, being 2 for 2D and 3 for 3D systems. The simulations are done in 3D, but they were not far from being pseudo-2D, since the height of the channel is $h = D$, not twice as big as the particles diameter, so two particles cannot fit one next to another along the height of the channel. Therefore, b was left as a free fitting parameter that was found to be equal to 2.57; between 2 and 3 as expected. We suspect that $c = 4.21$ is related to the small avalanches, i.e., to how the simulation is started, but its exact relation is not known; a is found to be 0.65 and considered as just a fitting parameter. The fitted function is shown in dashed black lines in Figure 8.3 (A); the values at the extrema were not taken into account for the fitting since it must be independent of them.

One characteristic of an exponential distribution is that the standard deviation σ for each particle diameter is equal to the mean number of escapees, $\sigma = \langle s \rangle$ [44, 50]. It can be seen in Figure 8.3 (B) where we plot σ against $\langle s \rangle$, that a prominent feature is that the data for each particle size lies on the fitted straight line shown in black dashed lines. However, the slope is equal to 0.74 and not 1 as predicted for an exponential distribution. The reason is attributed once more to the region of small avalanches, the data smaller than the mode of s shifts $\langle s \rangle$ to larger values, making the standard deviation differ from what is predicted. It is interesting to notice that since all the simulations were started in the same way for all particle sizes, the data lies on the same straight line. We speculate that if the simulations are started in a different manner, a different slope would be obtained.

We propose another function of the form

$$\langle s \rangle = e^{\alpha(D/d-1)^\beta} + \delta, \quad (8.4)$$

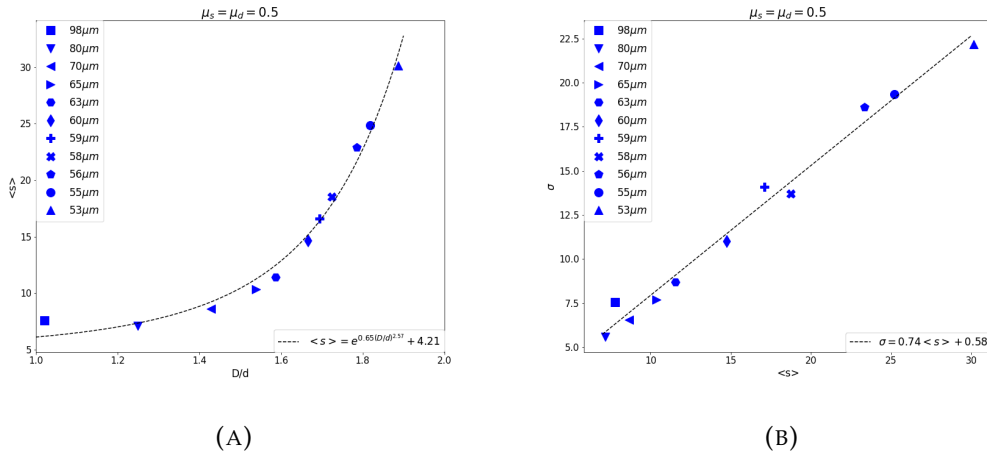


FIGURE 8.3: In figure (A) we plotted the mean number of escapees $\langle s \rangle$ vs. the ratio D/d . The fitted function predicts that $\langle s \rangle$ will grow as exponential to the power $D/d^{2.57}$. In (B) we see the standard deviation σ vs. $\langle s \rangle$. For an exponential distribution $\sigma \sim \langle s \rangle$.

that can describe the behaviour of $\langle s \rangle$. It has the advantage that it is only defined when $D/d > 1$, which is physical since particles bigger than the constriction cannot flow through. However in this case, β is not expected to correspond to the dimensionality. Fitting the parameters as done in Figure 8.3 (A), we obtain $\alpha = 3.74$, $\beta = 1.09$ and $\delta = 4.16$. The new function is plotted together with the data in Figure 8.4 (A). From it, it is complicated to see if the function is better than the one in equation (8.3), but we can compare them by computing the relative error for the two cases, which is defined as

$$E_r = \frac{|\langle s \rangle_{fit} - \langle s \rangle_{sim}|}{\langle s \rangle_{fit}}, \quad (8.5)$$

where $\langle s \rangle_{fit}$ and $\langle s \rangle_{sim}$ are the values of the fitted function and the simulations respectively.

In Figure 8.4 (B) we see the relative error in blue symbols for the equation (8.3) and red for equation (8.4). In general, both fits lay within an error of 10%, except for the value $D/d = 1.02$, which deviates from expected more in our proposal than using equation (8.3). We suspect that the reason why it deviates is due to the small volume fraction imposed at the particles insertion, $\phi = 0.20$. The number of particles inserted decreases as the third power of the diameter, meaning that much less particles spawn for a large value, such as $d = 98 \mu\text{m}$. Then, similarly to the occurrence of small avalanches, the big particles tend to arrive alone to the constriction and cannot form a clog. This should be more noticeable if we reduce ϕ even further at the insertion boundary.

A qualitatively way to describe the statistical behaviour of the clogging events is using a return map, which is essentially plotting the outcome of the i experiment against the outcome of the $i + 1$ experiment. For the case of clogging it means plotting (s_i, s_{i+1}) . In Figure 8.5, we show the return maps for the cases when $D/d = 1.88, 1.66, 1.42$ and 1.02 . The density of points is higher near the mean point $(\langle s \rangle, \langle s \rangle)$, for an exponential distribution and decays exponentially (as expected) the

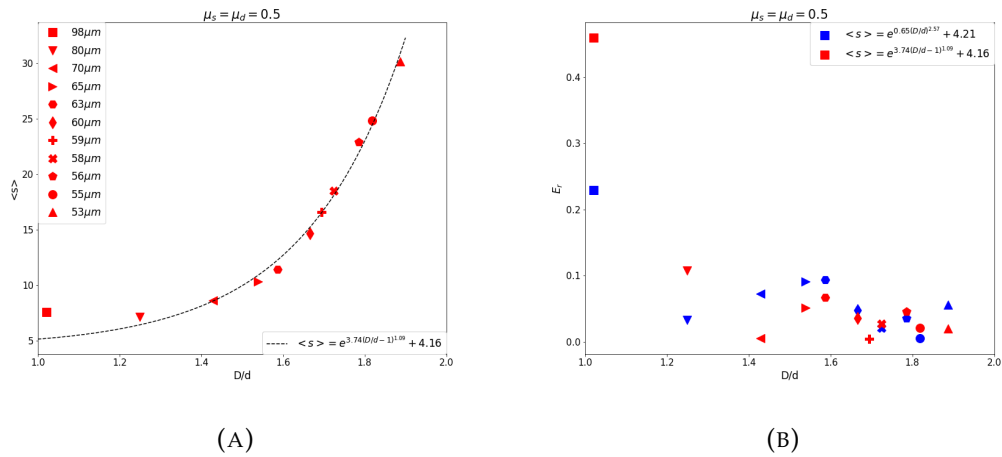


FIGURE 8.4: In figure (A) we plot $\langle s \rangle$ vs. D/d together with our proposed fitted function. In (B) we see the relative error E_r between the simulations results and the fitted functions; in blue symbols the relative error with respect to equation (8.3) and in red with respect to our proposed function (8.4).

further away from this point. It is interesting to see that the *spreading* of the points is related to the standard deviation of the experiments. Since $\sigma \sim \langle s \rangle$, the points in the return maps of smaller particle diameters are more spread than for bigger particles.

As the last part of our analysis, I would like to discuss about the differences between the experimental results obtained by Marin et al. [44] and the results presented here. I started Chapter VII talking about the purpose of the simulations, which was to replicate the clogging behaviour of a constricted suspension flow. We were able to reproduce the results qualitatively by obtaining clogging events when $D/d \in [1.02, 1.88]$; the statistics showed to be Poissonian and well described by an exponential distribution, when discarding the small avalanches region. The exponential dependence of $\langle s \rangle$ on the ratio D/d was also reproduced, either using equation (8.3) or (8.4), similar to what was found in dry granular media [48, 49, 50] and submerged hoppers [51]. However, the mean number of escapees found experimentally by Marin et al., deviated more the larger D/d . For a $D/d = 1.7$, they found experimentally that $\langle s \rangle \sim 100$ whereas we found $\langle s \rangle \sim 25$. For the case when $D/d = 2.07$, it was found experimentally that $\langle s \rangle = \mathcal{O}(10^3)$ and in our simulations this value of the ratio already presented intermittent flow with sporadic permanent clogs.

A deviation from the experiment indicates that there is something we are not taking into account. It is possible that the friction we used was not adequate; however, several simulations were done changing the value of the dynamic friction coefficient (results not shown) with no success to match the experiment. It is hard to do so since there are two free parameters to tune, the static and dynamic friction coefficients, then only one of them should be varied at a time.

There is also the possibility that we cannot tune the friction coefficients to match the experiments and we need to add more complexity to our approach. Until now, only the contact forces and Stokes drag force were added to the model, but reading the

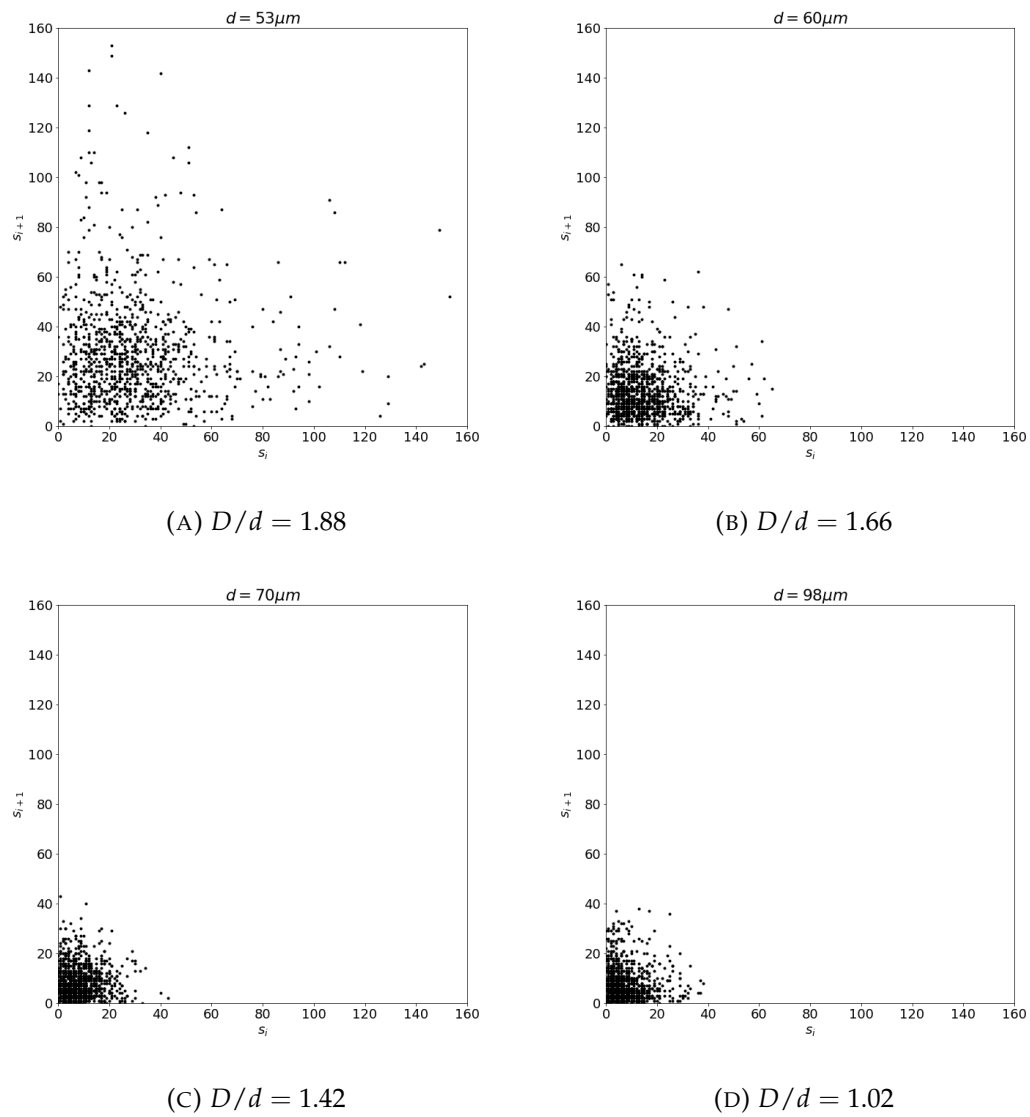


FIGURE 8.5: Return maps for $D/d =$ (A) 1.88, (B) 1.66, (C) 1.42 and (D) 1.02. For a positively skewed exponential distribution, the points agglomerate near the mean.

work done by Metzger et al. [61], we suspect that inclusion of a lubrication force of the form

$$\mathbf{F}_1 = \sum_{ij} \frac{3\pi\eta d^2}{8h_{ij}} \hat{\mathbf{n}}(\mathbf{u}_i - \mathbf{u}_j) \cdot \hat{\mathbf{n}}, \quad (8.6)$$

might be necessary to reproduce the results of the experiment. Here \mathbf{u}_i and \mathbf{u}_j are the velocities of the particles i and j ; the unit normal vector $\hat{\mathbf{n}}$ was defined in equation (2.2) and $h_{ij} = r_{ij} - d$, where r_{ij} is the distance between the centres of the particles i and j . This force acts at a distance $2\epsilon_r \leq h_{ij} \leq d/2$, with ϵ_r the roughness of the particles. It is repulsive when the particles are approaching each other but attractive when they are separating. This change in sign dependent on the particles relative velocity might be necessary to capture the physics of the experiment and replicate the results.

Although we assumed that the flow rate does not affect the clogging probability, following the conclusions drawn by Dorbolo et al., for dry granular media in their article *Influence of the gravity on the discharge of a silo* [62], we do not discard the possibility of the faster-is-slower effect in the flow of suspended particles through microchannels. Meaning that faster (in average) particles might tend to form clogs oftener than slower ones. This effect has already been observed in crowd swarming, sheep herds and grains flowing out a 2D hopper over a vibrated incline [63, 64], and has been suggested for particles flowing through syringes, where increasing the sucking velocity seems to slow down the flow [65]. We are just stipulating that the flow rate might have an effect since we did take a high average flow velocity. In either case, it is worth running several simulations for different flow rates to discard this possibility.

Chapter 9

Conclusions and Outlook

In this thesis we worked on two schemes with very different length scales, from a planetary size to the microscopic realm. We named the first part of the thesis the *propeller project* and the second one the *clogging project*, the two of them connected through the theory of Granular Matter and MercuryDPM. From each project, several conclusions and prospects for future research can be drawn.

9.1 Propeller Project

9.1.1 Conclusions

Saturn's rings are the perfect example where two very different communities converge, those of Granular Matter and Astrophysics. On one side the Granular Matter community often disregards what happens on a big scale (order of thousands of kilometres) since they commonly study macroscopic systems on the human scale; on the other side, the Astrophysics community often disregards what happens in short temporal scales, such as during collisions between particles. In this project we took the best of what both communities have to offer and applied it principally to simulations of ring sections from the reference frame of a moonlet orbiting Saturn in order to study the structures known as propellers.

We derived the forces that the ring particles experience from a completely mechanical point of view, including the expression for the linearised velocity shear profile, without employing a hydrodynamical approach as often used. The Lees-Edwards boundary conditions proved to be appropriate to replicate the velocity shear profile, except for the case when the mean free path of the ring particles is comparable to the size of the computational domain, i.e., very dilute systems, often called a Knudsen gas, since the dynamics would be dominated by interactions with the boundaries and not between the particles themselves.

When fixing a moonlet in the middle of the computational domain and including its gravitational force, propeller structures were visibly found for $\epsilon < 0.50$, for higher restitution coefficients we proposed an arbitrary criterion to discern whether there is a propeller or not; if the ratio between the maximum and the minimum coarse grained density in the propeller region is higher than 2, we considered that the structure is present. When the ratio is smaller than 2, the granular temperature is

sufficiently high to randomize the particles around the moonlet and destroy the propeller. It was found that this corresponds to $\epsilon \approx 0.70$, where the energy density dissipation factor, so called inelasticity, $1 - \epsilon^2 \approx 1/2$, meaning that simulations when $1 - \epsilon^2 > 1/2$ tend to show propellers structures and otherwise do not.

Since our criterion for the appearance of propellers is arbitrary ($\Sigma_{max}/\Sigma_{min} > 2$), the definition of another criterion would change the inequality. For instance, if it is defined as $(\Sigma_{max} - \Sigma_{min})/\Sigma_{min}$, the criterion for the presence of these structures would change to $(\Sigma_{max} - \Sigma_{min})\Sigma_{min} > 1$. It can also be defined as $(\Sigma_{max} - \Sigma_0)/\Sigma_0$, where Σ_0 is the density for the corresponding homogeneous system. However, employing the velocity criterion $v_H > \delta v_y$ for the existence of propellers, where v_H is the Hill velocity and δv_y the fluctuating velocity in y direction, gives us an approximate upper limit for the restitution coefficient where these structures appear, which is given by $\epsilon \approx 0.62$. In either case, both criteria predict a smooth transition between propeller and no-propeller state.

When looking at Figures B.3, B.4 and B.5, there is a clear qualitative difference between the fields of $\epsilon = 0.85$ and $\epsilon = 0.95$, which might mislead us to think that the transition to a no-propeller state is around $\epsilon = 0.95$. This is, naturally, in disagreement with the results obtained using the proposed criteria. However, we consider that a propeller is composed by the *hub* and the *blades*. For the fields where $\epsilon = 0.75$ or 0.85 , the *hub* is still present due to the particles inside the Roche lobe, but the *blades* are not. It is possible to define the absence of a propeller by the non-existence of both the *hub* and the *blades*. But a new criterion should be introduced in this case, possibly regarding the density inside the Roche lobe.

9.1.2 Outlook

As explained in Chapter VI, the propeller structures that we reproduced are not in equilibrium since, for a long integration time, perturbed particles will cross the periodic boundaries making them unrealistic. It is possible to make the domain bigger so that the granular temperature randomizes the particles before crossing, however, the computational time will increase accordingly and the approximation of small curvature in the rotating Cartesian system might not hold any more.

At the beginning of our research, it was observed that the size of the computational domain was big enough to sample unperturbed particles crossing through the periodic boundaries when $\epsilon \approx 0.65$, which is in agreement with the latter results and the criteria proposed, since, at approximately this value of ϵ , the system changes to a no-propeller state.

We believe that in order to create propellers in equilibrium, a modification to the Lees-Edwards boundary conditions (LEBC) must be done. The idea is similar to what Seiß et al. [39] and Michikoshi & Kokubo [12] applied to their planetary ring simulations, where they created eight copies surrounding the main domain in order to sample unperturbed particles entering from the boundaries.

We propose what we call the modified Lees-Edwards boundary conditions (MLEBC), where one copy of the original LEBC is created. We will name the original Lees-Edwards domain LE1 and denote the copy as LE2. In Figure 9.1, we show a schematic image of the MLEBC. The moonlet is shown in black at the center of LE1 but it is not placed in LE2, the black particles are particles before leaving either LE1 or LE2 with

their direction given by black arrows, we drew the particles in white after being reinserted.

The particles labelled with (a) leave LE2 from the right boundary and are reinserted in the respective left boundary but also copied into the left boundary of LE1; the ones labelled with (b) leave LE2 from the left side and are reinserted into LE2 from the right and also copied to LE1 entering from the right boundary. Particles named as (c) and (d) follow the usual LEBC rules as explained in section 6.1.1, being reinserted in their respective domains. Finally, particles labelled as (e) leave LE1 either from the left or right side (shown by the red arrows) and are erased from the simulation.

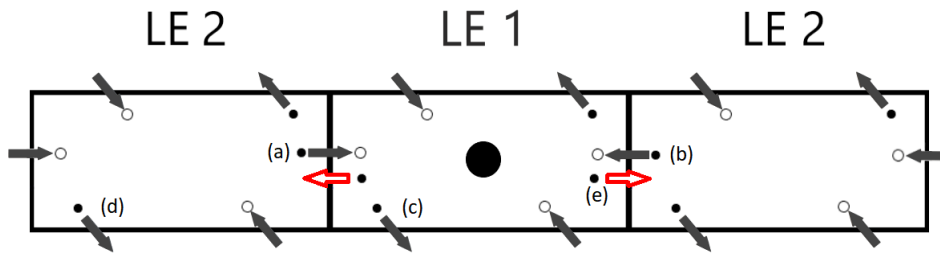


FIGURE 9.1: Schematic image of the modified Lees-Edwards conditions.

This kind of modified conditions should be able to help us simulate propellers in equilibrium, since the particles entering from the left or right boundaries will be unperturbed. It will not be able to reproduce their whole extent unless we make LE1 (and LE2 accordingly) big enough, but it can be very helpful when trying different kinds of contact models where we focus only on the creation and *hub* of the propeller.

Once the MLEBC have been implemented, it would be interesting to simulate particles with different contact models. We suspect that a Hertzian contact model will not make much difference but better explore the effect of adhesive forces or charged particles in simulations with and without a moonlet. Then, using the coarse graining tool as did in Chapter VI, we would be able to sample different times of integration once the propellers are in steady state to reproduce plots like Figure 6.6 with smaller error bars for different contact models.

A natural extension to the work done here is to add self-gravity to the particles in the ring section. Using the AMUSE framework this is easy, since the N-body integrators take into account the gravitational attraction from all particles present in the simulation. Nevertheless, the AMUSE integrators do not consider collisions between particles. A rudimentary implementation of collisions in AMUSE has been tested employing the LSD contact model. However, the long computational time for as few as 1000 particles made it impossible to obtain interesting or conclusive results. It is also possible to implement self-gravity using the MercuryDPM framework, nonetheless, the integration time would scale as $\mathcal{O}(N^2)$, where N is the number of particles, making the simulations computationally expensive and inefficient. A new way to improve the efficiency is open to research. Coupling MercuryDPM with AMUSE is a good option, but this is not a straightforward solution.

Once an efficient way to implement self-gravity is found, one could explore different densities (or, equivalently, packing fractions) to study the appearance of gravity wakes, which are clumps of particles formed due to the self-gravity.

9.2 Clogging Project

9.2.1 Conclusions

With the simple approach used, where only the contact and driving forces are used, we were able to replicate the clogging behaviour of a suspension flow inside a micro-channel using DEM simulations, even with strong approximations. Setting the static and dynamic friction coefficients between particles and walls at $\mu_s = \mu_d = 0.5$, clogs were observed in the range of $D/d \in [1.02, 1.88]$, where D is the width of the constriction and d the particle diameter.

It is observed that the number of escapees s increases exponentially with $(D/d)^b$, where b is a parameter related to the dimensionality of the system. It was found that the probability of clogging is well fitted by an exponential distribution, being the agreement better after the region of small avalanches, when s is larger than the mode, which suggests that clogging in a constricted suspension flow is a Poisson process, i.e., each clogging event is independent from each other and all the particles going through the constriction have the same probability of being the last escapee.

The discrepancies between the probability for the occurrence of small avalanches and the fitted exponential distribution are considered to be a consequence of the way the simulations are started, and are also found in experimental results. When the simulation/experiment is started, the front particles in the middle of the channel flow faster than the others due to the Poiseuille profile, such that they arrive with no partner at the constriction and do not form a clog. The cases when two or more front particles arrive together are scarce and of low probability, therefore, the region of small avalanches in the PDF shows a disagreement with the fitted exponential distribution.

However, since all simulations were started in the same way, a straight line was still found when plotting the standard deviation against the mean number of escapees for all particles sizes, which is characteristic of a Poisson process.

9.2.2 Outlook

There are several ways to improve the simulations. In Chapter VIII we talked about how considering a Poiseuille flow throughout the channel and Poiseuille-like in the constriction was a bold approximation when a high number of particles is present. However, we still consider that we capture the important physics using this estimation, i.e., the particles flow faster in the center of the channel, slower close to the walls and the mean flow velocity increases inside the constriction.

One could, for instance, tune the static and dynamic friction coefficients to match the experimental results. Nevertheless, several matching attempts were done by varying the dynamic friction coefficient with no success (results not shown). With a more complex contact model it might be possible to replicate the experimental results. A good starting point could be the hysteretic spring model described by Luding [18], which gives us the possibility to simulate a repulsive force between particles when they are approaching and an attractive force when they are departing, behaviour that is observed experimentally and considered to be due to lubrication forces.

On the other hand, it is also possible to implement the expression for the lubrication force itself, which is given by equation (8.6) following the work of Metzger et al. [61]. However, one has to be careful since the expression is singular at a contact between particles. Therefore, a new parameter is introduced, the particle roughness ϵ_r , that is the minimum distance at which the lubrication forces actuate; ϵ_r is also experimentally unknown and needs to be tuned.

Several simulations with different average flow velocities must be run to discard the possibility of a faster-is-slower effect, since our assumption that the flow rate does not affect the clogging probability is based on the work done about dry granular media. If this effect is present, a slower average flow velocity might reduce the probability of clogging and, therefore, increase the mean number of escapes s .

As a final option, if nothing aforementioned works, one could couple a CFD solver to MercuryDPM to compute the flow exactly (as much as the resolution permits), including a linear contact force, the drag and lubrication forces. Nonetheless, this option is not straightforward and each simulation will be computationally much more expensive.

Bibliography

- [1] National Aeronautics and Space Administration (2017). *The Saturn System Through the Eyes of Cassini*, NASA/JPL-Caltech/Space Science Institute.
- [2] Dougherty, M.K., et al. (2009). *Saturn from Cassini-Huygens*, Springer.
- [3] Brown, R.H., et al. (2009). *Titan from Cassini-Huygens*, Springer.
- [4] Boss, A. P. (2001). *Gas giant protoplanet formation: Disk instability models with thermodynamics and radiative transfer*, *The Astrophysical Journal*, 563(1), 367.
- [5] Andreotti, B., Forterre, Y., Pouliquen, O. (2013). *Granular Media: Between Fluid and Solid*, Cambridge University Press.
- [6] Müller, M.-K., (2007). *Long-Range Interactions in Dilute Granular Systems*, University of Twente, Enschede.
- [7] Spahn, F., & Sremčević, M. (2000). *Density patterns induced by small moonlets in Saturn's rings?*, *Astronomy and Astrophysics*, 358, 368-372.
- [8] Sremčević, M., Spahn, F., & Duschl, W. J. (2002). *Density structures in perturbed thin cold discs*, *Monthly Notices of the Royal Astronomical Society*, 337(3), 1139-1152.
- [9] Seiß, M., Albers, N., Sremčević, M., Schmidt, J., Salo, H., Seiler, M., ... & Spahn, F. (2018). *Hydrodynamic Simulations of Moonlet-induced Propellers in Saturn's Rings: Application to Blériot*, *The Astronomical Journal*, 157(1), 6.
- [10] National Aeronautics and Space Administration (2017). *Cassini Targets a Propeller in Saturn's A Ring*, NASA/JPL-Caltech/Space Science Institute. <https://www.nasa.gov/image-feature/jpl/pia21433/cassini-targets-a-propeller-in-saturns-a-ring>
- [11] National Aeronautics and Space Administration (2017). *Bleriot Propeller Close-up*, NASA/JPL-Caltech/Space Science Institute. <https://www.nasa.gov/image-feature/jpl/pia21447/bleriot-propeller-close-up>
- [12] Michikoshi, S., & Kokubo, E. (2011). *Formation of a propeller structure by a moonlet in a dense planetary ring*, *The Astrophysical Journal Letters*, 732(2), L23.
- [13] Rein, H., & Papaloizou, J. C. (2010). *Stochastic orbital migration of small bodies in Saturn's rings*, *Astronomy & Astrophysics*, 524, A22.
- [14] Thornton, A. R., et al. (2013). *A review of recent work on the Discrete Particle Method at the University of Twente: An introduction to the open-source package Mercury-DPM*, University of Twente, Enschede.

- [15] Thornton, A. R., Weinhart, T., Luding, S. and Bokhove, O. (2012). *Modeling of particle size segregation: Calibration using the discrete particle method*, Mod. Phys. C 23, 1240014.
- [16] Portegies, S. & McMillan, S. (2018). *Astrophysical Recipes: The Art of AMUSE*, IOP Publishing.
- [17] Brilliantov, N. V., Pöschel, T. (2004). *Kinetic Theory of Granular Gases*, Oxford University Press.
- [18] Herrmann, H. J., Hovi, J. P., Luding, S. (1998). *Physics of Dry Granular Media*, Nato ASI series.
- [19] Taghizadeh, K., Combe, G., Luding, S. (2017). *ALERT Doctoral School 2017 Discrete Element Modeling*, The Alliance of Laboratories in Europe for Education, Research and Technology.
- [20] Goldhirsch, I. (2010). *Stress, stress asymmetry and couple stress: from discrete particles to continuous fields*, Granular Matter, 12(3), 239-252.
- [21] Weinhart, T., Thornton, A. R., Luding, S., & Bokhove, O. (2012). *From discrete particles to continuum fields near a boundary*, Granular Matter, 14(2), 289-294.
- [22] Weinhart, T., Luding, S., & Thornton, A. R. (2013). *From discrete particles to continuum fields in mixtures*, In AIP conference proceedings (Vol. 1542, No. 1, pp. 1202-1205). AIP.
- [23] Tunuguntla, D. R., Thornton, A. R., & Weinhart, T. (2016). *From discrete elements to continuum fields: Extension to bidisperse systems*. Computational particle mechanics, 3(3), 349-365.
- [24] Weinhart, T., Hartkamp, R., Thornton, A. R., & Luding, S. (2013). *Coarse-grained local and objective continuum description of three-dimensional granular flows down an inclined surface*, Physics of Fluids, 25(7), 070605.
- [25] Weinhart, T., Labra, C., Luding, S., & Ooi, J. Y. (2016). *Influence of coarse-graining parameters on the analysis of DEM simulations of silo flow*, Powder technology, 293, 138-148.
- [26] Thornton, S. T., Marion, J. B. (2004). *Classical Dynamics of Particles and Systems*, Brooks/Cole.
- [27] Taylor, J. R. (2005). *Classical Mechanics*, University Science Books.
- [28] Goldstein, H., Poole, C., Safko, J. (2000). *Classical Mechanics*, Addison Wesley.
- [29] Steigerwald, B., & Jones, N. (2018). *NASA Research Reveals Saturn is Losing Its Rings at "Worst-Case-Scenario" Rate*, NASA Goddard Space Flight Center. <https://solarsystem.nasa.gov/news/794/nasa-research-reveals-saturn-is-losing-its-rings-at-worst-case-scenario-rate/>
- [30] Hairer, E., Lubich, C., & Wanner, G. (2006). *Geometric numerical integration: structure-preserving algorithms for ordinary differential equations*, Springer Science & Business Media.
- [31] Sanz-Serna, J. M., & Calvo, M. P. (2018). *Numerical hamiltonian problems*, Courier Dover Publications.

- [32] Pelupessy, F. I., Jänes, J., & Zwart, S. P. (2012). *N-body integrators with individual time steps from Hierarchical splitting*, *New Astronomy*, 17(8), 711-719.
- [33] Jänes, J., Pelupessy, I., & Zwart, S. P. (2014). *A connected component-based method for efficiently integrating multi-scale N-body systems*, *Astronomy & Astrophysics*, 570, A20.
- [34] Lees, A. W., & Edwards, S. F. (1972). *The computer study of transport processes under extreme conditions*, *Journal of Physics C: Solid State Physics*, 5(15), 1921.
- [35] Wagner, A. J., & Pagonabarraga, I. (2002). *Lees–Edwards boundary conditions for lattice Boltzmann*, *Journal of Statistical Physics*, 107(1-2), 521-537.
- [36] Pan, D., Hu, J., & Shao, X. (2016). *Lees–Edwards boundary condition for simulation of polymer suspension with dissipative particle dynamics method*, *Molecular Simulation*, 42(4), 328-336.
- [37] Spahn, F., & Schmidt, J. (2006). *Hydrodynamic description of planetary rings*, *GAMM-Mitteilungen*, 29(1), 118-143.
- [38] Seiß, M., & Spahn, F. (2011). *Hydrodynamics of Saturn’s dense rings*, *Mathematical Modelling of Natural Phenomena*, 6(4), 191-218.
- [39] Seiß, M., Spahn, F., Sremčević, M., & Salo, H. (2005). *Structures induced by small moonlets in Saturn’s rings: Implications for the Cassini Mission*, *Geophysical Research Letters*, 32(11).
- [40] Luding, S. (2009). *Towards dense, realistic granular media in 2D*, *Nonlinearity*, 22(12), R101.
- [41] Koon, W. S., Lo, M. W., Marsden, J. E., & Ross, S. D. (2006). *Dynamical systems, the three-body problem and space mission design*, California Institute of Technology, Pasadena, CA, USA.
- [42] Abad, A. (2012). *Astrodinámica*, Editorial Bubok.
- [43] Salo, H. (1995). *Simulations of dense planetary rings: III. Self-gravitating identical particles*, *Icarus*, 117(2), 287-312.
- [44] Marin, A., Lhuissier, H., Rossi, M., & Kähler, C. J. (2018). *Clogging in constricted suspension flows*. *Physical Review E*, 97(2), 021102.
- [45] Guimarães, T., Marin, A., Kähler, C. J., Barnkob, R. (Unpublished). *Acoustically-assisted Fluidic Hourglasses*.
- [46] To, K., Lai, P. Y., & Pak, H. K. (2001). *Jamming of granular flow in a two-dimensional hopper*, *Physical review letters*, 86(1), 71.
- [47] Beverloo, W. A., Leniger, H. A., & Van de Velde, J. (1961). *The flow of granular solids through orifices*, *Chemical engineering science*, 15(3-4), 260-269.
- [48] Zuriguel, I., Garcimartín, A., Maza, D., Pagnaloni, L. A., & Pastor, J. M. (2005). *Jamming during the discharge of granular matter from a silo*, *Physical Review E*, 71(5), 051303.
- [49] Janda, A., Zuriguel, I., Garcimartín, A., Pagnaloni, L. A., & Maza, D. (2008). *Jamming and critical outlet size in the discharge of a two-dimensional silo*, *EPL (Europhysics Letters)*, 84(4), 44002.

- [50] Thomas, C. C., & Durian, D. J. (2013). *Geometry dependence of the clogging transition in tilted hoppers*, Physical Review E, 87(5), 052201.
- [51] Koivisto, J., & Durian, D. J. (2017). *Effect of interstitial fluid on the fraction of flow microstates that precede clogging in granular hoppers*, Physical Review E, 95(3), 032904.
- [52] Zuriguel, I., Parisi, D. R., Hidalgo, R. C., Lozano, C., Janda, A., Gago, P. A., ... & Maza, D. (2014). *Clogging transition of many-particle systems flowing through bottlenecks*, Scientific reports, 4, 7324.
- [53] Zuriguel, I. (2014). *Invited review: Clogging of granular materials in bottlenecks*, arXiv preprint arXiv:1412.5806.
- [54] Bruus, H., (2008). *Theoretical Microfluidics*, Oxford University Press.
- [55] Kundu, P. K., Cohen, I. M., Dowling, D. R. (2016). *Fluid Mechanics*, Academic Press.
- [56] Haberman, R. (2012). *Applied partial differential equations with Fourier series and boundary value problems*, Pearson Higher Ed.
- [57] Flemmer, R. L., & Banks, C. L. (1986). *On the drag coefficient of a sphere*, Powder Technology, 48(3), 217-221.
- [58] Mikhailov, M. D., & Freire, A. S. (2013). *The drag coefficient of a sphere: an approximation using Shanks transform*, Powder technology, 237, 432-435.
- [59] Beetstra, R. (2005). *Drag force in random arrays of mono-and bidisperse spheres*, University of Twente.
- [60] Hidalgo, R. C., Goñi-Arana, A., Hernández-Puerta, A., & Pagonabarraga, I. (2018). *Flow of colloidal suspensions through small orifices*. Physical Review E, 97(1), 012611.
- [61] Metzger, B., Pham, P., & Butler, J. E. (2013). *Irreversibility and chaos: Role of lubrication interactions in sheared suspensions*, Physical review E, 87(5), 052304.
- [62] Dorbolo, S., Maquet, L., Brandenbourger, M., Ludewig, F., Lumay, G., Caps, H., ... & Dowson, A. (2013). *Influence of the gravity on the discharge of a silo*, Granular Matter, 15(3), 263-273.
- [63] Helbing, D., Farkas, I., & Vicsek, T. (2000). *Simulating dynamical features of escape panic*, Nature, 407(6803), 487.
- [64] Pastor, J. M., Garcimartín, A., Gago, P. A., Peralta, J. P., Martín-Gómez, C., Ferrer, L. M., ... & Zuriguel, I. (2015). *Experimental proof of faster-is-slower in systems of frictional particles flowing through constrictions*, Physical Review E, 92(6), 062817.
- [65] Muecke, T. W. (1979). *Formation fines and factors controlling their movement in porous media*, Journal of petroleum technology, 31(02), 144-150.
- [66] Spahn, F., Petzschmann, O., Schmidt, J., Sremčević, M., & Hertzsch, J. M. (2001). *Granular viscosity, planetary rings and inelastic particle collisions*, In Granular Gases (pp. 363-385). Springer, Berlin, Heidelberg.

Appendix A

Granular Temperature of a Sheared Gas

As output, MercuryDPM returns an energy file for a chosen number of time steps per simulation. The kinetic, elastic and gravitational potential energy are contained in this file, therefore, it was natural for us to plot the kinetic energy as a function of time for different restitution coefficients (plots not shown). A sudden jump in the kinetic energy or any discontinuity is a sign that something has gone wrong in the simulation.

For an integration time of about 40,000 s , the systems in section 6.1 showed no discontinuity. The energy remained in the same order of magnitude for all simulations except for when $\epsilon = 0.95$ and 0.99 . In this temporal range, the energy for the aforementioned ϵ 's seemed to grow indefinitely unlike the other restitution coefficients. In reality, the energy does not grow indefinitely, this is an effect of the Lees-Edwards boundaries shearing and the high restitution coefficient. After a transient time, the kinetic energy settles to an asymptotic value depending on ϵ .

In this Appendix, we follow the formalism described in *Towards Dense, Realistic Granular Media in 2D* by Luding (2009) [40], and apply it to a simplified system similar to the one described in Chapter VI section 6.1 to find the time at which the kinetic energy K saturates. In practice, it is easier to work with the granular temperature T rather than with K , as we will see in the following sections, since it is related to the fluctuating kinetic energy K_T in 2D by

$$T = \frac{K_T}{N} = \frac{1}{2}mv_T^2, \quad (\text{A.1})$$

with the number of particles N , the mass of the particles m and the fluctuating velocity v_T . Along the thesis we also used δv to denote the fluctuating velocity, but here we use v_T to follow the notation of Luding [40].

A.1 Energy Balance Equation

Assume a single-species granular packing, where the mass and momentum are microscopically conserved at each collision, therefore also conserved macroscopically. Energy, on the other hand, is not conserved microscopically for inelastic particles, but it can be inserted into or dissipated from the system. However, it is possible to

write a balance equation considering the energy density dissipation rate I and the energy density input rate J . Then, the energy balance equation can be written as

$$\partial_t \left(\frac{1}{2} \rho u^2 + \frac{1}{2} \rho v_T^2 \right) + \partial_k \left[\left(\frac{1}{2} \rho u^2 + \frac{1}{2} \rho v_T^2 \right) u_k \right] = -\partial_k [u_i \sigma_{ik} + q_k] + \rho u_i f_i - I + J, \quad (\text{A.2})$$

where, for shortness sake, we used the notation $\frac{\partial}{\partial x_k} = \partial_k$ to denote partial derivatives with respect to the k coordinate. In equation (A.2), u represents the average or streaming velocity, ρ the mass density of the packing, σ_{ij} the stress tensor, q_i the heat flux and f_i any body force such as gravity.

Furthermore, suppose that only the fluctuating velocity depends on time, $v_T = v_T(t)$, and the velocity components are $u_y = 0$ and $u_x = u_x(y)$ resembling the constant shear of a ring section, such that the velocity gradients are zero; we also assume that there is no energy input and that gravity is negligible. Then, equation (A.2) becomes

$$\frac{1}{2} \rho \partial_t (v_T^2) = -\partial_k [u_x \sigma_{xk}] - I. \quad (\text{A.3})$$

It might seem risky to neglect gravity and not include inertial forces such as the centrifugal or Coriolis since they are clearly included in the simulations in Chapter VI. However, body forces are not relevant for the increment of granular temperature as the Lees-Edwards shearing is, which is included in the stress tensor. Contrary to what one might think, the inertial body forces described in section 6.1 lower the granular temperature, bounding the movement of the particles into an epicyclic motion [66].

With all these assumptions, it is possible to find an analytical solution for T as we will see in further sections; we expect that the solution will give us an insight for the time at which the granular temperature saturates for a ring section simulation.

A.2 Constitutive Relations and Transport Coefficients

In order to solve equation (A.3), we need to specify the constitutive relations and transport coefficients required. The only constitutive relation that we need to define is the stress tensor

$$\sigma_{ij} = p \delta_{ij} + \sigma_{ij}^D. \quad (\text{A.4})$$

It is divided into one isotropic part which involves the pressure p and a deviatoric one containing the deviatoric stress tensor

$$\sigma_{ij}^D = -\eta [\partial_j u_i + \partial_i u_j], \quad (\text{A.5})$$

where η is the shear viscosity and δ_{ij} the Kronecker delta as usual.

The transport coefficients involved are given, according to Luding [40], by:

$$I = \frac{\rho^p \phi^2 g(\phi) v_T^3}{4s_0} (1 - \epsilon^2), \quad (\text{A.6})$$

$$p = \frac{\rho^p \phi v_T^2}{2} [1 + 2\phi g(\phi)], \quad (\text{A.7})$$

$$\eta = f \frac{\rho^p \phi v_T s_0}{2[\phi g(\phi)]} \left[1 + 2\phi g(\phi) + \left(1 + \frac{8}{\pi} \right) (2\phi g(\phi))^2 \right], \quad (\text{A.8})$$

corresponding to the energy density dissipation rate, pressure and shear viscosity respectively. We see already in (A.6) the dependence of I on the restitution coefficient ϵ .

For very dilute systems, $\phi \ll 1$, the pair correlation function $g(\phi)$ can be approximated to

$$g_2(\phi) = \frac{1 - 7\phi/16}{(1 - \phi)^2}, \quad (\text{A.9})$$

dependent on the packing fraction ϕ . The particle density is denoted by ρ^p , the free path $s(\phi)$ is given by

$$s(\phi) = \frac{s_0}{\phi g(\phi)}, \quad (\text{A.10})$$

where

$$s_0 = \frac{\sqrt{2\pi}d}{8},$$

d is the particle diameter and f a correction factor proposed by Luding

$$f = 1 + \frac{c_\eta}{\phi_\eta - \phi} - \frac{c_\eta}{\phi_\eta},$$

where $c_\eta = 0.037$ and $\phi_\eta = 0.71$.

A.3 Sheared Granular Gas

For the case of a granular gas simulation with Lees-Edwards boundary conditions as explained in section 6.1.1 and the above mentioned assumptions in section A.1, the shear rate is

$$\partial_y u_x = \dot{\gamma},$$

such that the only non-trivial component of the stress tensor reads

$$\sigma_{xy} = -\eta\dot{\gamma}, \quad (\text{A.11})$$

then, the first term of the right hand side of equation (A.3) becomes

$$\partial_y [u_x \sigma_{xy}] = \sigma_{xy} \dot{\gamma} = -\eta \dot{\gamma}^2. \quad (\text{A.12})$$

Inserting (A.6) and (A.12) into (A.3), we obtain the equation for the evolution of the fluctuating velocity of a homogeneous sheared granular gas:

$$\frac{1}{2} \rho \partial_t (v_T^2) = \eta \dot{\gamma}^2 - \frac{\rho^p \phi^2 g(\phi) v_T^3}{4s_0} (1 - \epsilon^2). \quad (\text{A.13})$$

It can be easily translated to an equation for the granular temperature using

$$v_T^2 = \frac{2T}{m}$$

and $\rho = \rho^p \phi$ so that (A.13) becomes

$$\partial_t T = \frac{m}{\rho^p \phi} \eta \dot{\gamma}^2 - \frac{\phi g(\phi) (1 - \epsilon^2)}{\sqrt{2ms_0}} T^{3/2}. \quad (\text{A.14})$$

We must simplify it first before attempting to solve it since there is a temperature dependence hidden inside the viscosity.

The shear rate for a granular gas orbiting in a circular manner as explained in Chapter VI is given by

$$\dot{\gamma} = \frac{3}{2} \Omega_0,$$

where Ω_0 is the Kepler frequency. The particle mass can be obtained from the particle density ρ^p and the particle volume V^p

$$m = \rho^p V^p = \rho^p \frac{4}{3} \pi a^3,$$

with a the particle radius; notice that we use the volume since we consider a pseudo-two-dimensional system with spherical particles lying on a plane.

Using these relations and equation (A.8) for the shear viscosity, one can write the first term of the right hand side in equation (A.14) as

$$\frac{m}{\rho^p \phi} \eta \dot{\gamma}^2 = AT^{1/2}, \quad (\text{A.15})$$

where

$$A = \frac{\sqrt{ms_0}}{\sqrt{2}\phi g(\phi)} \left[1 + 2\phi g(\phi) + \left(1 + \frac{8}{\pi} \right) (\phi g(\phi))^2 \right] \dot{\gamma}^2, \quad (\text{A.16})$$

and call B the numerical factor in the second term of the right hand side in (A.14)

$$B = \frac{\phi g(\phi)(1 - \epsilon^2)}{\sqrt{2ms_0}}, \quad (\text{A.17})$$

then, we recast equation (A.14) in the simple form

$$\frac{d}{dt}T = AT^{1/2} - BT^{3/2}, \quad (\text{A.18})$$

whose solution is given by

$$t = \frac{2}{\sqrt{AB}} \left[\operatorname{arctanh} \left(\sqrt{\frac{BT}{A}} \right) - \operatorname{arctanh} \left(\sqrt{\frac{BT_0}{A}} \right) \right], \quad (\text{A.19})$$

where T_0 is an initial value of the granular temperature. The solution of T as a function of time is given implicitly in (A.19).

When $t \rightarrow \infty$, it is possible to find a steady state solution just equating the right hand side terms in (A.18)

$$AT^{1/2} = BT^{3/2}, \quad (\text{A.20})$$

then, the final temperature at a very long time $T(t \rightarrow \infty) = T_f$ will be given by

$$T_f = \frac{m\dot{\gamma}^2 s_0^2}{(1 - \epsilon^2)} \left[\frac{1}{(\phi g(\phi))^2} + \frac{2}{\phi g(\phi)} + \left(1 + \frac{8}{\pi} \right) \right]. \quad (\text{A.21})$$

In Figure A.1 we plot the granular temperature for the systems with Lees-Edwards boundary conditions described in section 6.1, namely, with the relevant parameters given by

$$\begin{aligned} \Omega_0 &= 1.538 \times 10^{-4} \text{ s}^{-1}, \\ \rho^p &= 500 \text{ kg/m}^3, \\ \phi &\approx 0.01, \\ a &= 2 \text{ m}, \end{aligned}$$

unless stated otherwise, from where all the transport coefficients can be computed. We observe T for four different restitution coefficients, where the light colors correspond to a Ring Gas (RG), including the inertial forces given by equations (5.41), (5.43) and (5.44); the darker colors correspond to simulations of a Free Gas (FG) with no inertial forces; in dashed lines with the same dark colors, we see the prediction for the Final Temperature (FT) that the Free Gases should reach after a transient

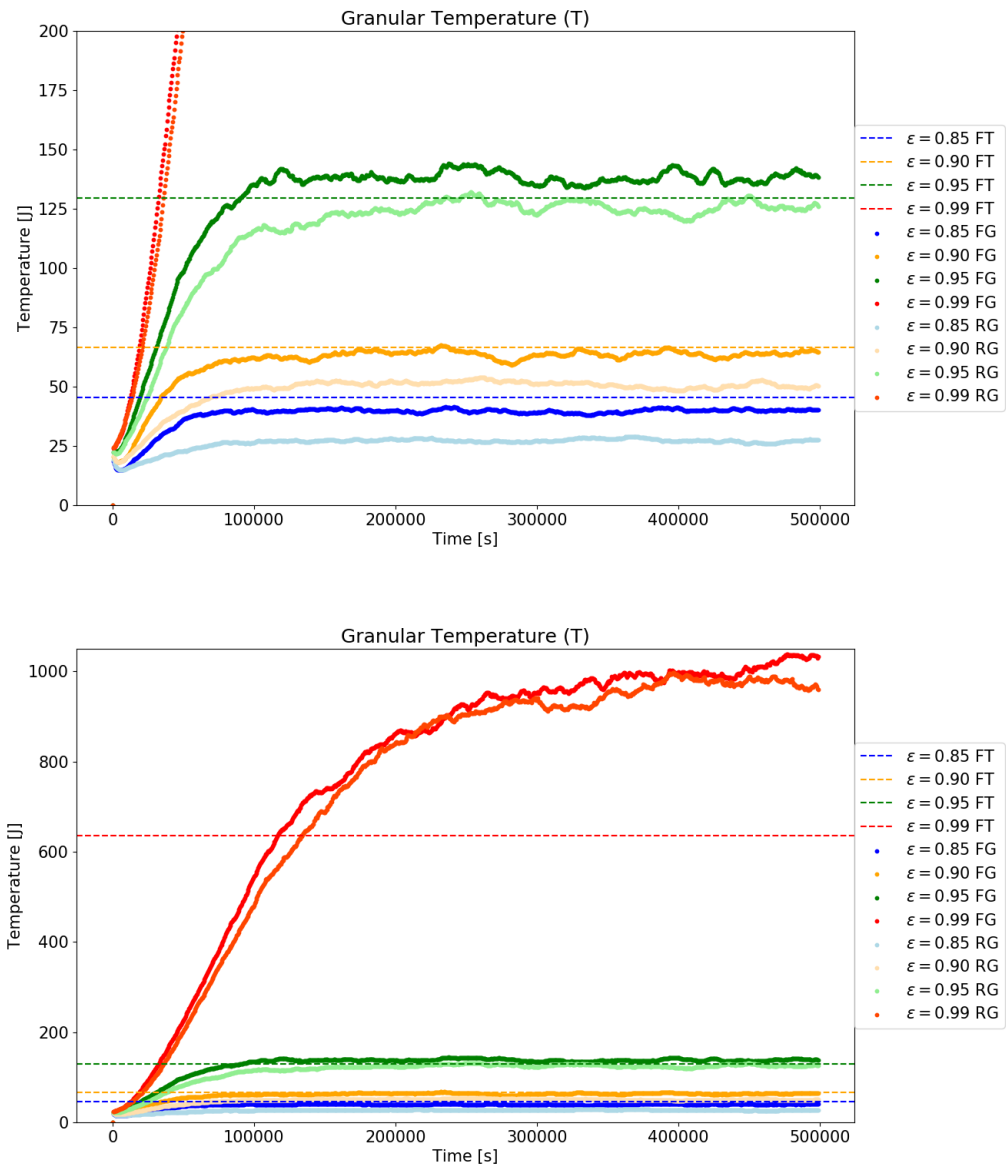


FIGURE A.1: Granular temperature for a Ring Gas (RG) and a Free Gas (FG), corresponding to simulations with and without inertial forces respectively for different restitution coefficients. In dashed lines we plotted the theoretical Final Temperature (FT) for a granular gas without inertial forces, equation (A.21).

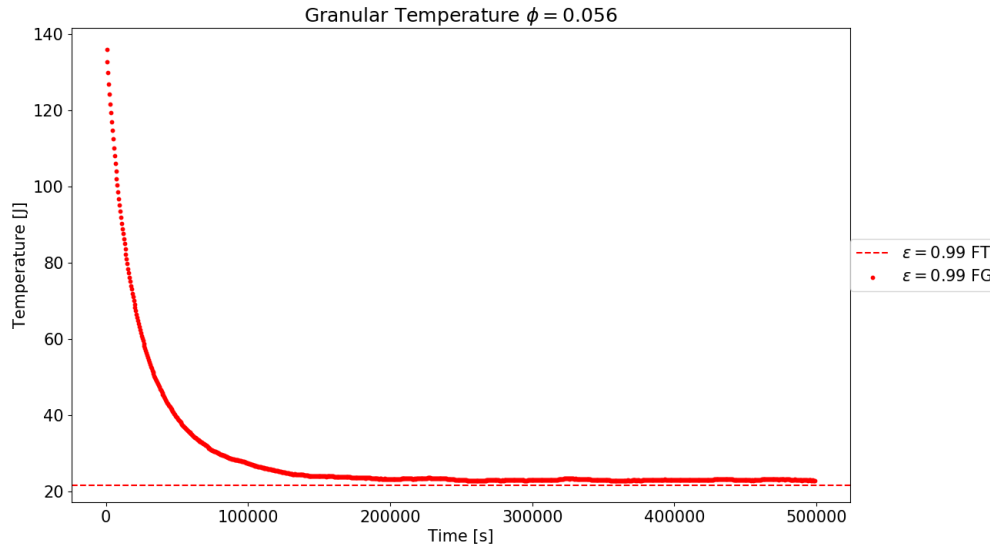


FIGURE A.2: Comparison between theoretical granular temperature and simulations for a free cooling granular gas for $\phi = 0.056$.

time, equation (A.21). It is seen that for restitution coefficients higher than 0.85, the saturation time is reached after 50,000 seconds of integration.

As stipulated, the Ring Gas saturates at a slightly lower granular temperature than the Free Gas due to the epicyclic motion of the particles. The predicted Final Temperature is in moderate good agreement with the Free Gas temperature, except for the case when $\epsilon = 0.99$. We suspect that this deviation is an effect of the low packing fraction and high restitution coefficient. The Lees-Edwards boundaries will speed up the particles at each crossing, since the mean free path is only a few times smaller than the size of the computational domain, the almost elastic particles are not able to dissipate the kinetic energy obtained from the boundaries in just a few collisions. Therefore, the granular temperature rises higher than predicted.

To prove this hypothesis we simply have to increase the packing fraction by a factor of 5 and compare the theoretical Final Temperature with the saturation value of the Free Gas for $\epsilon = 0.99$, which is shown in Figure A.2. It is clear that the agreement is much better than for a lower packing fraction, therefore validating our hypothesis.

A.4 Free Cooling Granular Gas

For a free cooling granular gas the heating term in equation (A.14) disappears

$$\frac{d}{dt} T = -\frac{\phi g(\phi)(1 - \epsilon^2)}{\sqrt{2ms_0}} T^{3/2}, \quad (\text{A.22})$$

and using the same definition as in (A.17) we can recast the last equation to

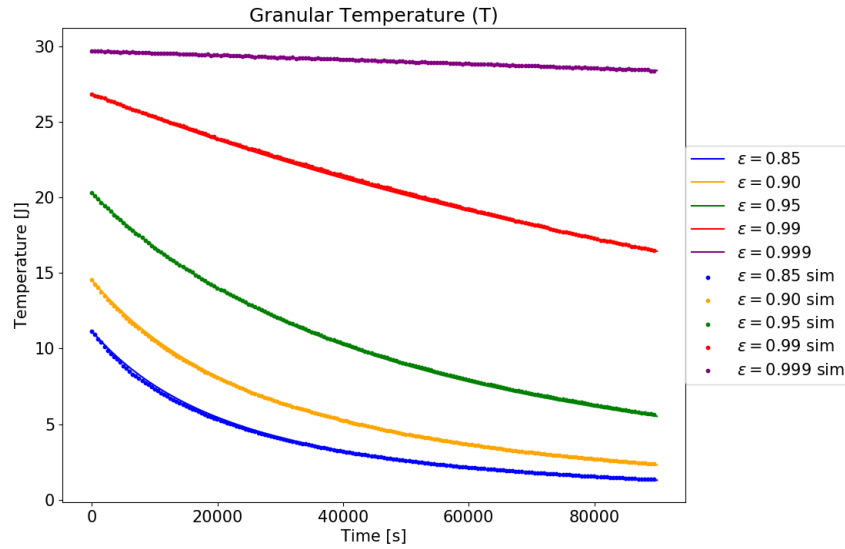


FIGURE A.3: Comparison between theoretical granular temperature and simulations for a free cooling granular gas. The theoretical result lies almost exactly on the simulations data.

$$\frac{d}{dt}T = -BT^{3/2}, \quad (\text{A.23})$$

whose solution is given by

$$T = \frac{T_0}{\left(1 + \frac{\sqrt{T_0}}{2}Bt\right)^2}, \quad (\text{A.24})$$

commonly known as Haff's law, where T_0 is the initial granular temperature.

We ran simulations keeping the same parameters as the last subsection, but changing the Lees-Edwards conditions for periodic boundaries to remove the heating from the simulations. In Figure A.3 we show the granular temperature for the same four restitution coefficients and we compared it to the theoretical prediction, equation (A.24).

All simulations were started with the same initial conditions, nevertheless, since the initial velocities were imposed using a random uniform distribution, we had to wait for 10,000 seconds to sample the gas with realistic initial velocities, thus the reason why the five curves start in different temperatures. In this case it is not important the initial temperature, but to compare Haff's law with the respective T_0 . As it shown in Figure A.3, there is a excellent agreement between the simulations and theory, dots and solid lines respectively. This case deviates from the situation in a ring system due to the lack of a heating term. However, it is a simple test to try the codes and check the validity of the stiffness and dissipation used for the particles.

Appendix B

Coarse Graining Images of Propellers

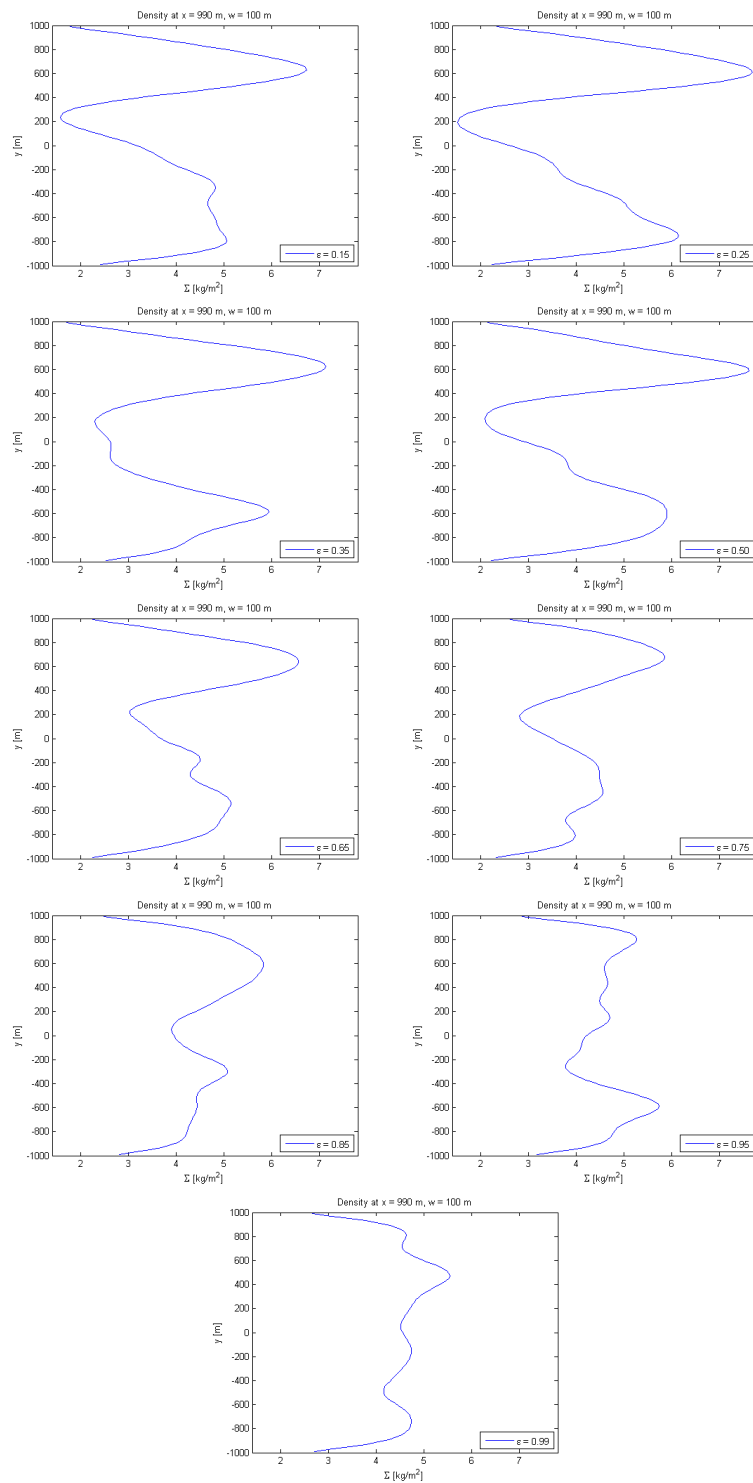


FIGURE B.1: Coarse grained density at $x = 990$ m for 30,000 particles and different coefficients of restitution.

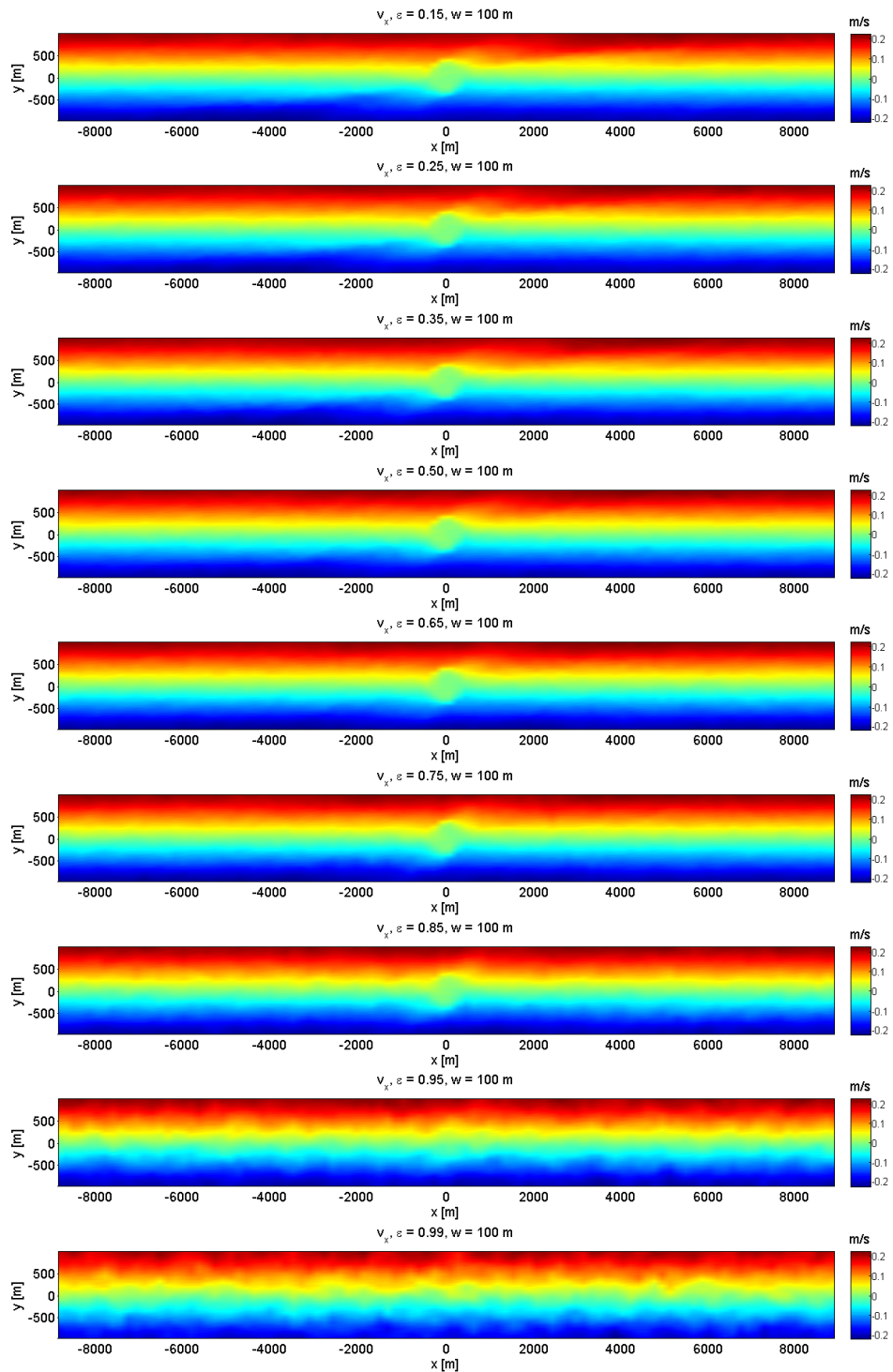


FIGURE B.2: Coarse grained velocity in the x direction for 30,000 particles and different coefficients of restitution.

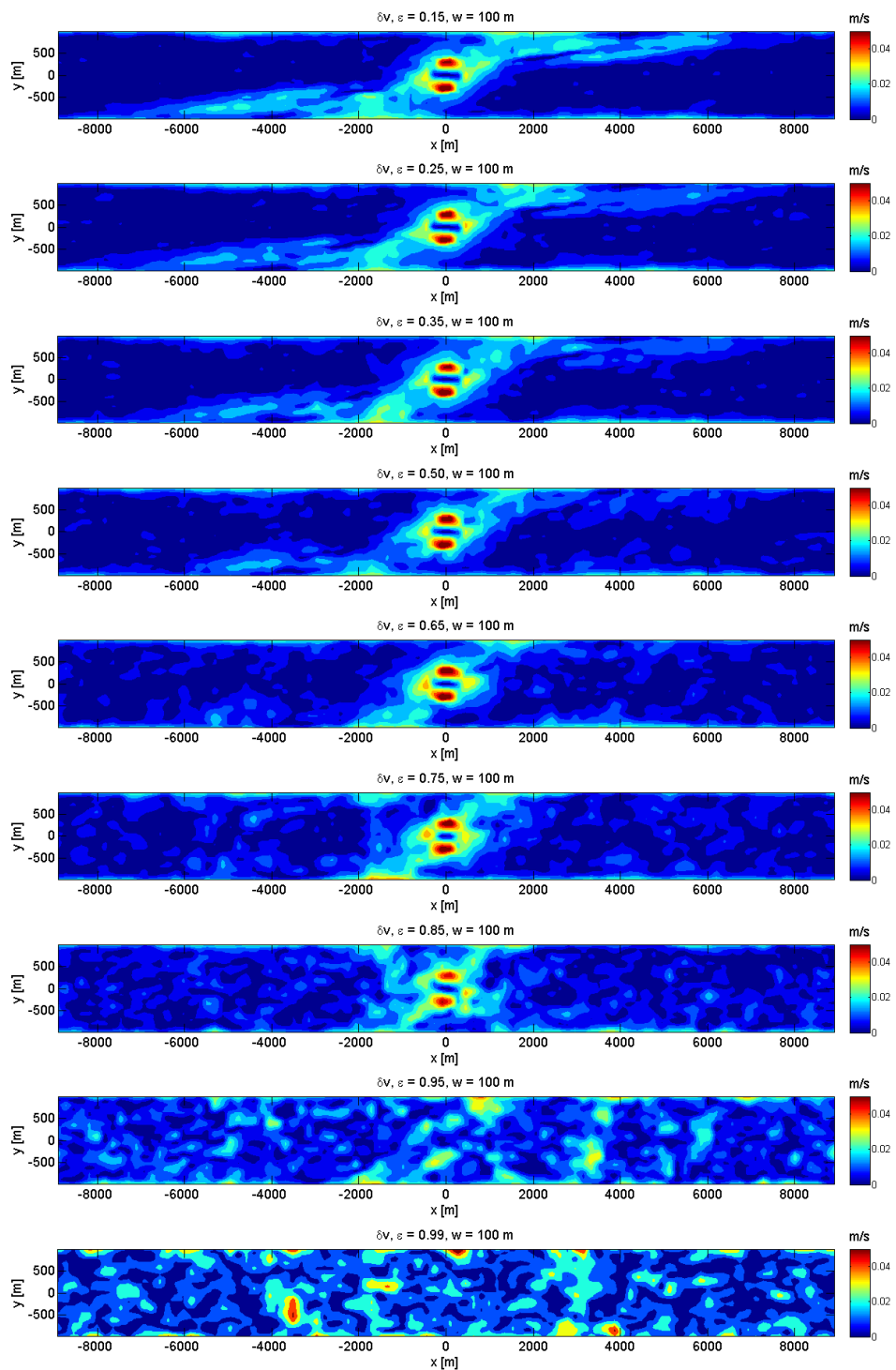


FIGURE B.3: Total coarse grained fluctuating velocity for 30,000 particles and different coefficients of restitution.

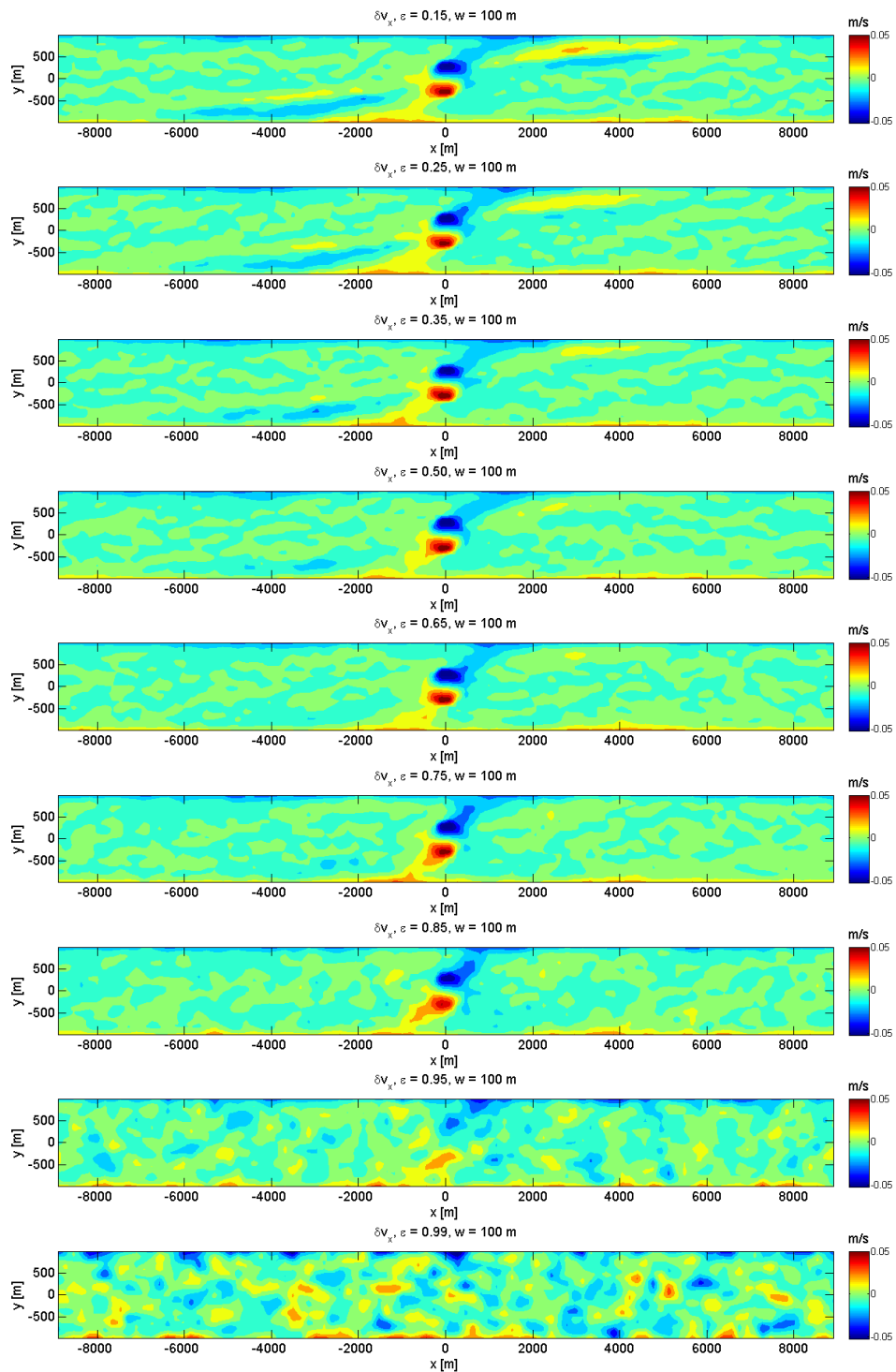


FIGURE B.4: Coarse grained fluctuating velocity in the x direction for 30,000 particles and different coefficients of restitution.

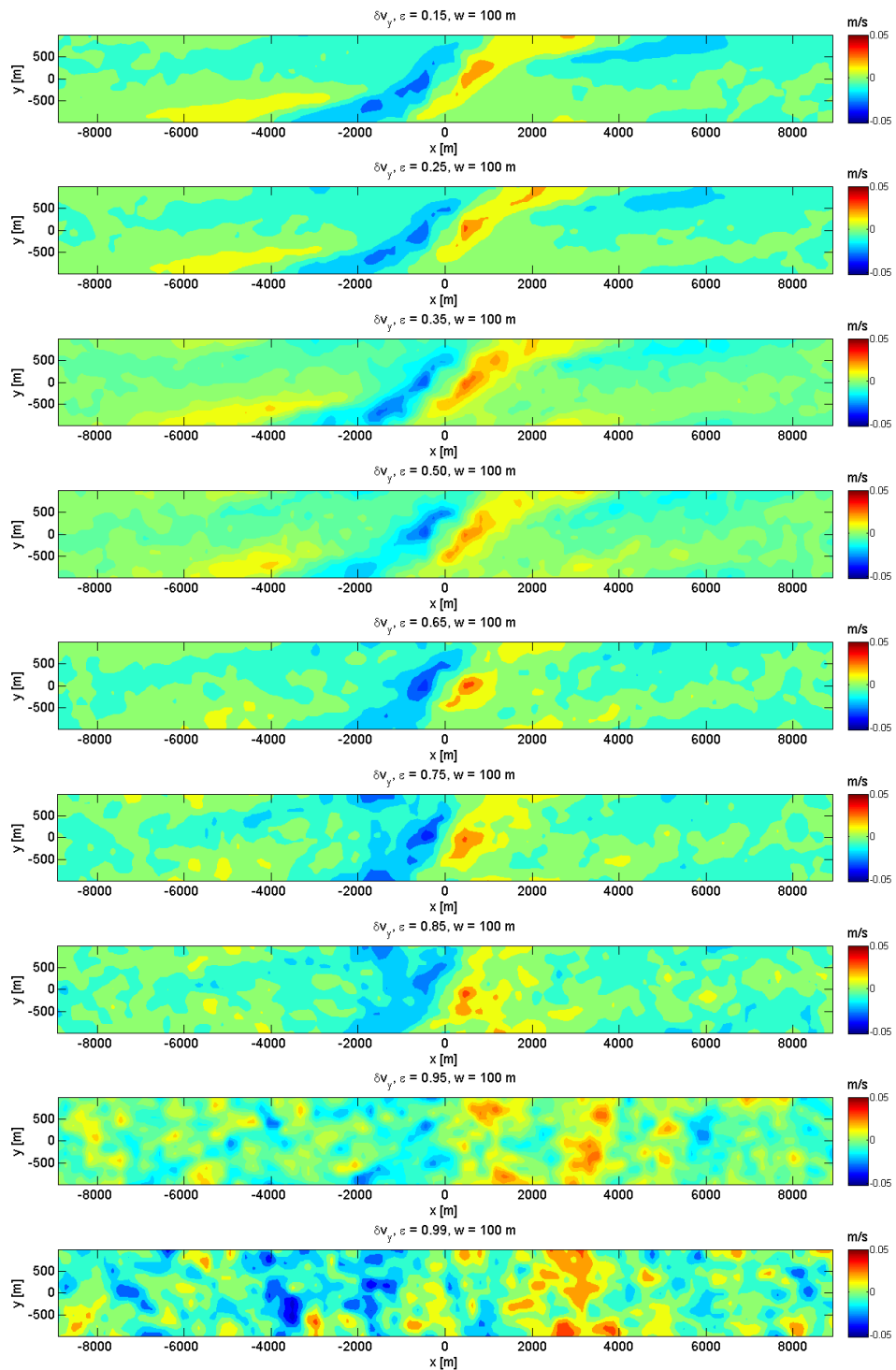


FIGURE B.5: Coarse grained fluctuating velocity in the y direction for 30,000 particles and different coefficients of restitution.

Appendix C

Supplemental Material for Clogging in a Constricted Suspension Flow

C.1 Drag Equation

In order to derive the Drag Equation (7.23) from dimensional analysis, first we start by choosing the parameters that we think could be involved in the solution variable, in this case, the drag force. By physical reasoning, we suspect that the drag force might be dependent on the velocity difference V , the density of the fluid ρ , its kinematic viscosity ν (we could have chosen the dynamic viscosity to give us the same result) and the cross sectional area A of the particle. We write the dimensions of these variables

$$\begin{aligned}
 [V] &= L^1 T^{-1}, \\
 [\rho] &= M^1 L^{-3}, \\
 [\nu] &= L^2 T^{-1}, \\
 [A] &= L^2, \\
 [F_D] &= M^1 L^1 T^{-2}.
 \end{aligned} \tag{C.1}$$

where M represents mass dimension, L the length and T time. We proceed to create the dimensional matrix:

	V	ρ	ν	A	F_D
M	0	1	0	0	1
L	1	-3	2	2	1
T	-1	0	-1	0	-2

TABLE C.1: Dimensional matrix of the parameters involved in the drag force.

The rank of the matrix is $r = 3$, the number of variables is $n = 5$, thus the number of dimensionless groups is $n - r = 5 - 3 = 2$. We call Π_1 the first dimensionless group and choose the solution variable to be the velocity, dependent on the density, viscosity and area. Next, we equate the dimensions of Π_1 with the dimensions of

the solution variable times the dimensions of the other parameters to an unknown power

$$\begin{aligned} [\Pi_1] = M^0 L^0 T^0 &= [V] [\rho]^a [v]^b [A]^c, \\ &= L^1 T^{-1} M^a L^{-3a} L^{2b} T^{-c} L^{2c}. \end{aligned} \quad (C.2)$$

Equating the powers of M , L and T we get three algebraic equations

$$\begin{aligned} 0 &= 1 - 3a + 2b + 2c, \\ 0 &= -1 - c, \\ 0 &= a, \end{aligned} \quad (C.3)$$

whose solution is

$$\begin{aligned} a &= 0, \\ b &= 1/2, \\ c &= -1. \end{aligned}$$

Knowing the powers of the variables we can write the first dimensionless group as

$$\Pi_1 = \frac{V\sqrt{A}}{v}, \quad (C.4)$$

we recognize (C.4) as the particle Reynolds number. For the second dimensionless group Π_2 , we take the drag force as the solution variable dependent on the density, the cross sectional area and the velocity difference. We equate their dimensions as done in (C.2)

$$[\Pi_2] = [F_D] [\rho]^a [A]^b [V]^c \quad (C.5)$$

to obtain the powers

$$\begin{aligned} a &= -1, \\ b &= -1, \\ c &= -2, \end{aligned}$$

so that we can write the second dimensionless group as

$$\Pi_2 = \frac{F_D}{\rho AV^2}. \quad (C.6)$$

If we define Π_2 as one half of the drag coefficient C_D we obtain the Drag Equation

$$\begin{aligned}
 F_D &= \Pi_2 \rho A V^2, \\
 &= \frac{1}{2} C_D \rho A V^2.
 \end{aligned}
 \tag{C.7}$$

In vectorial form it becomes

$$\mathbf{F}_D = \frac{1}{2} \rho C_D A |\mathbf{V}|^2 \hat{\mathbf{V}},
 \tag{C.8}$$

which is equation (7.23). Now, this gives rise to a new problem, since the drag coefficient is not constant and depends on the form of the particle and the Reynolds number of the flow it is submerged in. This problem has been known since many years and addressed in different ways. In particular, an old article by Flemmer & Banks [57] gives an expression for the drag coefficient of spherical particles in terms of Re_p when $Re_p < 0.3$

$$C_D = \frac{24}{Re_p},
 \tag{C.9}$$

which for $Re_p = 0.084$ gives $C_D \approx 285.7$. A newer article by Mikhailov & Freire [58] shows $C_D = 242.6$ for $Re_p = 0.1$.

C.2 Clogging Complementary Plots

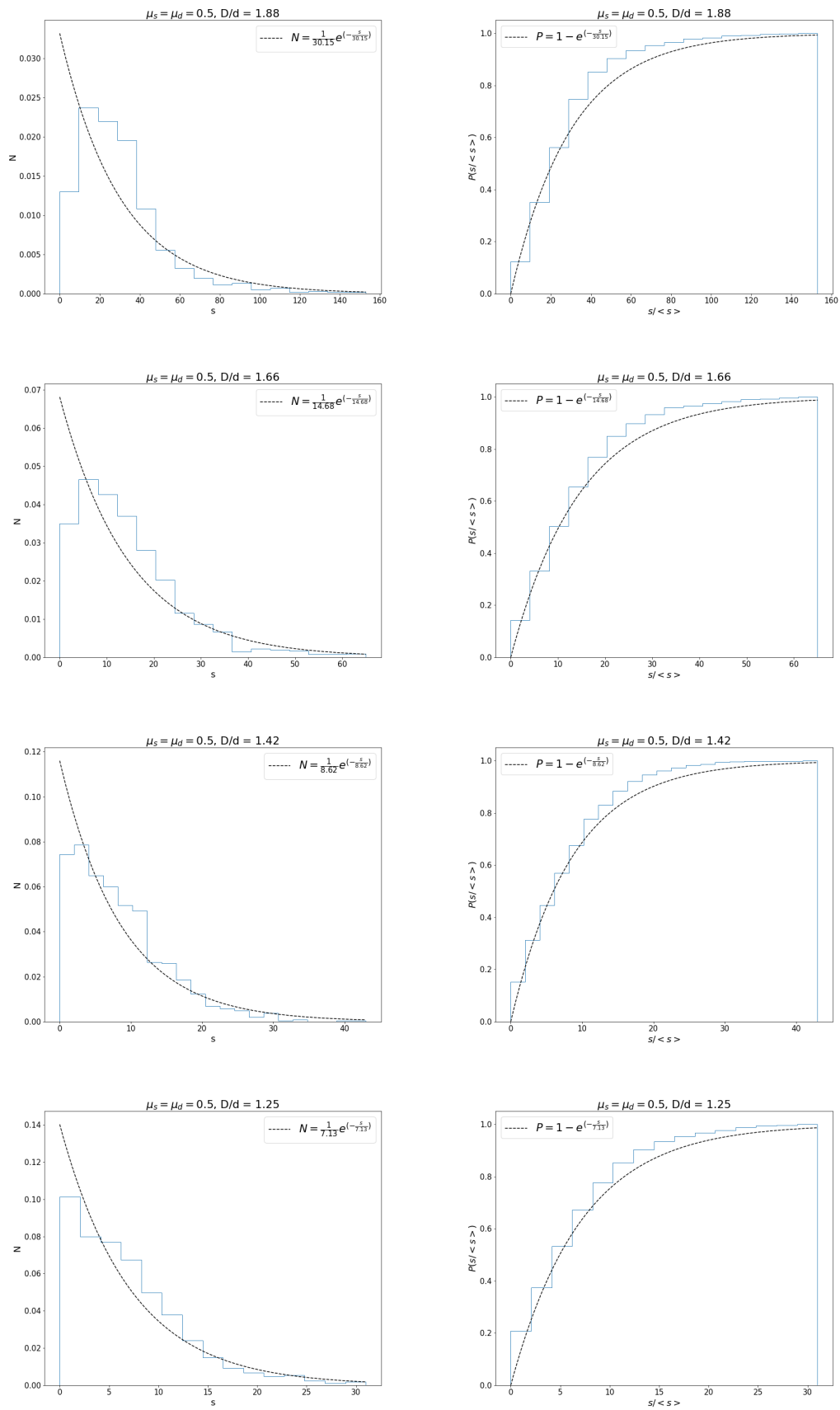


FIGURE C.1: PDF's (left side) with their corresponding CDF's (right side) for different values of D/d .